NORTHWESTERN UNIVERSITY

CREATION OF PEPTIDE AMPHIPHILE ARCHITECTURES AND ITS APPLICATIONS TO LIVING SYSTEMS

A DISSERTATION

SUBMITTED TO THE GRADUATE SCHOOL
IN PARTIAL FULFILLMENT OF THE REQUIREMENTS

for the degree

DOCTOR OF PHILOSOPHY

Field of Materials Science and Engineering

By

Shuming Zhang

EVANSTON, ILLINOIS

December 2008

ABSTRACT

Creation of Peptide Amphiphile Architectures and

Its Applications to Living Systems

Shuming Zhang

Peptide Amphiphile (PA) molecules developed in the author's laboratory and others have shown great versatility in creating self-assembled nanostructures with built-in biological and/or chemical functionalities. Their applications in spinal cord injury repair, angiogenesis, promoting cell adhesion and templating inorganic materials have also been well studied. Complementing previous compositional studies, where functions are mostly acquired via changes in compositions, this work has investigated strategies and methods to introduce architectural information into PA systems. Contributions of this work focused on understanding how temperature, pH, screening ions, aging, steric effects, and molecular design affect the formation of self-assembled nanostructures and downstream performance of macroscopic materials. A thermal energy pathway for self-assembly was discovered which drastically changes the final macroscopic nature of the material. In particular, it was observed that when a PA solution is heated to 80°C for 30 minutes aggregate of PA molecules formed a two-dimensional plaque structure at the elevated temperature. Upon cooling the plaque structure breaks into highly aligned fibrils to form a liquid crystalline substance as demonstrated by birefringence. By manually dragging this liquid

crystalline substance from a pipette onto salty media, it is possible to extend and fix the alignment over arbitrary lengths creating noodle-shaped viscoelastic strings. In great contrast, simple aging of PA solution at room temperature cannot lead to such drastic changes in short amount of time. It is hypothesized this emergent plaque structures are formed through aggregation of dehydrated fibers at elevated temperature. Besides temperature, pH value, screening ions and steric effects were also found to actively participate in this process. High repulsive interactions due to electrostatics and bulkiness of molecules inhibit the formation of liquid crystalline substance through heat treatment. By reducing potential interfiber ionic bridging through pH adjustment and molecular design, hydrogel fluidity can be increased and leads to improved robustness of final materials. Preferential cellular orientation and outgrowth of mammalian cells were achieved using such newly developed extracellular matrix (ECM) analogues in living systems. We envision these PA strings as substrates for “cellular wires” to direct biological function in space or as templates for alignment of one-dimensional nanostructures over macroscopic distances without the use of lithography.

Finally, this work also investigated strategies and methods to create and analyze combinatorial hydrogel arrays with encapsulated cells using a high throughput system. In these efforts, combinations of different PA molecules could be mixed at various ratios with cells into hydrogel arrays by automatic fluid handling robots. It is proved that with a small amount of cells, RNA can be quickly isolated and analyzed by one-step multiplex reverse-transcriptase polymerase chain reaction (RT-PCR). Using this system, culture conditions can be changed to

test multiple variables, such as PA concentration, growth factors, media type etc. While the system still needs optimization, it could potentially facilitate our efforts for discovering material candidates to be used in biomedical applications.

Thesis Advisor: Prof. Samuel I. Stupp

Acknowledgements

The completion of a graduate degree is a special and unique event. But as with all research, the accomplishments of one person reflect the contributions of many others. This thesis would not exist without the contributions of the many people listed here.

I want to thank my PhD advisor, Professor Samuel I. Stupp, who had encouraged me to do things that I never imagined I could be able to do in graduate school. The opportunities, experiences, freedom and concepts uniquely available from his group deeply shaped my research at Northwestern University. Thanks are also due to Professor Lonnie D Shea, Professor Phillip B. Messersmith and Professor Kenneth R Shull for their time and help as my committee members in the defense. Their insight and suggestions are greatly appreciated.

The research described in this thesis is the result of collaborations with a number of talented scientists. Without the experimental and intellectual contributions of some, this work would not have been possible; without the assistance of others, it would be far from complete. I am deeply grateful to Dr. Alvaro Mata, Megan Greenfield, Dr. Liam Palmer, Dr. Ramille Capito, Dr. Conrado Aparicio, Dr. Ronit Bitton for working together with me on the PA Noodle Project. I also want to thank Christina Newcomb, Saahir Khan, Dr. Arun Sharma, Lesley Chow, Eugene T. Pashuck, Takahiro Muraoka for working together on my other projects. Sincere appreciation also goes to Dr. Qingrun Zhang, Dr. Liangshi Li, Dr. Honggang Cui, Dr. Hongzhou Jiang, Dr. Yuri Velichko and many others. They have been great sources of inspiration in discussions all

these years. Special thanks for help in chemical synthesis and purifications to Dr. Andrew Cheetham.

Last, my family and friends have always provided the foundation for my personal and intellectual growth. Their love and support throughout the course of my research experience have helped me to maintain a sense of balance and perspective. This thesis is a reflection of their devotion, and a tribute to each of them.

List of Abbreviations

a.u.	arbitrary units
CCC	critical coagulation concentration
CD	circular dichroism
EDX	energy dispersive x-ray spectroscopy
ESI-MS	electrospray ionization mass spectrometry
GAPDH	glyceraldehyde-3-phosphate dehydrogenase
hMSC	human mesenchymal stem cell
HPLC	high-performance liquid chromatography
POM	polarized optical microscopy
PA	peptide amphiphile
PBA	pyrenebutyric acid
PBS	phosphate-buffered saline
QFDE	quick-freeze deep-etch
rhBMP	recombinant human bone morphogenetic protein
RT-PCR	reverse-transcriptase polymerase chain reaction
SAM	self-assembled monolayer
SAXS	small angle x-ray scattering
SEM	scanning electron microscopy
SMC	smooth muscle cell
TEM	transmission electron microscopy
UV	ultraviolet
WAXS	wide angle x-ray scattering
μCP	micro-contact printing

Table of Contents

List of Tables

List of Figures

CHAPTER ONE

Introduction

Chapter 1: Introduction

1.1 Background of Biomaterials

Materials are the basic substances that make up the world. They can be natural, like wood, or man-made, like plastic. So far, there are over 300,000 different known materials. Because of its close ties to the development of humanity, the study of materials science is one of the oldest forms of engineering and applied science. Although the field of materials science started mostly with ceramics and later metallurgy, it has since broadened to include every class of materials, such as ceramics, polymers, metals, semiconductors, magnetic materials, biomaterials, and many others.

Among these, the field of biomaterials has steadily grown over the years by integrating ideas from medicine, biology, chemistry, and engineering. In definition, biomaterials are "any substances (other than a drug) or combination of substances synthetic or natural in origin, which can be used for any period of time, as a whole or as a part of a system which treats, augments, or replaces any tissue, organ or function of the body" [1]. In the early stage of this discipline, researchers took materials from other existing technologies and applied them to human medicine with small modifications. Examples include the first intraocular lenses made from poly(methyl methacrylate) (PMMA), a material previously used for making cockpits of fighter planes [2, 3]; the first successful vascular grafts made from parachute fabric [3]; Since then, the continuous development of metal alloys and synthetic polymers have resulted in more revolutionary

advances [4-6]. Major landmarks include the introduction of cobalt and titanium based alloys [7, 8], the first successful hip joint replacement made from high-molecular-weight polyethylene [3, 4], the first commercially available hydrogel-based contact lenses (made from hydroxylethylmethacrylate) [3], and the introduction of bone cement made from PMMA [3]. The field has gradually moved forward to the use of tailored materials that elicit a specific biological response. However, the expanding scope does not end there. With increasing understanding of the fundamental mechanisms in biology, and the complementary ability to control the micro-, nano-, and molecular-scale structures of many materials, researchers are now able to build sophisticated biomimetic materials, to learn about biology, to obtain biological information, to control biological processes, and even to use biology to make abiotic materials, see Figure 1 [9].

Given the many opportunities for scientific advances available through biomaterials, we are most interested in creating biomimetic materials and use them to control biological process. For this goal, it is beneficial to learn from diverse natural materials, such as bone, tooth, mollusk shell, bark and human skin (See Figure 2) [10, 11]. It is clear that their superior performances are deeply correlated to their structures as well as compositions. Similar lessons can also be seen in living tissues. For example, neuron, muscles, blood vessel, bladder and intestine all need architecturally well-organized cells to be functional (see Figure 3). Research works in this thesis are therefore focused on creation of architectures and tuning of compositions in biomaterials.

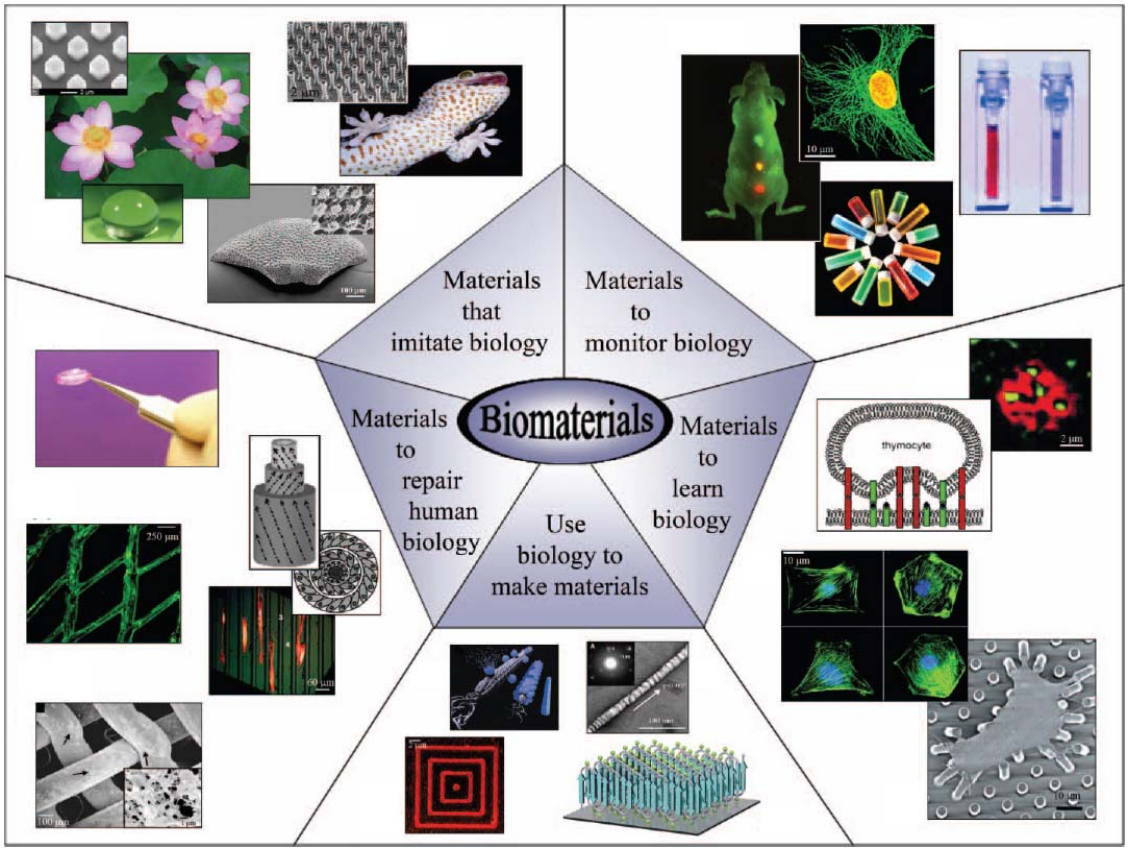

Figure 1 | Examples of modern biomaterials research (Reproduced from Stupp et al. [12])

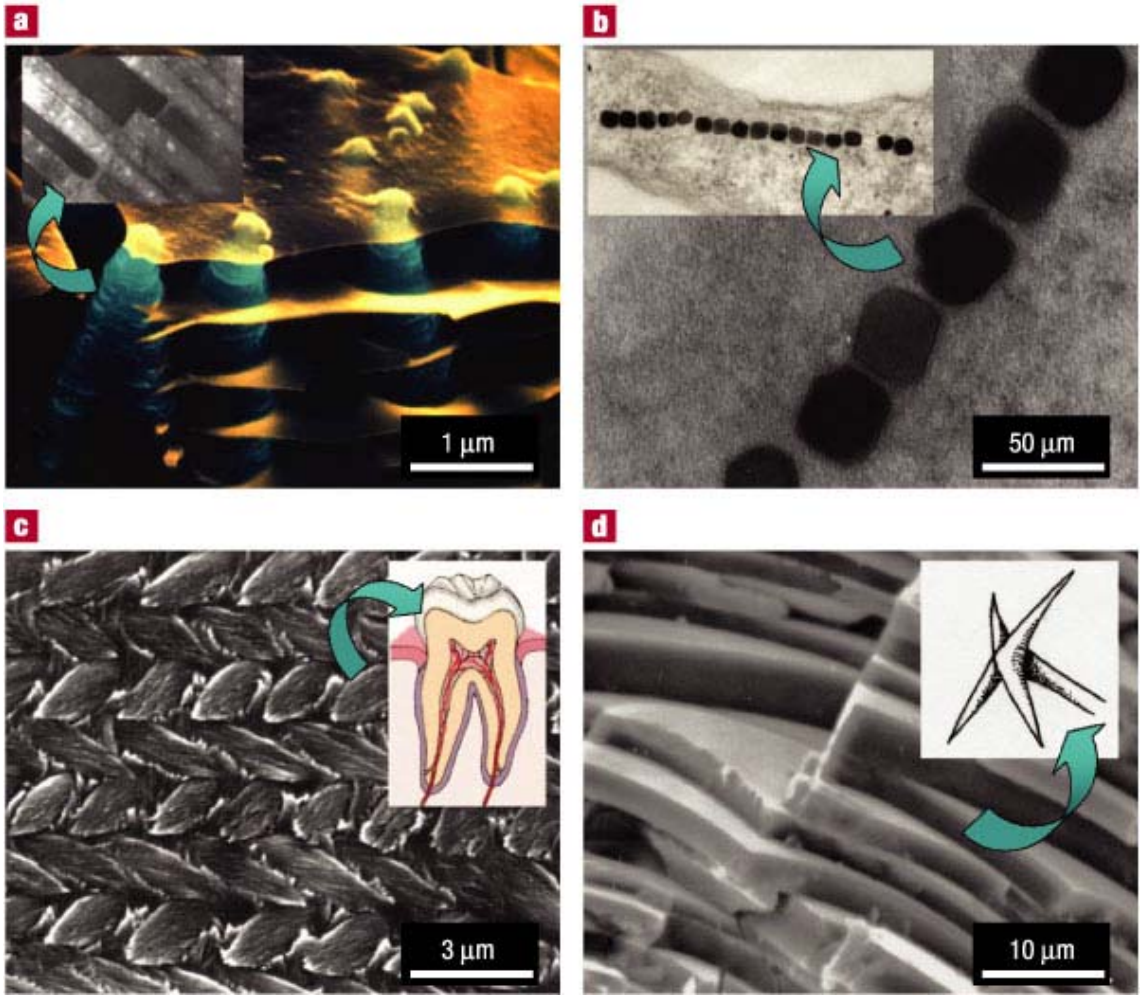

Figure 2 | Examples of biologically synthesized complex materials. **a**, SEM image of a growth edge of abalone. This is a layered, tough, and high-strength biocomposite. **b**, Magnetite nanoparticles formed by magnetotactic bacterium. **c**, SEM images of mouse enamel, a hard, wear-resistant material with highly ordered micro/nano architecture. **d**, SEM image of Rosella sponge, a biological optical fiber. (Image reproduced from [10])

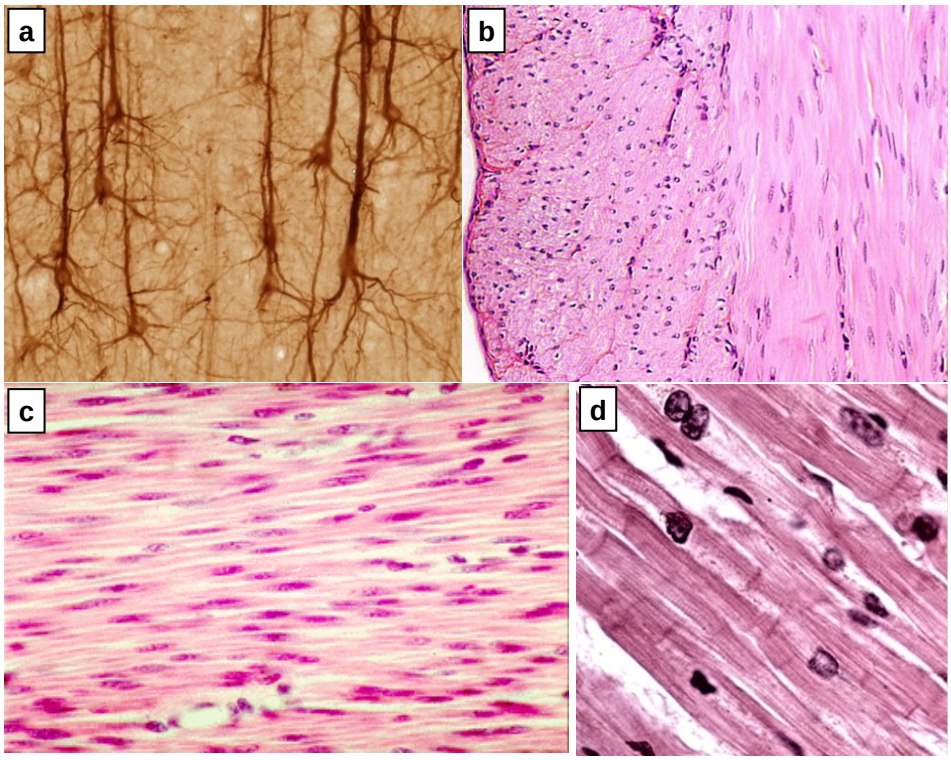

Figure 3 | Examples of living tissues with architectural organizations. **a,** In human brain, pyramidal neurons are aligned parallel to one another and perpendicular to the cortical surfaces [13, 14]. **b,** Smooth muscle of the intestinal wall; The outermost layer of smooth muscle is oriented longitudinally, while the inner layer of smooth muscle is oriented circularly. Coordinated contraction of the longitudinal and circular muscles squeezes material through the intestine in much the same way you squeeze toothpaste out of the tube. **c,** smooth muscle cells and **d,** cardiomyocytes in natural tissues are preferentially oriented so that cells can work synergistically (dilate and contract in the same directions).

1.2 Background of Self-Assembly

In our research, we used self-assembly as the primary tool to develop new structure and functions in biomaterials. Self-assembly is a term used to describe a process in which a disordered system of pre-existing components forms an organized structure or pattern as a consequence of specific, local interactions among the components themselves, without external direction [15-22]. Throughout biology, self-assembly is a powerful approach for fabricating novel supramolecular architectures across length scales. For example lipid molecules form oil drops in water, four hemoglobin polypeptides form a functional tetrameric hemoglobin protein, and ribosomal proteins coalesce with RNA into functional ribosomes. Scientists have applied this concept to develop a whole family of self-organized nanostructures such as zero-dimensional objects and spherical micelles [23-25], cylindrical micelles [26-28], ribbons [29-32], two-dimensional sheets [33-35], and three-dimensional networks [36, 37].

There are a few distinctive features that make self-assembly different from other processes. The first one is the key roles played by weak intermolecular interactions such as hydrogen bonding, $\pi - \pi$ stacking, solvophobicity, metal-ligand and van der Waals interactions [38-40] . Although these interactions are relatively small in isolation, when combined together as a whole, they govern the structural conformation of molecules and materials that arise from them, especially in biological systems. In many instances they determine the physical properties of liquids, the solubility of solids, and the organization of molecules in biological membranes. The second

feature is that the building blocks are not only atoms and molecules, but also nano- and micro-structures, with different chemical compositions, shapes and functionalities. As ligand-receptor, cell-substrate, and protein-protein interactions all occur on these scales, they are the right dimensions to study and control cellular behavior [41]. The third feature is, in order for self-assembly to take place, self-assembly process usually leads to a lower Gibbs free energy. However, because the relatively weak interactions in self-assembly are often subtle compared with covalent bonds, there is usually a delicate thermodynamic balance between various contributions in enthalpy and entropy to overcome the loss of translational and rotational entropy upon assembly [42, 43].

Most biologically relevant macromolecules, such as DNA, peptides and proteins interact through such weak interactions and self-assemble. Nature uses these forces and process to produce a long list of materials, such as collagen, keratin, pearl, shell, coral and others. Through observing and mimicking the processes by which supramolecular architectures are assembled in nature, biomaterials scientists can understand and produce entirely novel synthetic materials. The accurate and controlled application of self-assembly can lead to new and previously unachievable materials. Therefore self-assembly offers great opportunities for the creation of novel biomaterials.

1.3 Background of Peptide Amphiphile

In the field of biomaterials, scientists have been utilizing self-assembly to understand and

mimic biology for years [15, 44-46]. For example, Stupp laboratory at Northwestern [23, 26, 47-57] and others [58-69] have developed biomimic molecular systems capable of self-assembling into different nanostructures. Investigation of these systems has led to new structure and function of materials for a variety of uses, especially for biomedical applications [26, 30, 47-51, 70-80]. Among them, peptide amphiphiles (PA) have shown great versatilities in creating self-assembled nanostructures with built-in biological and/or chemical functionalities (see Figure 4) [81]. This family of molecules consists of a hydrophobic alkyl tail connected to a short peptide sequence. Upon addition of counterions or pH adjustment, these molecules can spontaneously self-assemble into networks of well-defined one dimensional nanofibers in aqueous environments. This process is thought to be triggered by peptide charge screening using counterions and facilitated by the collapse of the fatty acid as well as hydrogen bond formation among adjacent peptide segments [81-83]. Their applications in spinal cord injury repair [51], angiogenesis [49], promoting cell adhesion [84] and templating inorganic materials have also been well studied.

In the original design, PA molecule had five components: a long alkyl tail that conveys hydrophobic character to the molecule and makes the molecule amphiphilic; four consecutive cysteine residues that polymerize the self-assembled structure after oxidization; three glycine residues as a flexible linker; a single phosphorylated serine residue that help direct mineralization of hydroxyapatite; and the cell adhesion ligand RGD. Various modifications of the peptide sequence have since been made to simplify the design and expand the versatility. Typical

structures of current PA design are presented in Figure 5, highlighting four key structural features. Block 1 is still the long alkyl tail, block 2 is the beta-sheet forming segment, block 3 is the charged peptide segment and block 4 is the bioactive segment (epitope). These changes in PA design simplify different segments into standard functional building blocks for a more sophisticated molecule.

From the biological point of view, the most important feature of this material is the epitope, which imparts versatility by simple alteration of the sequence and presenting density. Many modifications have been made to endow varied biological properties [51, 77, 81]. Figure 6 is an example of gel that promotes neuron cell differentiation. As all of these molecules can form hydrogels that are structurally similar to extracellular matrices, they have been used in a variety of tissue engineering applications.

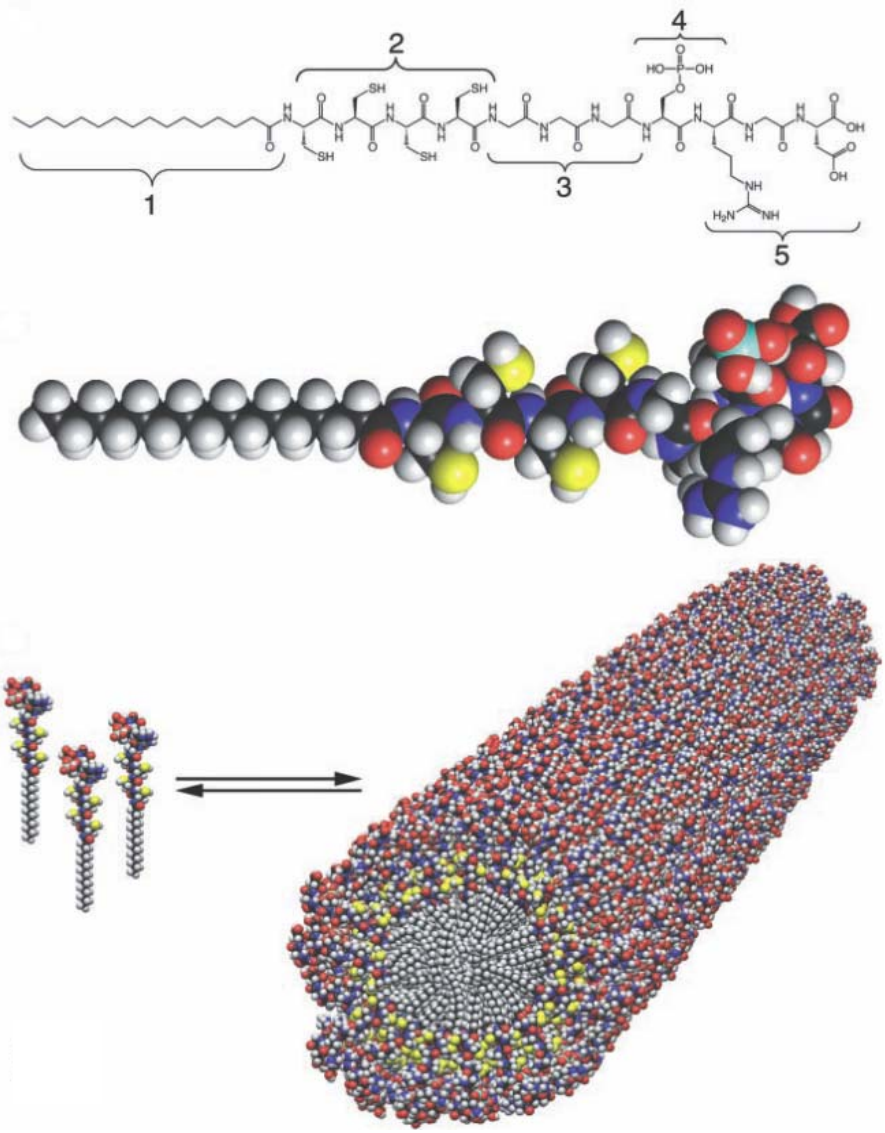

Figure 4 | Self-assembling peptide amphiphile molecule. A schematic of the molecule is shown, which further bundle together to form a cylindrical micelle (adapted from [81]).

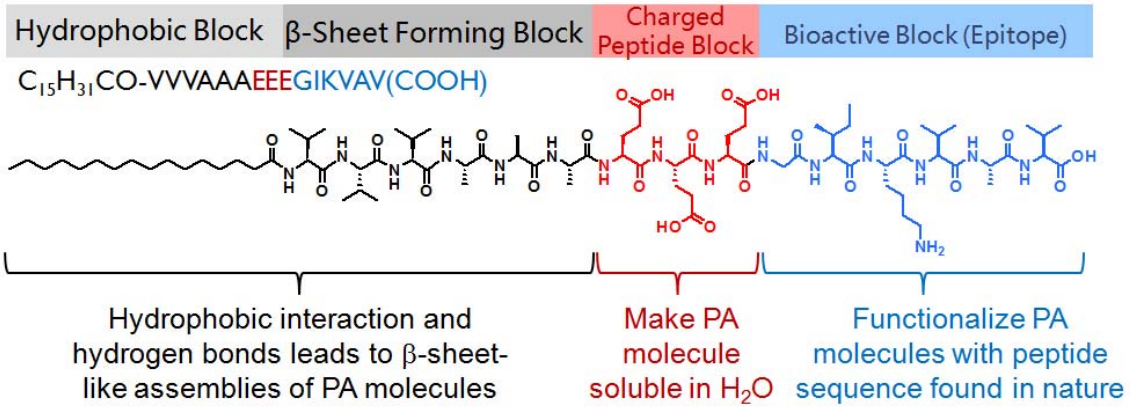

Figure 5 | Molecular structure of a PA molecule reflects current design principles. $C_{15}H_{31}CO$-VVVAAAEEEGIKVAV(COOH) was used as an example.

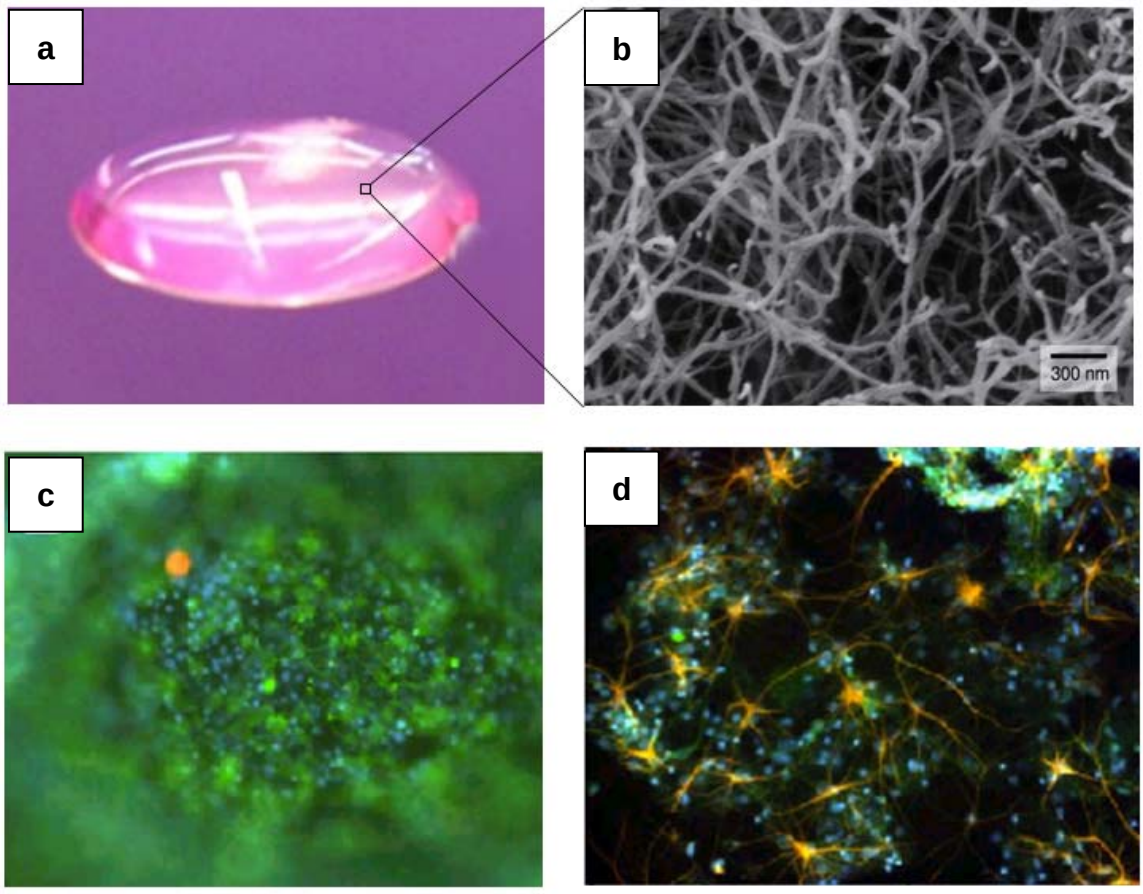

Figure 6 | Morphology of PA hydrogel ($C_{15}H_{31}CO$-AAAAGGGEIKVAV(COOH)) and its application in neuronal regeneration. **a,** PA hydrogel and **b,** its fibrous morphology under SEM. **c-d** Neural progenitor cells (NPCs) cultured under different experimental conditions; **c,** showed NPCs encapsulated in IKVAVPA gels started neuronal differentiation at 1 day. Differentiated neurons were labeled for tubulin (in green), and differentiated astrocytes (glial cells) were labeled for GFAP (in orange). **d,** NPCs cultured on laminin-coated cover slips at 7 days. The prevalence of astrocytes is apparent. (Figure was adapted from Silva, G.A., et al.[51])

1.4 Strategy and Approach

In Chapter 2 to Chapter 4, we investigated the strategies and methods to introduce architectural information into PA systems. Using knowledge in molecular self-assembly, we first studied how a thermal energy pathway can change behavior of PA molecules and facilitate their assembly into novel nanostructures. More specifically, we subjected a PA solution to elevated temperature and then cool down to room temperature. Various microscopic and spectroscopic characterization techniques, such as SEM, TEM, QFDE, CD, POM, EDX, SAXS, were used to probe the self-assembly behavior of PA molecules in this process. Other factor such as pH, ion screening, aging, and steric effects were also studied. The novel nanostructures prepared by this pathway were then fabricated into hydrogel strings, which were characterized by the extraordinary long range alignment of PA nanofibers. To study their applications in living systems, mammalian cells were encapsulated into such strings and cultured. Their responses to such new hydrogel were then analyzed in morphology and gene expressions.

In Chapter 5, we present our efforts to study the biological response of mammalian cells to PA gels. In this study, PA molecules of different designs were synthesized and mixed at various ratios with cells to form a hydrogel. After culturing, cells' responses to these hydrogel were analyzed with a real time RT-PCR based high-throughput screening method.

CHAPTER TWO

A Self-Assembly Pathway to Create Macroscopic Strings of Aligned Nanofibers

Chapter 2: A Self-Assembly Pathway to Create Macroscopic Strings of Aligned Nanofibers

2.1 Introduction

Inspired largely by biological systems, molecular self-assembly continues to be a theme of great interest in science. The targets differ broadly, from accessing ordered materials and self-assembling devices [85-87] to understanding how misfolded proteins self-assemble into stable fibers linked to human disease [88, 89]. Knowledge of self-assembly is concentrated on molecular principles for the design of crystals [90], liquid crystals [91], organometallic complexes [92], supramolecular aggregates [93-95], and pattern formation by phase-separated block copolymers [96-98], among others. Far less is known about self-assembly mechanisms and dynamics or about energy pathways to emergent macroscopic objects. In this work, aggregates of charged amphiphilic molecules containing peptides have been found to access a structure at elevated temperature that templates alignment of nanofiber bundles over macroscopic scales. The thermal pathway leads to a lamellar plaque structure that breaks upon cooling into a fluid of aligned fibrils. By manually dragging this liquid crystal from a pipette onto salty media, it is possible to extend and fix the alignment over centimeters in noodle-shaped viscoelastic strings. In great contrast, if the same aggregates of molecules do not access the plaque structure, they only form isotropic networks of fibrils upon addition of salt. We hypothesize this remarkable fibril alignment is templated by emergent 2D structures that fluctuate between states with and

without 1D texture. Mesenchymal stem cells were found to survive and align inside these noodle-shaped constructs and exhibit differentiation trends that are sensitive to the unusual long-range orientation of these systems. We envision the strings as substrates for "cellular wires" to direct biological function in space or as templates for alignment of 1D nanostructures over macroscopic distances without the use of lithography.

2.2 Materials Behavior Changes at Elevated Temperature

We report here on the evolution of molecular aggregates into macroscopic arrays of aligned nanofibers that can have arbitrary length. We prepared 0.5–1.0 wt % aqueous solutions of a peptide amphiphile (PA) known to self-assemble into high-aspect-ratio nanofibers [81, 99]. The PA molecules contain the peptide sequence $V_3A_3E_3$ and a C_{16} alkyl tail at the peptide's *N*-terminus (Appendix 1), and their self-assembly into nanofibers is triggered by ions that screen the charged amino acid residues. We heated the aqueous solutions to 80°C and kept them at this temperature for 30 minutes before cooling to 25°C. After this heat treatment, the solutions became viscous and strongly birefringent as observed between cross polars in an optical microscope. This result suggests the formation of a liquid crystalline substance with orientational order. When calcium chloride was added to the heated and cooled PA solution, we observed the formation of a gel that was at least four-fold stiffer than one formed from an unheated solution (see supporting evidences). Using polarized optical microscopy, we found that gels or films formed from heated solutions contained large birefringent domains (tenths of millimeters) (Figure 7), while those

formed from unheated solutions did not generate birefringent gels and appeared isotropic. We observed that noodle-like strings of arbitrary length or diameter could be formed by simply manually dispensing the aqueous PA solution in a salty medium (Figure 7 a-b). When the solution was dragged on a surface covered by a thin layer of this medium (Figure 7 c), uniform birefringence was observed along the length of the noodle (Figure 7 h-i). This observation suggested that macroscopic alignment extending over centimeters was achieved. Using the same methods, the unheated solutions did not form stable strings or show any birefringence. Scanning electron microscopy (SEM) indicated that gels formed from heated PA solutions contained extraordinarily long arrays of aligned nanofibers (Figure 8 a-d). In great contrast, unheated PA solutions formed matrices of randomly entangled nanofibers (Figure 8 e-f). Small angle x-ray scattering (SAXS) experiment of these aligned and random matrix gave distinctly different scattering patterns (Figure 9), indicating the difference seen in SEM is throughout the materials. Similar behavior was observed with other PA molecules, although the structural integrity of the string depended on the amino acid sequence (see supporting evidences).

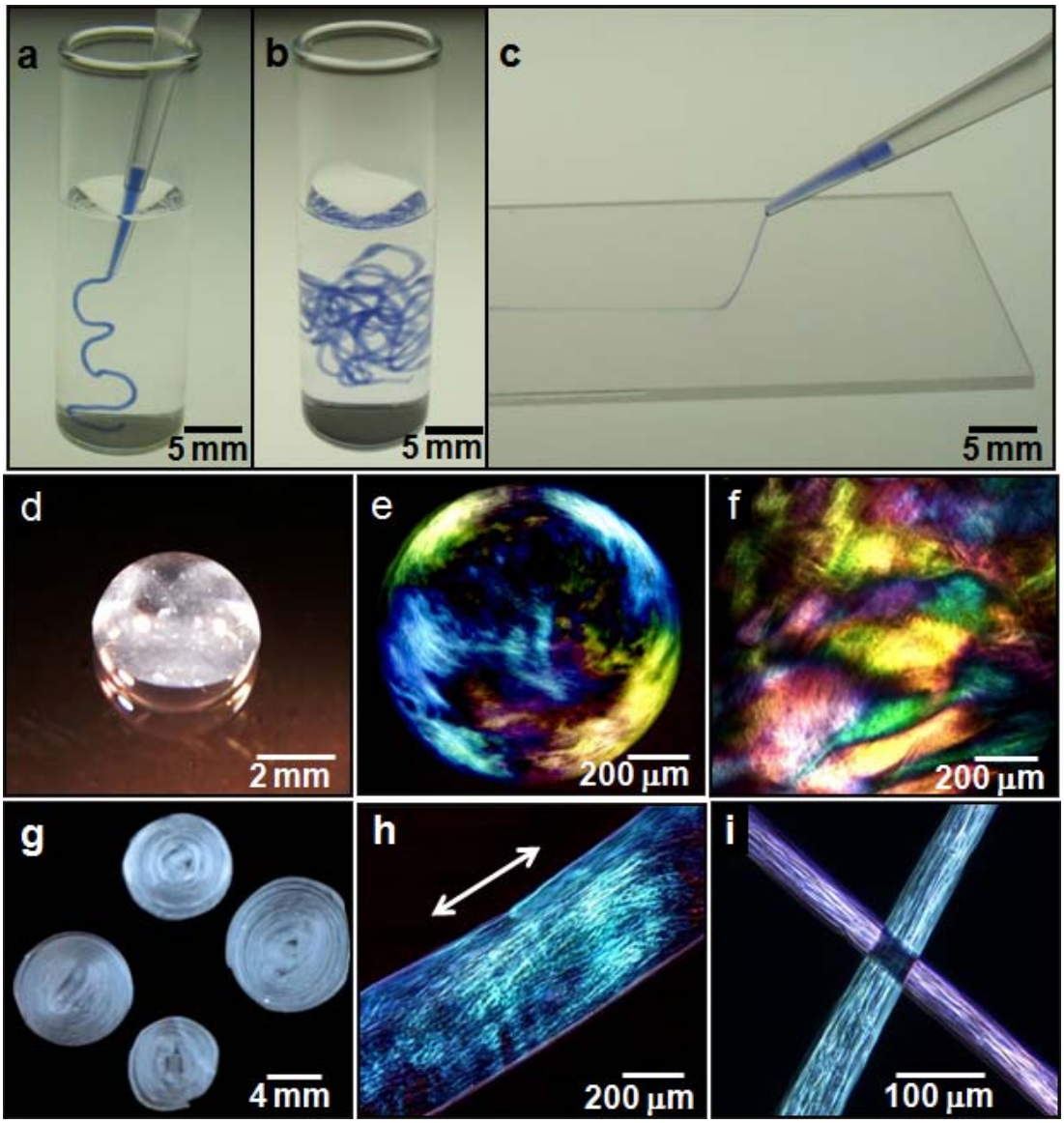

Figure 7 | Strings and gels with long-range internal alignment. **a**, **b**, PA solution colored with trypan blue injected into phosphate buffered saline after heat treatment. **c**, The same solution dragged through a thin layer of aqueous $CaCl_2$ to form a noodle. **d**, A bubble gel prepared with the heat-treated PA solution and $CaCl_2$. **e**, Birefringence of bubble gel as in (**d**) observed between cross polars suggesting the presence of macroscopically aligned domains. **f**, Similar domains in a gel film. **g**, PA noodle spirals prepared on a spin coater. **h**, Birefringence of a single noodle suggesting alignment along the noodle axis. **i**, Light extinction between cross polars at the crosspoint of two noodles demonstrating uniform alignment in each.

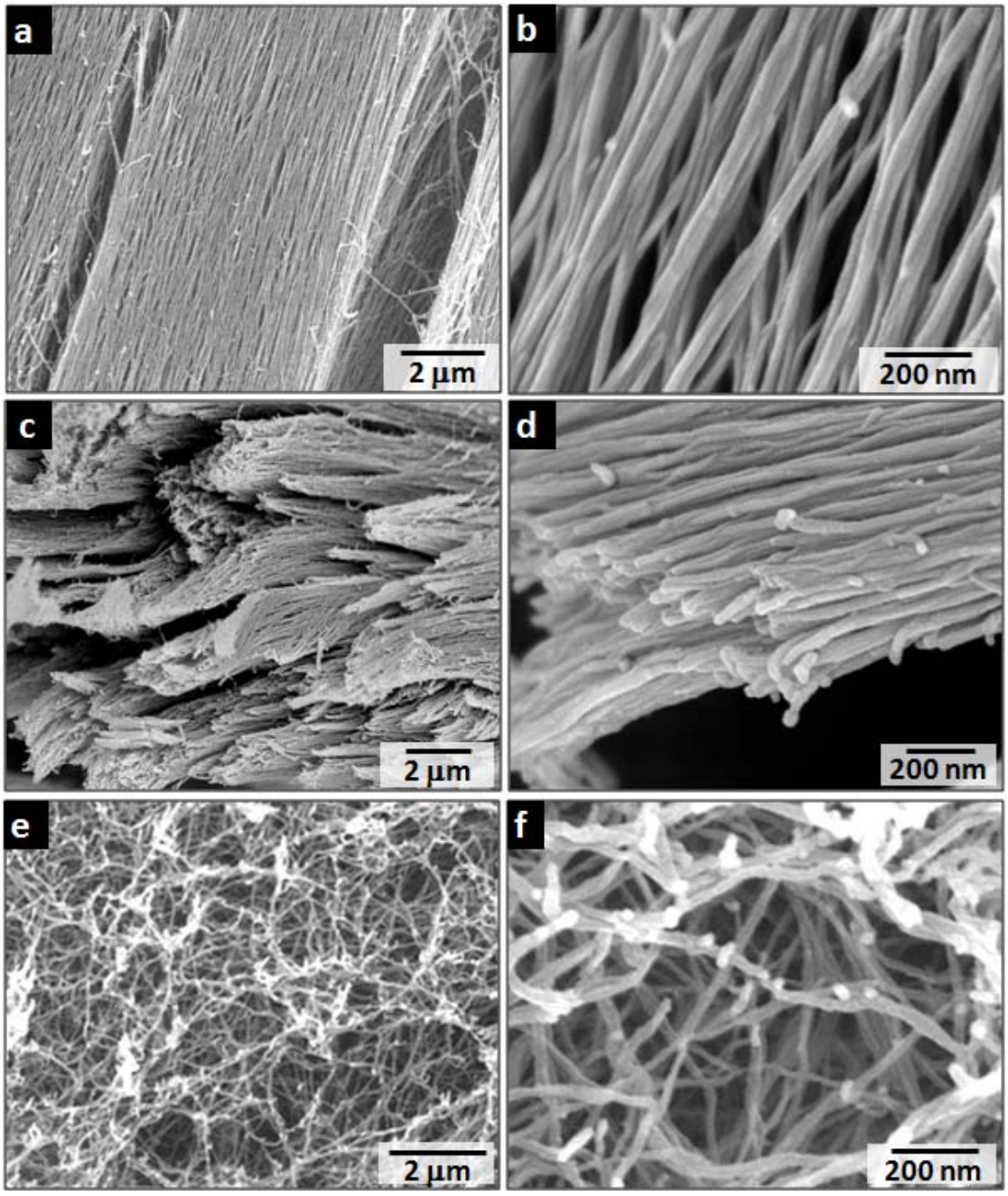

Figure 8 | SEM evidence of massive alignment versus isotropy of fibrils. **a**, **b**, Aligned nanofiber bundles in macroscopic strings formed by dragging thermally treated amphiphile solutions onto a $CaCl_2$ solution. **c**, **d**, Spontaneous long-range alignment of nanofiber bundles after adding $CaCl_2$ at 80°C. **e**, **f**, Isotropic network of nanofiber bundles formed by adding $CaCl_2$ to unheated amphiphile solutions. (Images courtesy of Dr. Alvaro Mata)

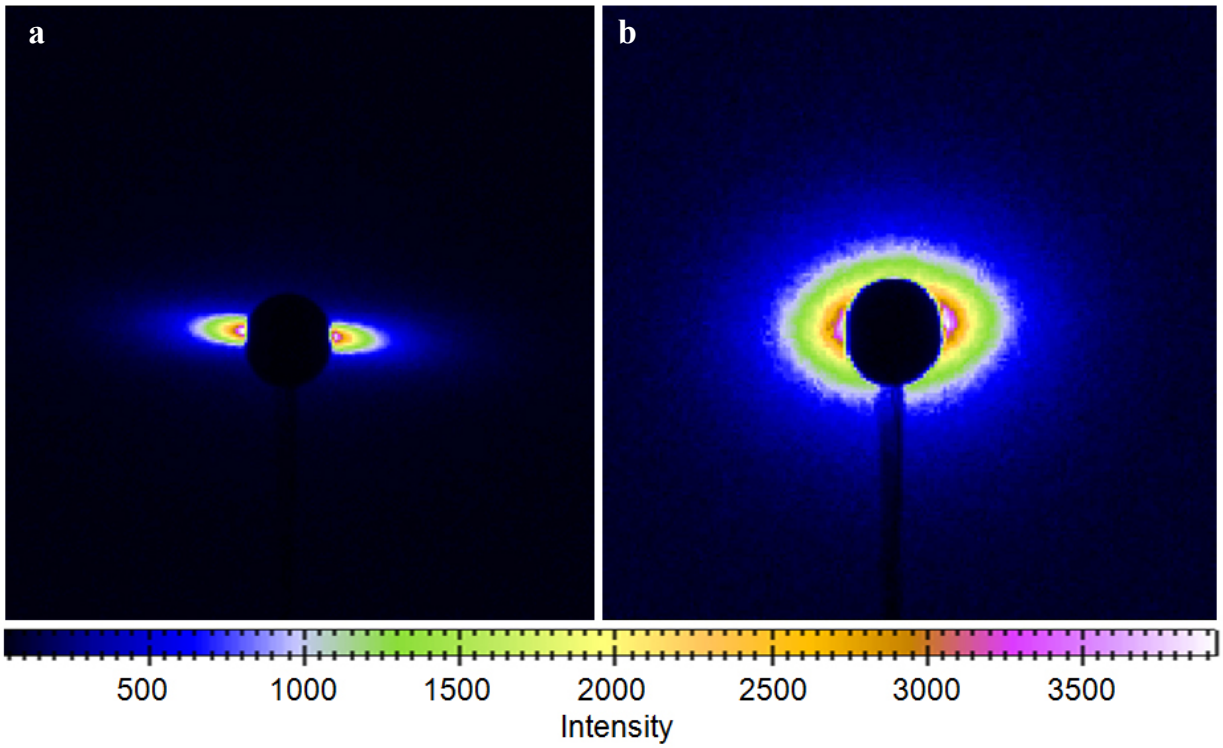

Figure 9 | Small angle x-ray scattering (SAXS) of PA noodle formed from a 2 wt% solution with and without heat treatment. The ratio of long axis to the short axis of iso-intensity lines derived from the SAXS patterns can be used to quantify the anisotropy of scattering objects. Larger value corresponds to higher anisotropy. **a,** with heat treatment, nanofibers in PA noodle have high degree of orientation order. Scattering pattern is narrowly distributed in a small angle. **b,** without heat treatment, the same gelation condition lead to minimum orientation order in gel and a wider distribution of scattering intensity. (Images courtesy of Dr. Ronit Bitton)

2.3 Understanding the Heating Process

2.3.1 Morphological Study

In order to gain a mechanistic understanding of the observed transformations, we examined the effects of heating on the PA solution structure by quick-freeze/deep-etch (QFDE) transmission electron microscopy (TEM) [100]. QFDE is a sample preparation technique that allows high-resolution imaging of hydrated structures by electron microscopy while minimizing disruption of the sample due to fixation or processing (see supporting evidences). The freshly dissolved PA solution contained a variety of small aggregates, such as micelles, tubes, and vesicles (see supporting evidences). These aggregates were generally less than 100 nm in diameter and less than a micron in length. As expected, aggregates and free monomer within these solutions assemble rapidly into nanofibers upon addition of screening salts, thus forming an isotropic gel. After the PA solution was equilibrated at 80°C for 30 minutes, most of the small aggregates disappeared and we observed “plaque-like” structures up to microns in length and width (Figure 10 a). Some of these plaques had a periodic surface texture with a characteristic spacing of about 7.5 nm, which corresponds to the expected diameter of a single canonical nanofibers [81, 101] (Figure 10 b). The plaque contained both smooth and textured regions, indicating that this structure was not simply an aggregate of fibers. The PA solutions that had been heated and then cooled to room temperature were clearly composed of aligned nanofiber bundles (Figure 10 c).

The bundles did not have the canonical nanofiber dimensions, but were instead tens of nanometers in diameter and several microns in length.

In order to image the plaque by SEM, we fixed the structure by adding calcium chloride at 80°C. Although most of the sample cooled to ambient temperature was composed of large arrays of aligned nanofibers, the plaque structure was captured as well (Figure 10 d). These plaques measured about 40 nm in thickness and had lengths and widths comparable to those observed by QFDE-TEM. They often contained long parallel striations and, in some cases, appeared to crack into fiber bundles (Figure 10 e). Using energy dispersive X-ray spectroscopy (EDX), we confirmed that the atomic composition of the plaque is the same as that of the observed fibers (see supporting evidences). Plaque structures were not observed in the unheated PA solutions or gels.

2.3.2 Spectroscopical Study

Both of these morphological studies indicated a morphological transition at elevated temperature. To confirm this transition by spectroscopical methods, we did small angle x-ray studies over heated vs. unheated PA solutions. In Figure 11, freshly dissolved PA solution (1 wt%), was scattered at 25°C, two minutes after being heated at 80°C and after cooling back to 25°C. Result shows that a peak near q=0.08 $Å^{-1}$ disappeared after solution is heated to 80°C.

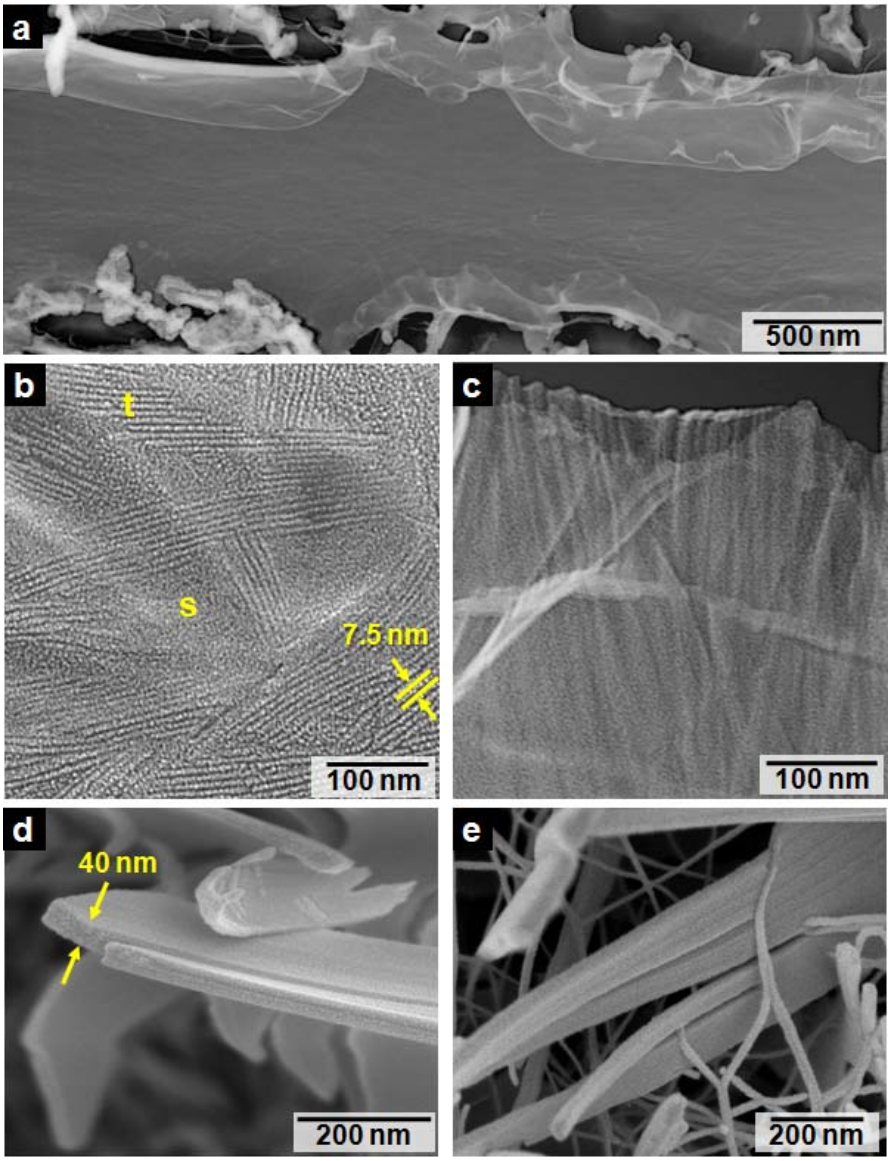

Figure 10 | Micrographs of structures captured at 80°C. **a**, TEM obtained after a quick-freeze/deep-etch (QFDE) preparation of PA solution at 80°C revealing a micron-sized, sheet-like structure curling at the edges. **b**, Higher resolution QFDE-TEM of the sheet-like structures revealing smooth (s) and textured (t) regions with a periodicity of about 7.5nm. **c**, QFDE-TEM of aligned nanofiber bundles templated by the sheet-like plaque after the PA solution was cooled to room temperature. **d**, SEM of plaques that were captured by adding $CaCl_2$ at 80°C. **e**, SEM of nanofiber bundles originating from a plaque. (Images courtesy of Megan Greenfield and Dr. Alvaro Mata)

After cooling back to room temperature, this change is preserved. As an unheated time control, a freshly dissolved solution was scattered after two hours of aging. The peak near q=0.08 $Å^{-1}$ is still there. Clearly, a transition happened during this heating process, which confirmed what we saw in QFDE and SEM. To find out the temperature needed for such transitions, 1 wt% PA solution was scattered at several different temperatures (Figure 12) after two minutes equilibration. Result showed that such transition only happened when PA solution was heated to 80°C. Lower temperature could not lead to this change that fast. Given the fact that PA solution viscosities more than doubled after 30 minutes heating at 50°C (Figure 30), the transition observed at 80°C may happen at lower temperature if heated longer. To further investigate the nature of this transition, we used larger q range and higher concentration (2 wt%) for SAXS. At 25°C, three peaks can be identified, which correspond to 3 nm, 5 nm and 7.5 nm. After being heated to 80°C, first two peaks did not change much. However, the 7.5 nm peak became less apparent and the peak maximum shift to lower q region. This result tells us that something is getting bigger in this process.

2.3.3 Proposed Mechanism

Another piece of useful information to decipher this process is that the gel formed with heat treated PA solution seems to have a larger average bundle diameter than that formed with unheated PA solution (Figure 14). Based on these observations, the mechanism about the transition is proposed as shown in Figure 15. A “fusing process” at elevated temperature causes the formation of large 2D structures through those small aggregates observed at room temperature. Upon cooling

or addition of divalent ions, this 2D structures break and template the formation of locally aligned nanofibers bundles. The driving force for fusing can be explained with Figure 16. This figure is an illustration of DLVO theory [102]. This theory suggests that the stability of a colloidal system is determined by the sum of van der Waals attractive (U_A) and electrical double layer repulsive (U_R) forces that exist between particles as they approach each other due to the Brownian motion they are undergoing. This theory also proposes that an energy barrier resulting from the repulsive force prevents two particles approaching one another and adhering together. But if the particles collide with sufficient energy to overcome that barrier, the attractive force will pull them into contact where they adhere strongly and irreversibly together. In our experiment, when the temperature is elevated to 80°C, molecules or aggregate collide with increased energy, which helps the coagulation process. Also, elevated temperature dehydrates molecules and aggregate, which favours the increase of entropy and facilitates coagulation process.

2.3.4 Mechanism Details

DLVO theory suggests the energy barrier can be reduced by addition of electrolyte. In Figure 17, we dissolved 1 wt% PA in water and PBS. These two solutions were then gelled with $CaCl_2$. Average diameter of fiber bundles in these two samples were estimated by SEM. Result showed an average diameter of 40.3 ± 8.2 nm and 26.7 ± 4.6 nm for sample with and without electrolytes. From this standpoint, both heating and electrolyte play similar roles. However, addition of monovalent electrolyte (at 1X PBS concentration) does not lead to noodle formation.

This might be due to the weak coagulation capacity of monovalent ions. An empirical observation known as the Schulze–Hardy rule states that the critical coagulation concentration (CCC) scales with the inverse sixth power of the counterion valence, i.e., $CCC \propto 1/z^6$ [103]. In reality, the coagulation capabilities of ions with the same valance are slightly different depending on their hydrodynamic diameter. Smaller hydrodynamic diameter leads to stronger coagulation capability.

For positive ions: $Ca^{2+} > H^+ > Cs^+ > Rb^+ > NH_4^+ > K^+ > Na^+ > Li^+$

For negative ions: $F^- > IO_3^- > BrO_3^- > Cl^- > Br^- > NO_3^- > I^- > CNS^-$

When we use divalent ions to gel PA solution, we never saw fiber bundles of canonical fiber diameter. The addition of $CaCl_2$ ions fused them together. However, as there is no pre-existing large aggregate, the formed fiber bundles are of smaller diameter.

As to the question why the structures we see at 80°C is two-dimensional, my hypothesis is, the built up electrostatic charge makes it easier to attach from side not top or bottom. And the built up charge also set a limit on the thickness of the plaque. Upon cooling or addition of Ca^{2+}, this two dimensional structures becomes more brittle and break into fiber bundles due to internal stress or bending of such two dimensional structures. As a result, fiber bundles emerge out from the two dimensional plaque structures.

With above explanation, this whole transition does not require a fix temperature to happen. The plaque structure accessed by these systems at elevated temperature clearly templates the remarkable long-range alignment of nanofibers observed. The alignment extends to macroscopic

dimensions and becomes fixed in the noodle structure by simply dragging solutions on salty media. Heating to 80°C provides enough energy to the system to reorganize from a collection of polymorphic aggregates into sheets capable of templating large arrays of aligned nanofibers upon cooling. We believe the dehydrated fiber state is thermodynamically stable at room temperature in these systems, an idea supported by the gradual formation of nanofibers by simple aging without heating. However, the macroscopic arrays of aligned nanofibers cannot be formed in solutions without first accessing the plaque structure at elevated temperature. The plaque state is therefore a necessary step of the energy pathway leading to the macroscopically aligned noodle. Of course, further theoretical calculation is still needed to support the proposed mechanism.

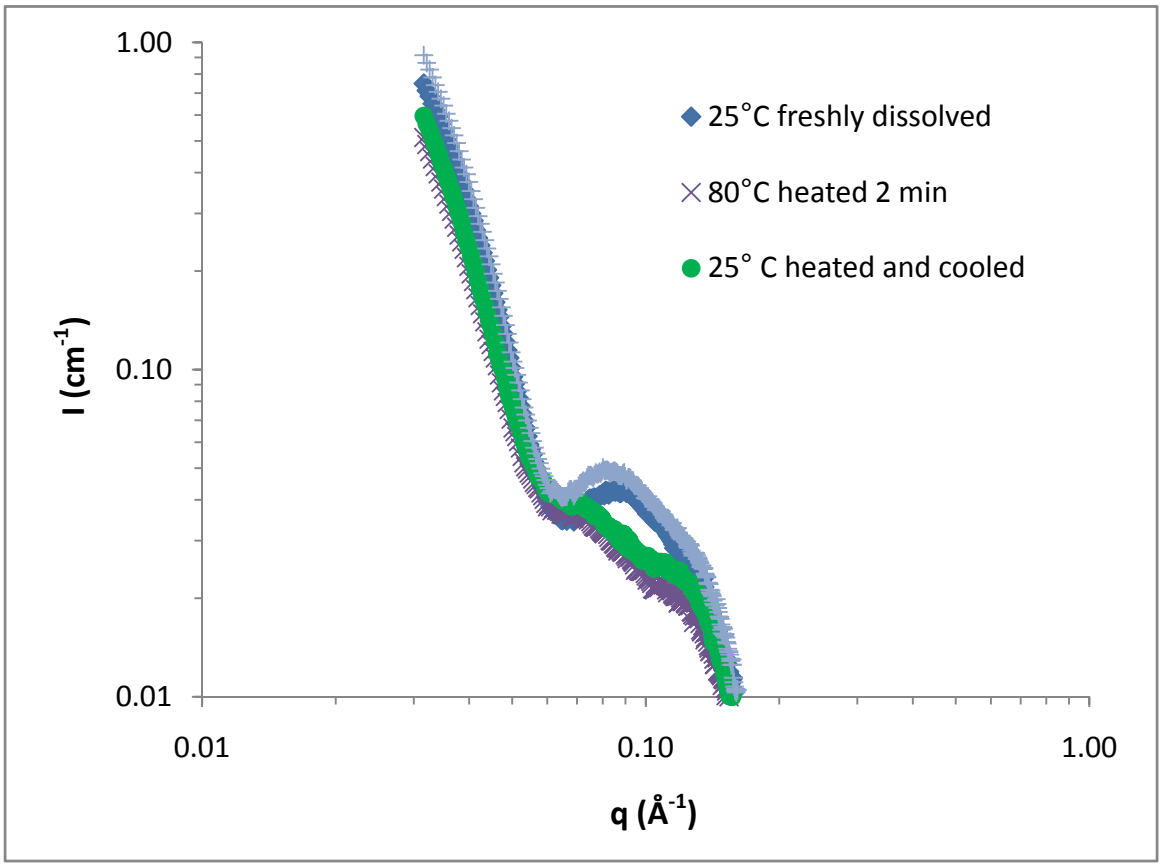

Figure 11 | SAXS result of 1 wt% PA solution ($C_{15}H_{31}CO$-VVVAAAEEE(COOH)) at 25°C and 80°C reveals transition between two temperatures. Samples tested include (**a**) freshly dissolved 25°C sample; (**b**) after being maintained at 80°C for 2 mins; (**c**) after being heated at 80°C for an hour and cooled back to 25°C; (**d**) an unheated control after fresh solution aged at 25°C for two hours. Result clearly showed a peak (q ~ 0.08 $Å^{-1}$) in **a,** which disappeared in **b** after heat treatment at 80°C. This change was preserved after cooling back to 25°C as shown in **c**. Two hours aging alone could not lead to the same change in sample **d**. (Figure courtesy of Dr. Ronit Bitton)

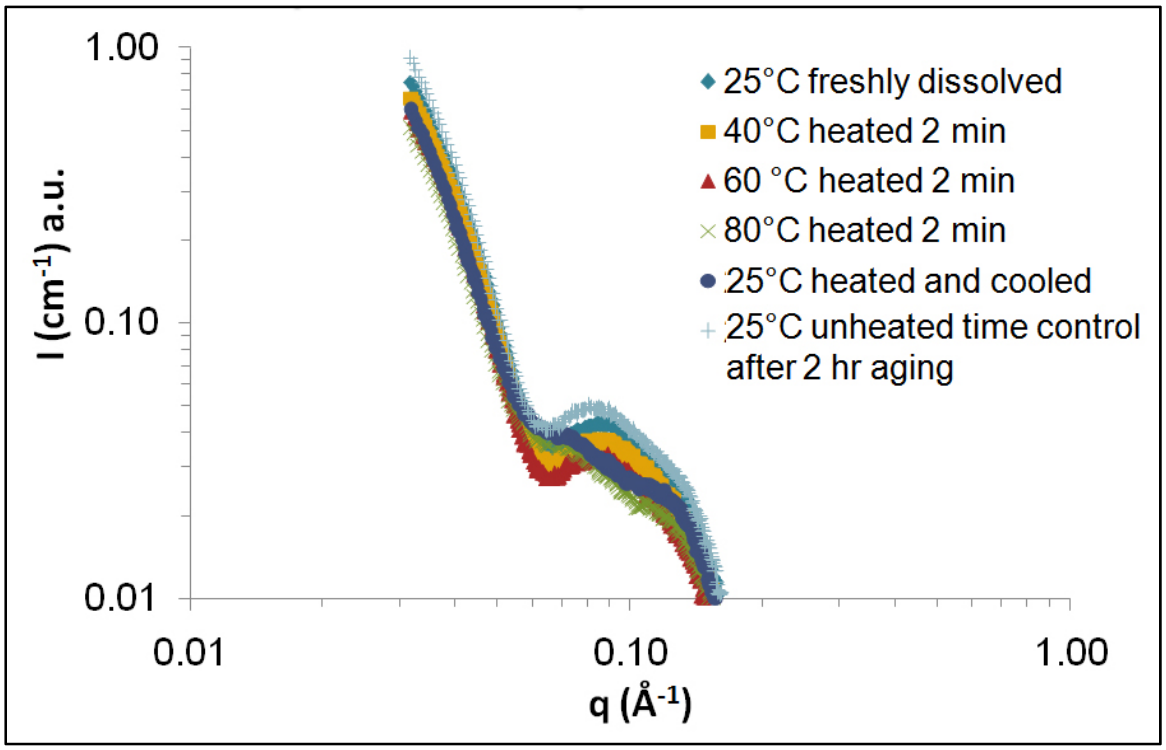

Figure 12 | SAXS result of 1 wt% PA solution ($C_{15}H_{31}CO$- VVVAAAEEE(COOH)) treated at 25°C, 40°C, 60°C and 80°C. Result showed only 80°C treatment can cause the transition seen in Figure 11 quickly. (Figure courtesy of Dr. Ronit Bitton)

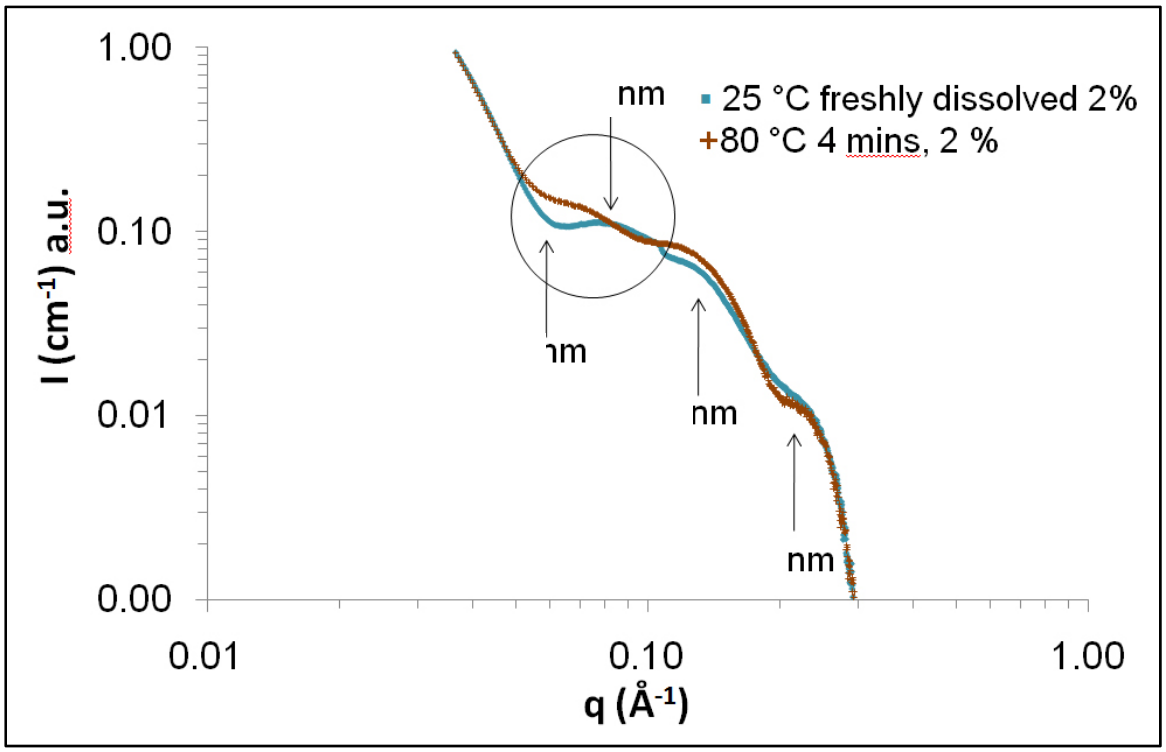

Figure 13 | SAXS result of 2 wt% PA solution ($C_{15}H_{31}CO$-VVVAAAEEE(COOH)) freshly dissolved at 25°C and after be heated at 80°C for four minutes. The result showed freshly dissolved 25°C solution has three peaks in SAXS, which correspond to d around 2-3nm, 4-5nm and ~7.5 nm. After heat treatment, the two peaks in high q region did not change much. However, in low q region, the position of the scattering maximum appears to shift towards smaller q region and the peak maximum becomes less apparent. (Figure courtesy of Dr. Ronit Bitton)

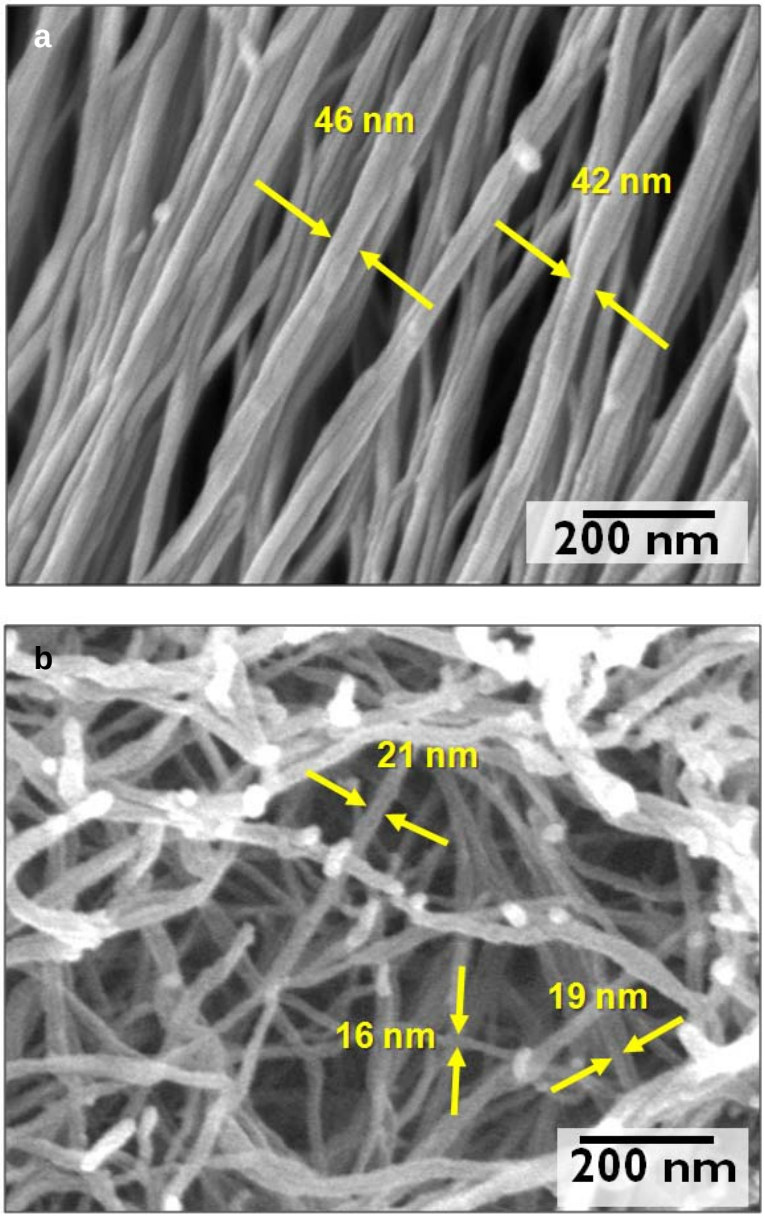

Figure 14 | SEM micrograph showing PA nanofiber bundles are of larger diameter in hydrogel formed with heat treated PA solution. Before gelation, solution in **(a)** was heated to 80°C and cooled to 25°C, solution in **(b)** was maintained at 25°C. (Images courtesy of Dr. Alvaro Mata)

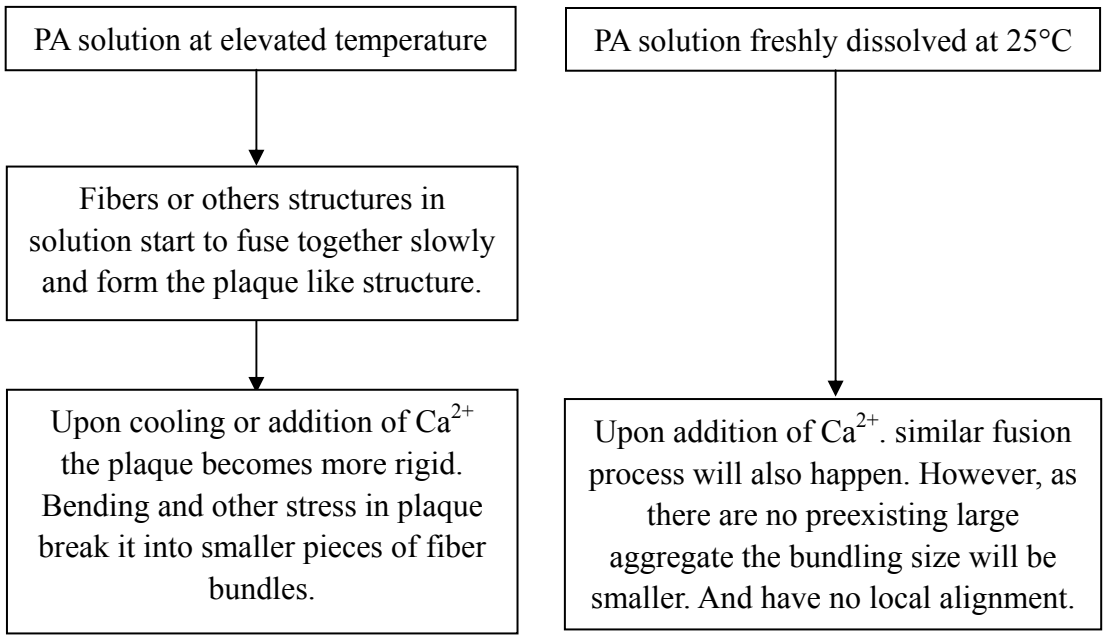

Figure 15 | Proposed mechanism, impact of heating

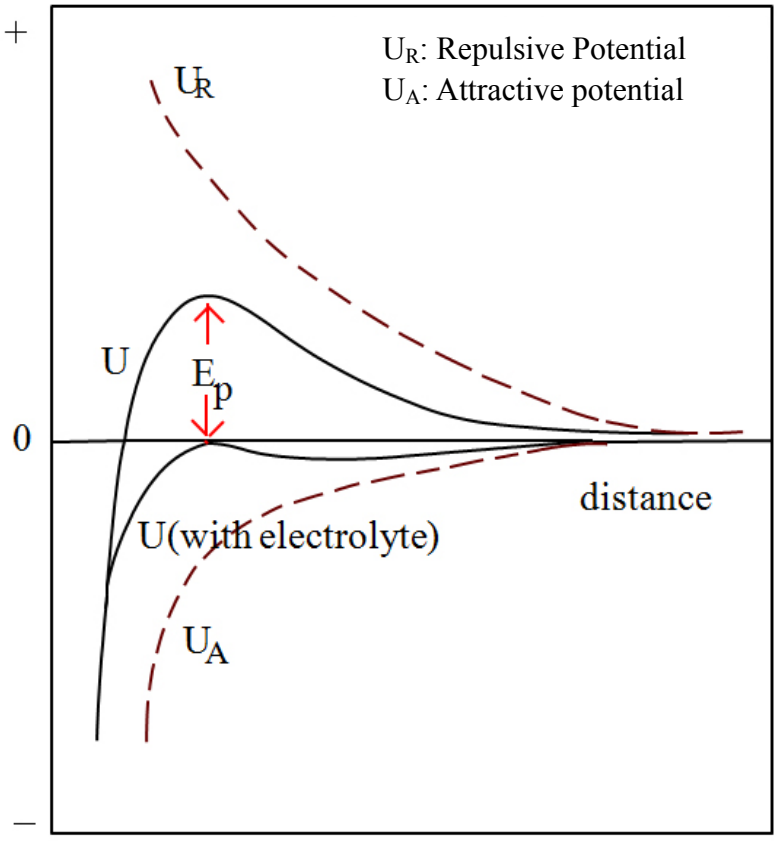

Figure 16 | DLVO theory suggests that the stability of a colloidal system is determined by the sum of van der Waals attractive (U_A) and electrical double layer repulsive (U_R) forces that exist between particles as they approach each other due to the Brownian motion they are undergoing. This theory proposes that an energy barrier resulting from the repulsive force prevents two particles approaching one another and adhering together. But if the particles collide with sufficient energy to overcome that barrier, the attractive force will pull them into contact where they adhere strongly and irreversibly together. [102]

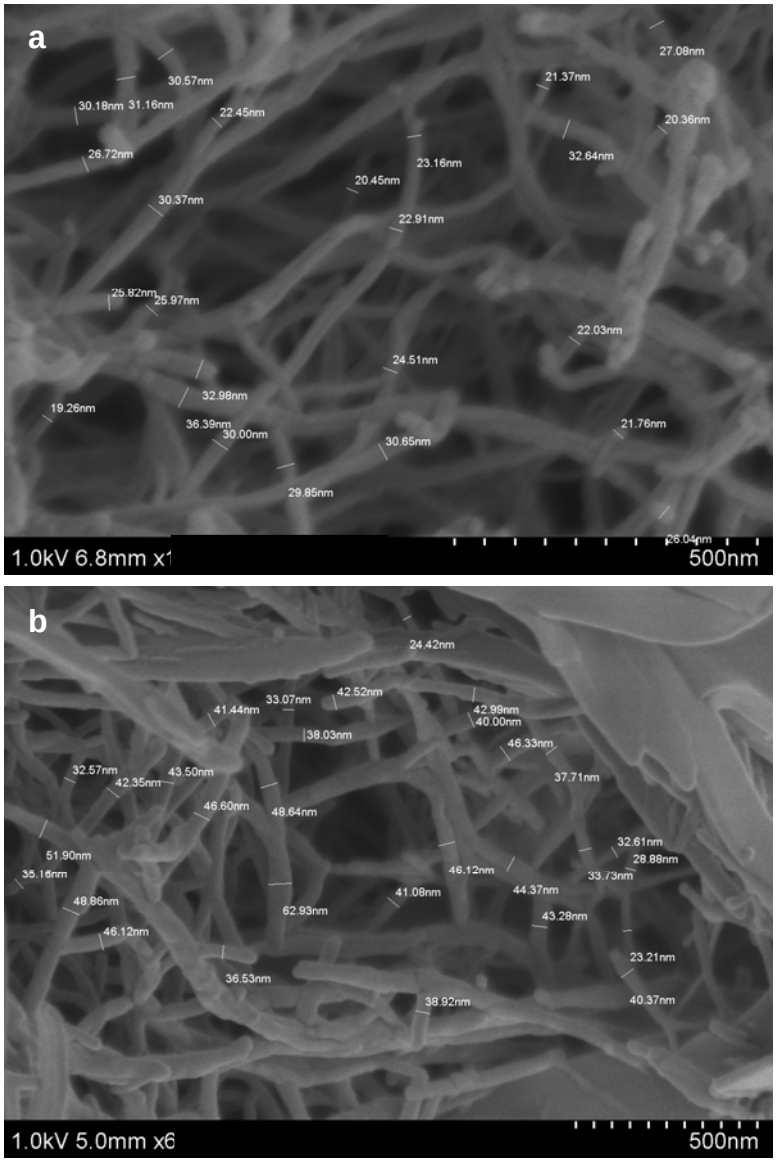

Figure 17 | Comparison of fiber bundle diameter between PA dissolved in water **(a)** and PBS **(b)**. Result shows that the average diameter are 26.7 ± 4.6nm in **a,** and 40.3 ± 8.2nm in **b.** (Images courtesy of Dr. Alvaro Mata)

2.4 Discussion

We just discussed how elevated temperature can facilitate and lead to the observed transition in self-assembly process. While temperature was the main experimental consideration, data revealed that several other factors, such as pH value, aging and screening ions should also be taken into account in the complicated self-assembly process.

2.4.1 pH Value

As illustrated in Figure 5, PA molecules used in this study usually contain a hydrophobic tail (denoted as **T**), a β-sheet forming peptide segment (denoted as **β**), a charged peptide segment (denoted as **C**) and epitope block (denoted as **E**). During self-assembly process, the hydrophobic collapse and hydrogen bonds in **T** and **β** induce the assembly and aggregation. The charged head group helps the molecules to dissolve in water and counterbalances assembly and aggregation process by electrostatic repulsion. Epitope block may also hinder assembly through steric effects. The dynamic balance between these forces facilitates or inhibits PA self-assembly. As a simple way to change the assembly, we can adjust the electrostatic repulsion among molecules by changing pH or the number of carboxyl/amine groups in PA molecules, without changing other segments. In Figure 18, we performed pH-dependent CD study using three different PA molecules. These PA molecules contain two, three or four carboxyl groups and were dissolved at pH 6, 8 and 10. The results showed that for a PA that has three or four carboxyl groups (Figure 18 a-b), electrostatic repulsion becomes dominant and disrupts β-sheet formation at high pH.

However, when pH value is lowered or PA has fewer carboxyl groups, β-sheet structure can form regardless of solution pH. This result can be explained by the change of electrostatic repulsion among deprotonated PA molecules. When the electrostatic repulsion is too strong, β-sheet structures diminish and PA molecules are less likely to self-assemble into high-aspect-ratio nanofibers. Gels made from such solutions are therefore very weak. Shown in Figure 19, 10 mM $C_{15}H_{31}$CO-VVVAAAEEE (COOH) PA was adjusted to pH 7.5 or 10. After heating and cooling, solution was gelled with $CaCl_2$. The great contrast of G' between these two samples proved that the dominance of adhesion forces (from **T** & **β**) over repelling forces (from **C** & **E**) is required for self-assembly of nanofibers. The influence of pH value on PA self-assembly is independent of temperature. However, it could greatly strengthen or weaken the impact of heat treatment we saw earlier in this chapter.

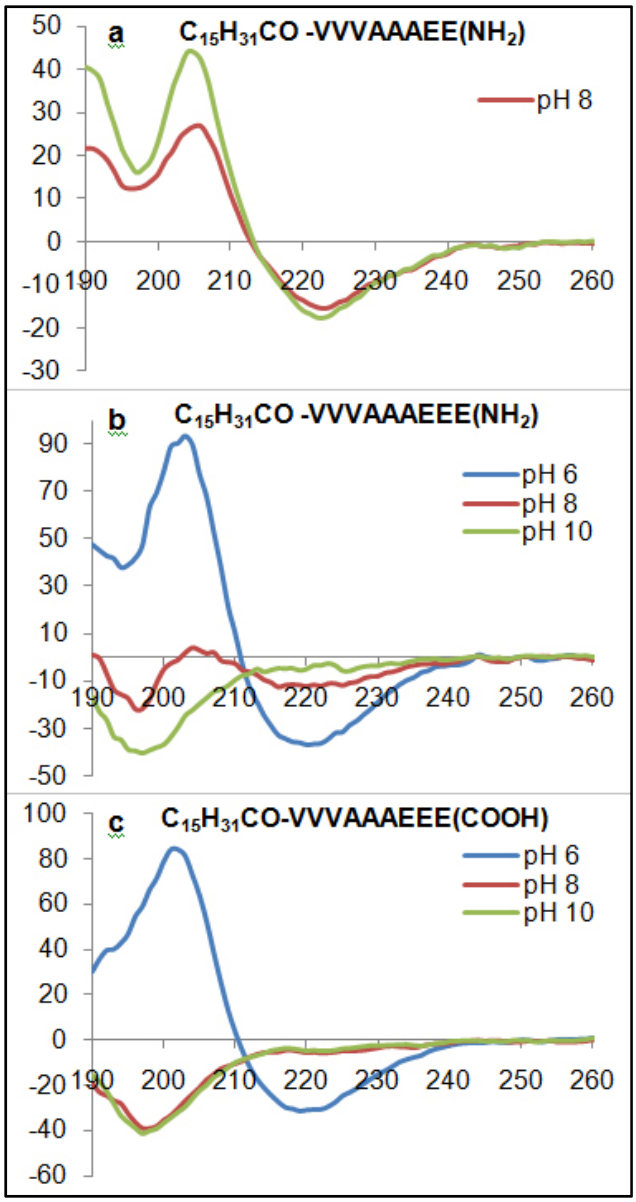

Figure 18 | CD Scan of three PA molecules at pH value 6, 8 and 10; Tested PA molecules are **(a)** $C_{15}H_{31}CO$-VVVAAAEE(NH_2) **(b)** $C_{15}H_{31}CO$-VVVAAAEEE(NH_2) and **(c)** $C_{15}H_{31}CO$-VVVAAAEEE(COOH), containing two, three and four carboxyl groups *(molecule in* ***(a)*** *is not soluble at pH 6, that data is not available).* The results showed that for PA has three or four carboxyl groups, electrostatic repulsion becomes dominant and disrupts β-sheet formation at high pH. However, when pH value is lowered or PA has fewer carboxyl groups, β-sheet structure can form regardless of solution pH.

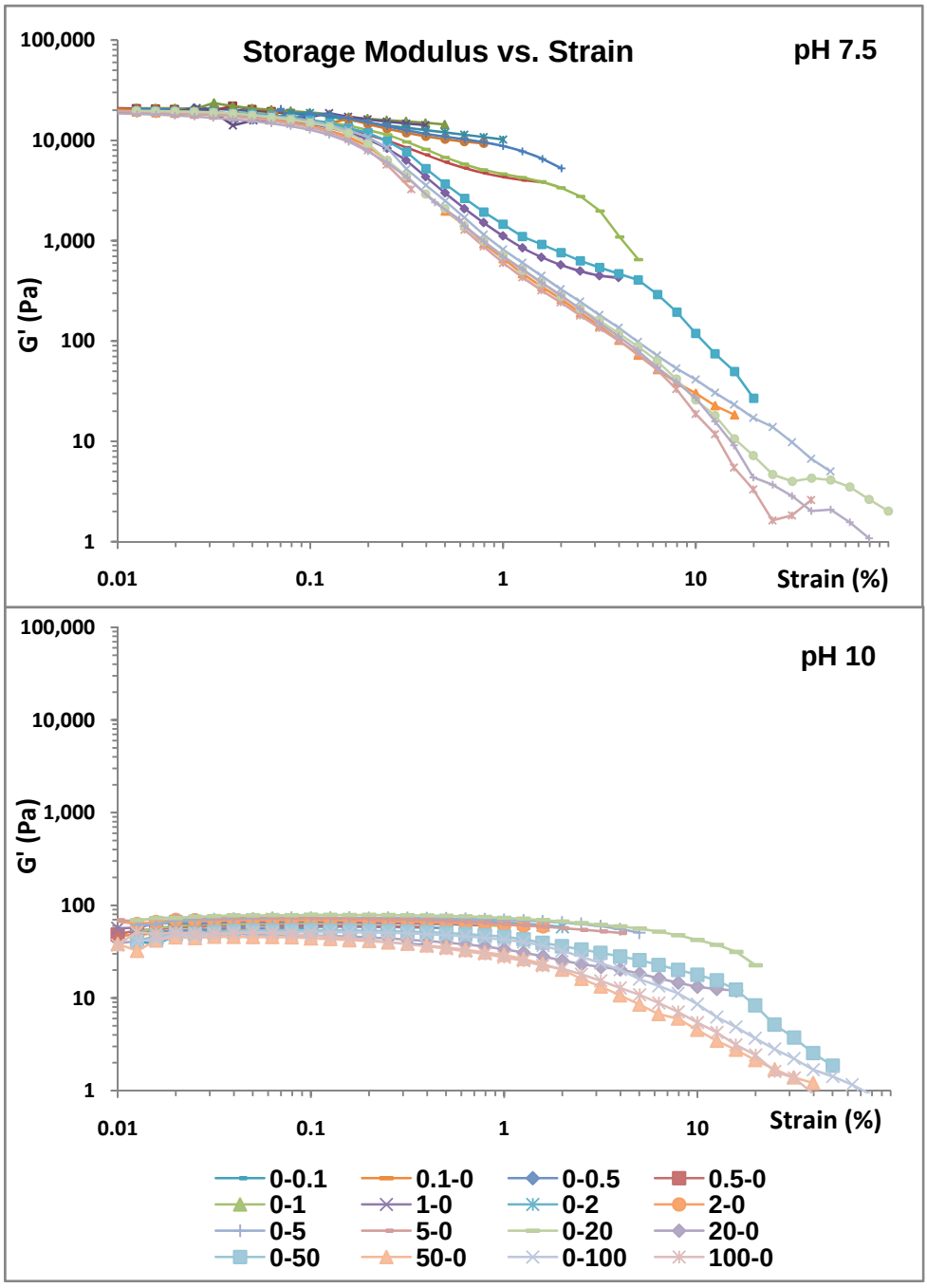

Figure 19 | Storage modulus decrease sharply when pH value is adjusted to increase electrostatic repelling force between molecules. 10mM $C_{15}H_{31}$CO-VVVAAAEEE(COOH) PA was used in this study and the final calcium concentration was 25mM.

2.4.2 Aging

During the study, we also found that the PA solution (0.5-2.0 wt%) becomes more viscous with aging. While CD study showed no changes between freshly prepared and seven day old samples (see Figure 20 and Figure 36) during heating and cooling, other characterization methods (SEM, QFDE/TEM and POM) all showed increasing fiber length and orientation order in aged samples (see Figure 21 and Figure 22). We think reorganization of dynamically trapped structures leads to this change. However, the change is slower and less significant comparing to the heating and cooling process.

2.4.3 Screening Ions

Addition of monovalent ions can affect self-assembly process from two aspects. On one hand it facilitates coagulation process as mentioned in section 2.3.4. On the other hand, it also change the packing parameter of surfactants [106]. Equation for estimating packing parameter is given as $P=V_0/(a_0*l_0)$ (see Figure 23). While the addition of monovalent ions has little effect over hydrocarbon volume V_0 and critical length of hydrocarbon chain l_0, it could reduce the area of the head group a_0. However, as we can make PA noodle structure both in water and PBS solution, the addition of screening ion does not seems to be a critical factor in the range of 0-160 mM monovalent ions concentration (PBS contains around 160 mM monovalent ions).

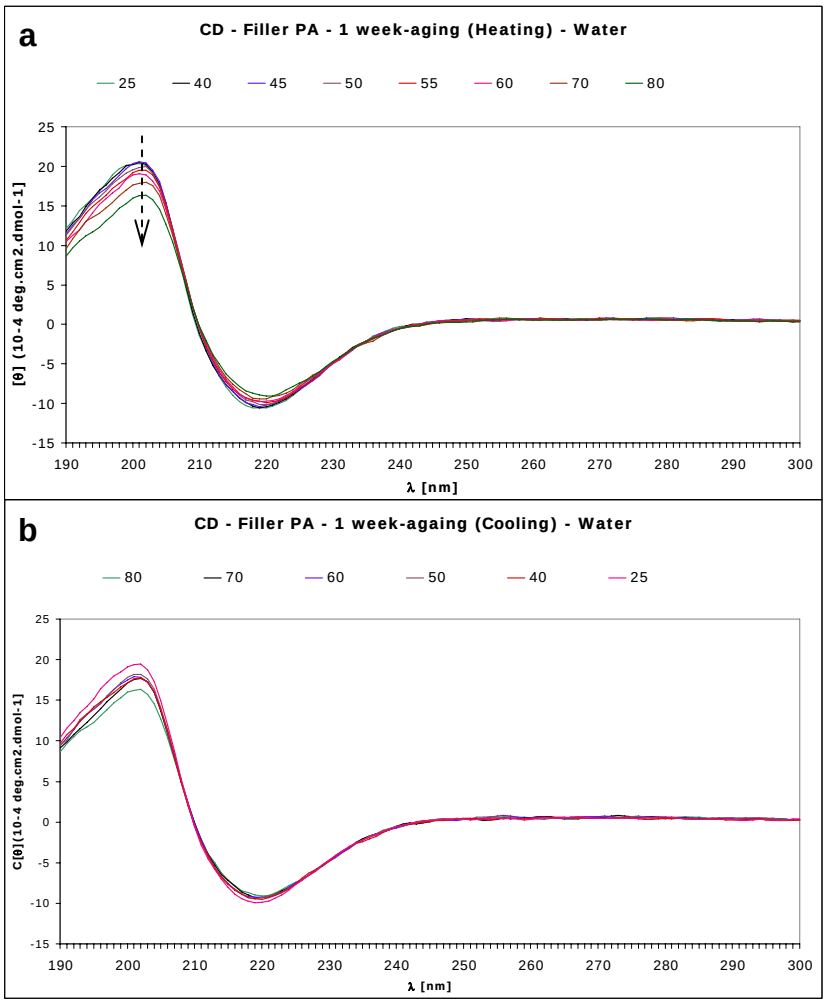

Figure 20 | CD scans from 1 week aged 0.01 wt% $C_{15}H_{31}CO$-VVVAAAEEE(COOH) PA solution at different temperatures during heating up and cooling down cycle. **a,** Scan while heating up; **b,** Scan while cooling down. Comparing to Figure 36, there is no significant difference. (Figures courtesy of Dr. Conrado Aparicio)

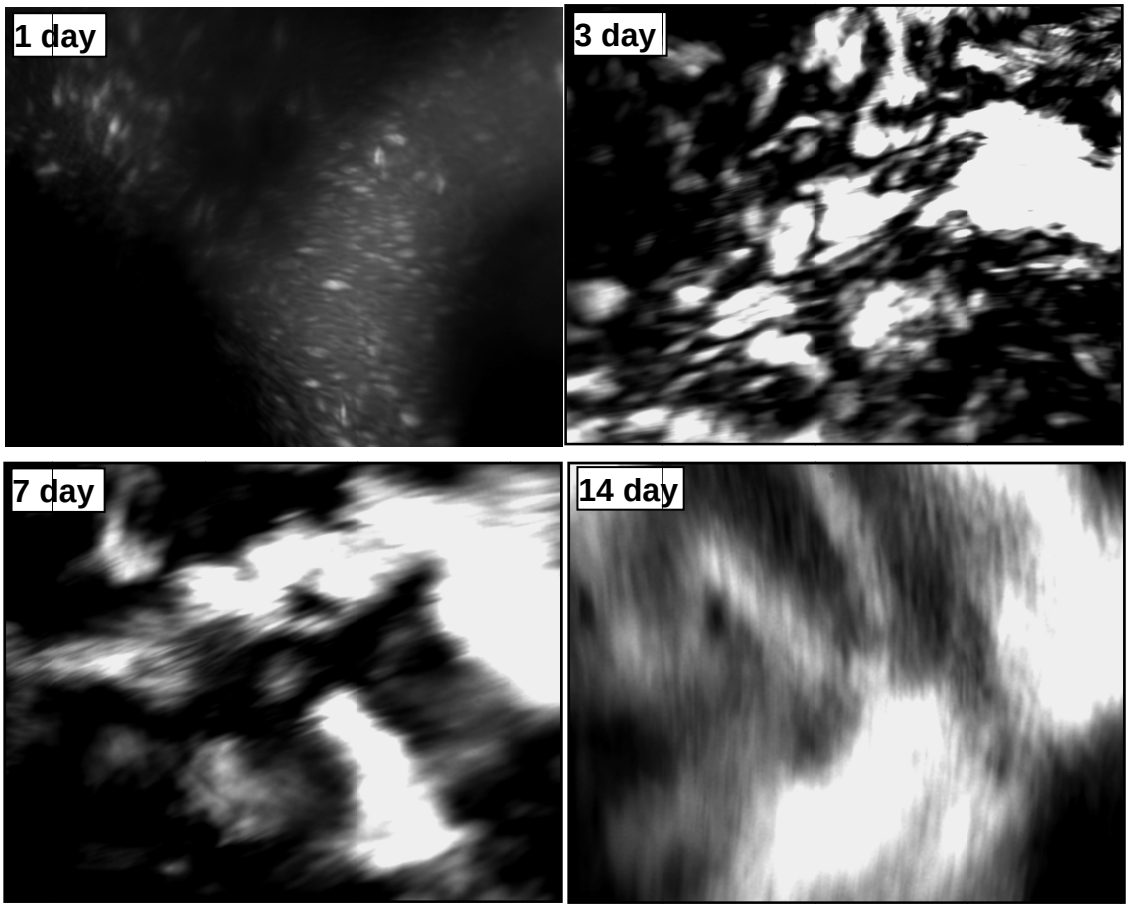

Figure 21 | Birefringence study of 1% $C_{15}H_{31}CO$-VVVAAAEEE(COOH) PA in Water after 1, 3, 7 and 14 day; With time, the birefringent domains became larger and brighter, indicating increased order in the PA solution. (Images courtesy of Dr. Alvaro Mata)

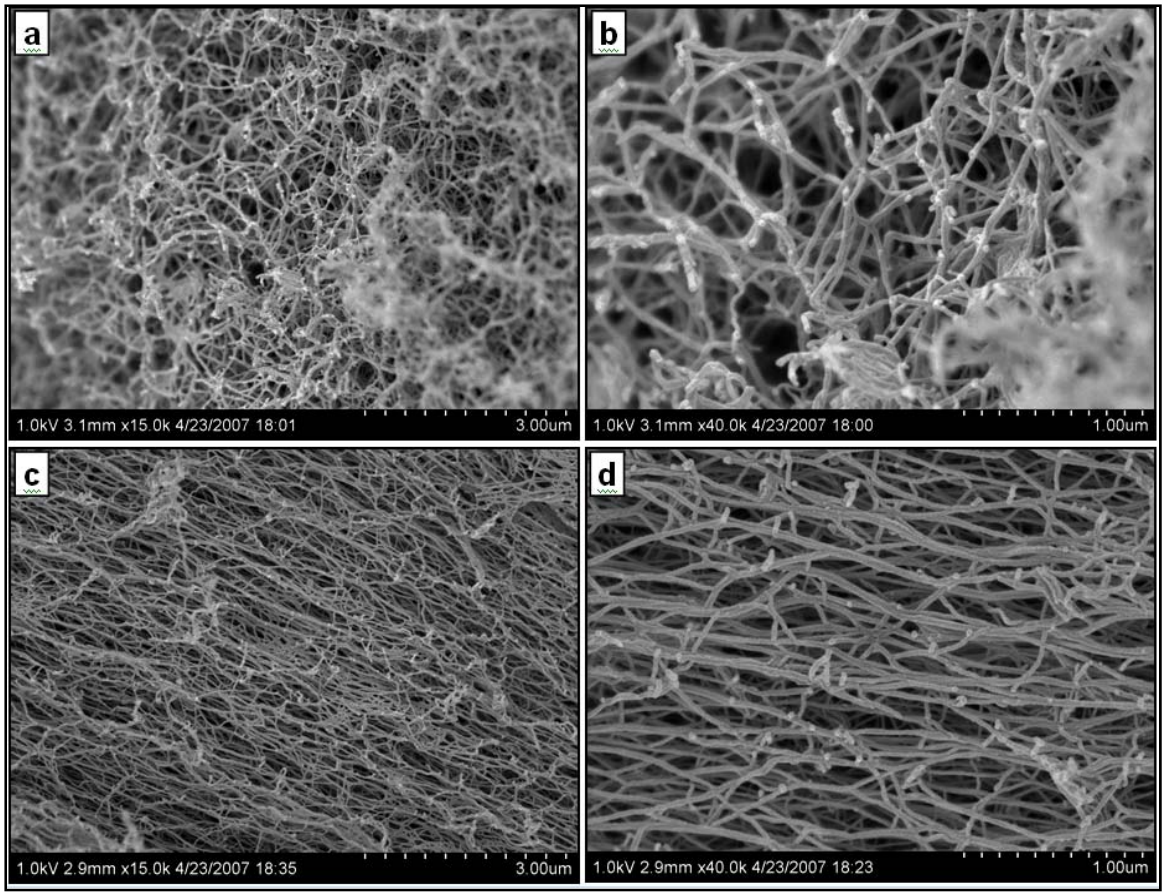

Figure 22 | SEM of PA gel made with aged $C_{15}H_{31}CO$-VVVAAAEEE(COOH) solution. **a,b** 1 day aging; **c,d**, 14 days aging. Results showed increasing order with aging time. (Images courtesy of Dr. Alvaro Mata)

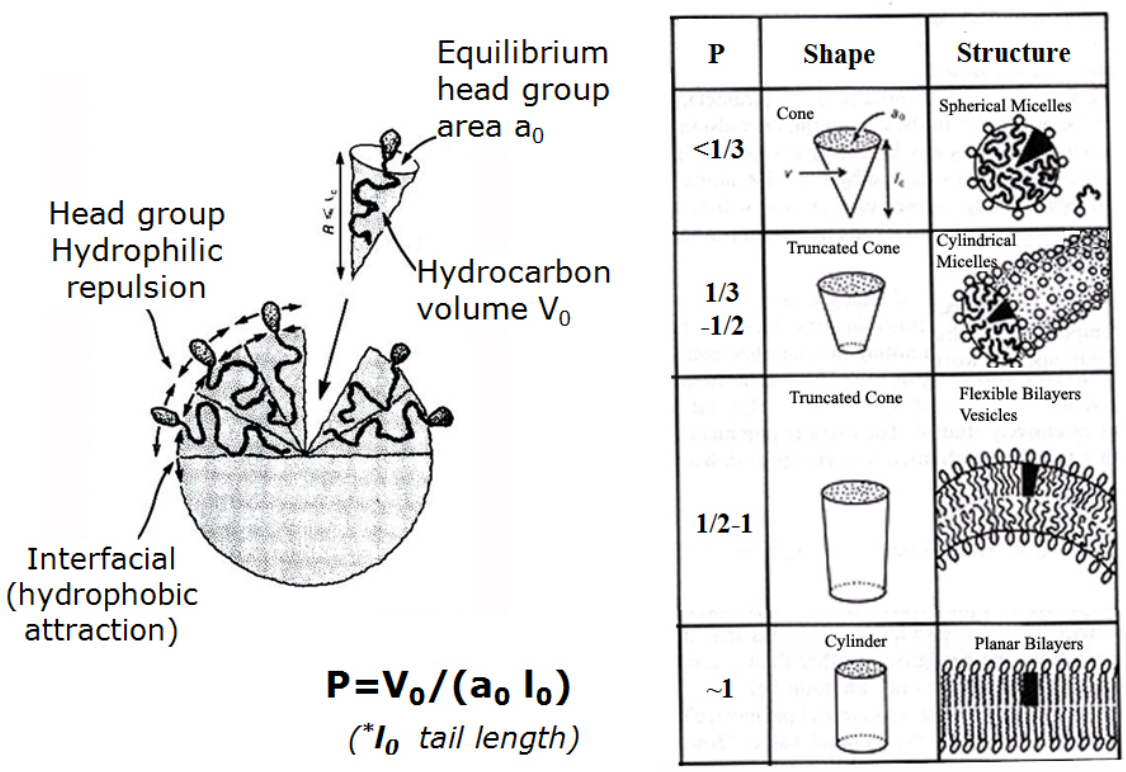

Figure 23 | Packing Parameter: definition (left) and its role in defining self-assembly structures (right) (adapted from Israelachvili, Intermolecular & Surface Forces, 1985).

2.4.4 Steric Effects

Besides pH value, aging and screening ions, steric effects are another important consideration for self-assembly. As shown in Dr. Liang-Shi Li's work in our group [107], torsional strain caused by steric repulsion between the bulky substituents may overwind the β-sheets. Muraoka and Paramonov also demonstrated how steric effects can influence self-assembly and derived materials properties. [83, 108]. Our observation in tested PA noodle candidate molecules agreed with this point. In Table 1 (see supporting evidences 2.8.1) PA with different design were synthesized. After heating and cooling, PA molecules with longer sequence were less likely to form PA noodle structures as those shorter ones. Therefore, steric effects are something definitely needs our attention.

2.4.5 Long Range Alignment and Deborah Number

In earlier session of this chapter, we learned that environmental factors such as temperature, pH, etc can template the formation of larger fiber bundles. But how does this change in nanostructures lead to the potential alignment over arbitrary length? Theoretical models suggests that during the processing of polymeric nematics, if the product of strain rate ἑ and the conformational relaxation time λ (a.k.a. Deborah Number, De=ἑ*λ) is greater than unity individual molecules can experience significant viscous torques and become highly oriented in one direction [109]. In making the PA noodles scattered in Figure 9, we kept the longitudinal

strain rates constant (~4 1/s) in both heated and non-heated PA solution. With high degree of preferential alignment only happen in heated solution, it is apparent that the relaxation time of PA solution increased after heat treatment. Relaxation time is predicted to be extremely sensitive to molecular weight. It is therefore, the longer relaxation time that leads to larger De value and makes the previously infeasible long range alignment of PA nanofibers happen.

2.4.6 Comparison to Electrospinning

Electrospinning is a highly versatile method to process solutions or melts, mainly of polymers, into continuous fibers with diameters ranging from a few micrometers to a few nanometers [110]. When these fibers are collected by rotating wheels or frames, they can form a substrate that consists of aligned nanofibers. Here we would like to compare electrospinning with PA noodle system.

A standard electrospinning setup includes a spinneret, a syringe pump, and a collector plate (see Figure 24). When polymer solution or melt is extruded with high voltage difference (10 to 50 kV) between the spinneret and grounded collector plate, the flowing liquid is stretched into a thin fiber. This elongation process results in the fabrication of uniform fibers with nanometer-scale diameters. Although some researchers have tried encapsulating biological components such as bacteria, virus, etc [111, 112], electrospinning with mammalian cells is rare. The intolerance of mammalian cells to this process probably dues to the high strain rate occurs during electrospinning, which is sometimes as high as 10^4-10^5 1/sec. Most applications of

electrospinning are therefore based on culturing cells on top of collected aligned nanofibers [113, 114]. Another disadvantage of electrospinning is that most molten polymers or polymer/solvent systems are not cell compatible during processing. There are some water soluble polymers such as poly(vinyl alcohol) (PVA) and poly(ethylene oxide) (PEO) that can be used for electrospinning [110], but the options are limited. Additionally, as the solution needs to have a minimal level of viscosity in electrospinning, the concentration, molecular weight or both are usually in a region not favorable for cellular encapsulation. For example, the electrospinning solution needs to be 3.5-8 wt% for m.w. 146,000 PVA [115], or 8-37% Poly(ethylene glycol) (PEG) with 0.1-0.2 wt% PEO (PEG m.w. ~10,000, PEO m.w. > 500,000) [116].

For comparison, PA noodles are deformed at a strain rate ~ 4 1/s, which is much lower and more compatible with cells. The versatility of PA molecules also endows us the capability to make PA noodle of customized physical/chemical properties. Additionally, PA noodle system uses water as solvent and requires a PA concentration as low as 0.5 wt%. All these features make PA noodle a better platform for biological applications.

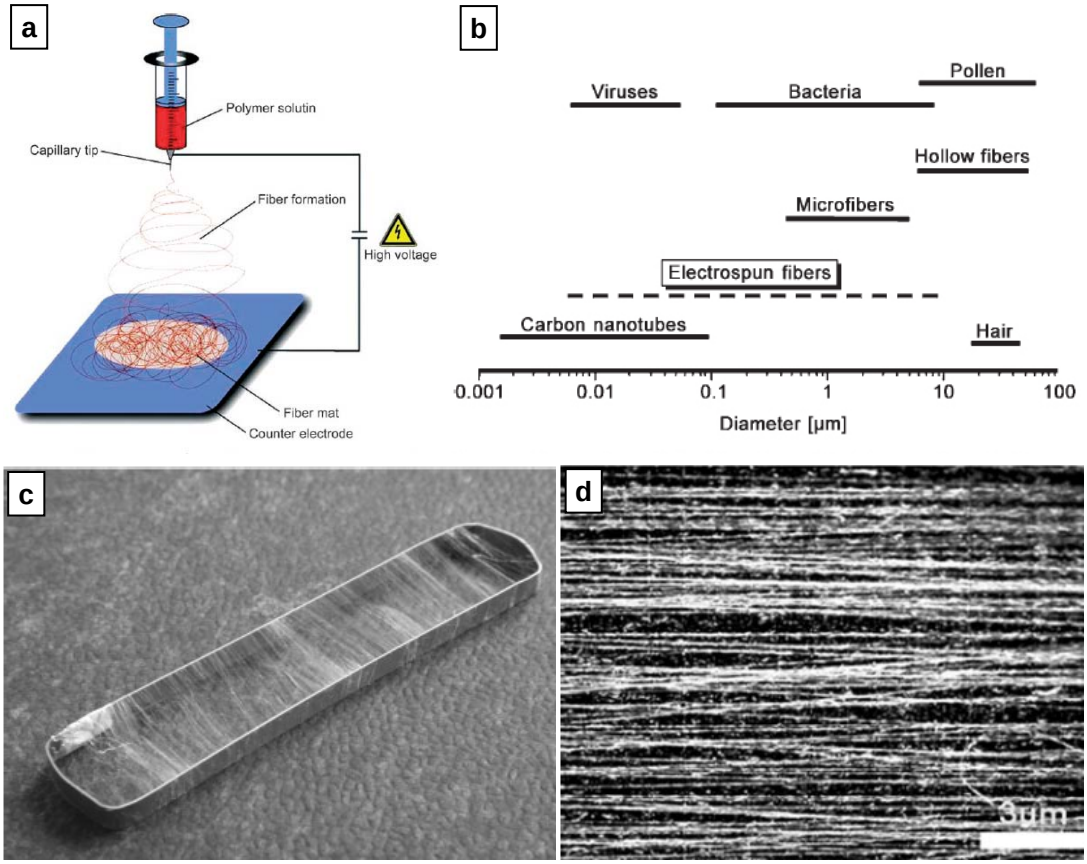

Figure 24 | Electrospinning **a,** A typical Electrospinning setup; **b**, Comparison of the diameters of electrospun fibers to those of biological and technological objects; **c,** Frame electrode used for obtaining parallel fibers; **d**, Parallel polylactic acid fibers obtained directly via the electrospinning process (reproduced from [110, 117]).

2.5 Applications

We explored the use of the macroscopic noodles composed of aligned PA nanofibers to direct the orientation of cells in 3D environments. After dispersing human mesenchymal stem cells (hMSCs) in thermally treated PA solutions, we manually dragged these solutions onto salty media to form noodle-shaped strings with encapsulated stem cells. These cells start to elongate along the fiber director axis within 12 hours. Optical, fluorescence, and electron microscopy (Figure 25) all demonstrated that both cell bodies and philopodia were aligned with PA fibrils in the extracellular space. These effects on hMSC orientation are hypothesized to result from contact guidance along the preferentially oriented matrix [118]. Clearly these arrays of aligned nanofibers could be used to guide cells in 3D without the use of surface patterning. We will explore this application in next chapter.

We also compared the osteogenic, chondrogenic and myogenic differentiation of these cells in the aligned environment with that of the same cells encapsulated in an isotropic network of nanofibers. After culturing the cells for two weeks, real-time reverse-transcriptase polymerase chain reaction (RT-PCR) revealed a significant difference in the course of differentiation between cells in the aligned versus isotropic environment (Figure 26). Result showed that, in Chondrogenic medium, hMSC cultured in isotropic hydrogel express more chondrogenic markers AGC1 and COL2A1. In osteogenic medium, hMSCs cultured in isotropic and aligned environments had opposite expression levels of ALP and OPN. As osteopontin is a negative

regulator in the early stage of osteogenic differentiation [119], the aligned environment is more osteogenic. In growth medium, hMSCs cultured in aligned hydrogel gel have more DES expression, indicating further myogenic development. Therefore in chondrogenic media, hMSCs were further differentiated when cultured in isotropic hydrogel. However, in osteogenic media and growth media, hMSCs are more differentiated in aligned environment. From these results, an aligned 3D environment can be useful to mediate stem cell differentiation. Important variables for differentiation within bulk aligned matrices may include mechanotransduction of signals, cell polarization, and matrix-mediated isolation of cells. Future work will explore the biological basis of these observations, which may be related to the synergistic effects of matrix stiffness [120] and nanofiber alignment on cell differentiation.

A “cellular wire” based on the noodle construct could be used to fabricate sophisticated engineering device or direct neuron cells spatially for function (Figure 27). We were also able to create a noodle construct with dispersed carbon nanotubes that retains the same degree of fibril alignment observed by SEM in pure PA strings (Figure 28). These “black noodles” had electrical conductivities on the order of 1–10 S/cm in a dry state, depending on the concentration of carbon nanotubes.

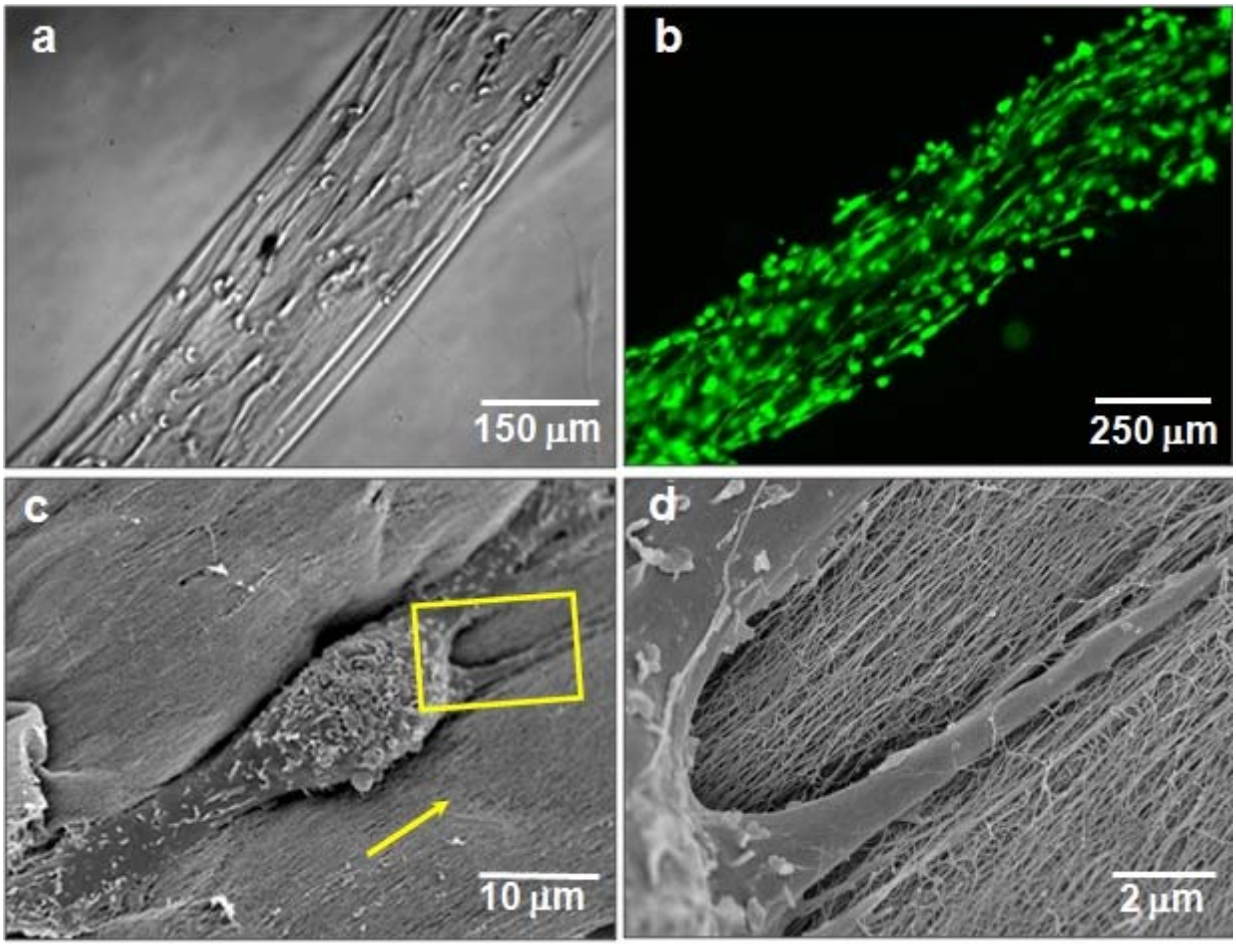

Figure 25 | Cell alignment in strings of aligned fibrils. **a**, Preferential alignment of encapsulated human mesenchymal stem cells (hMSCs) along the noodle axis. **b**, Calcein-labeled aligned cells cultured in noodle. **c**, **d**, SEM images at different magnifications of a single cell in the noodle structure (arrow indicates the alignment direction).

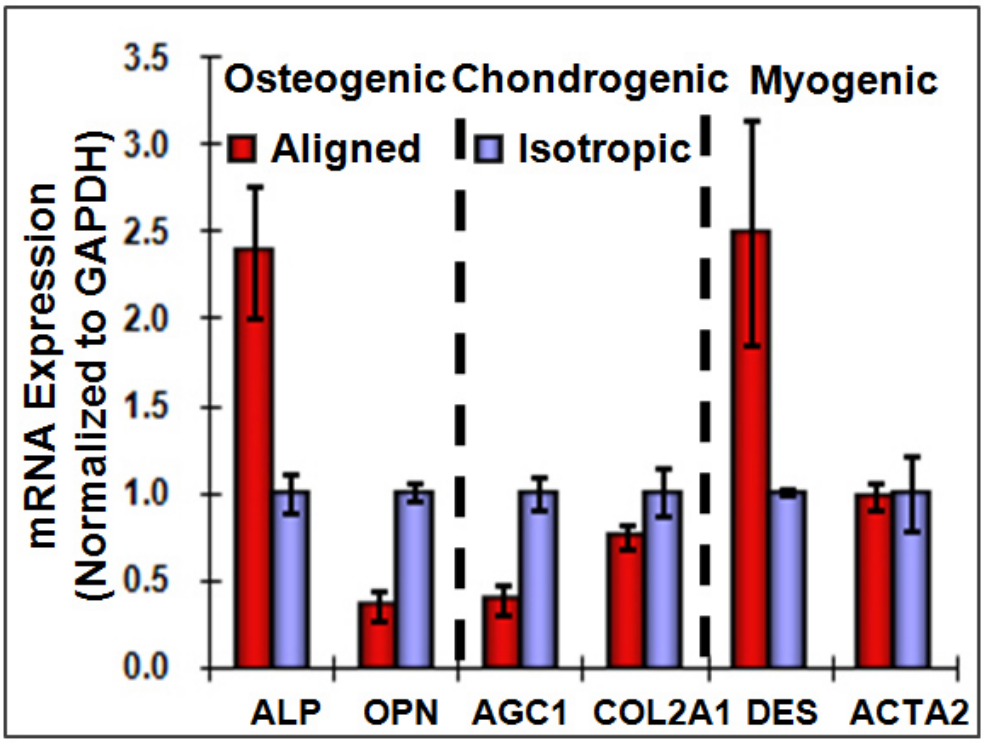

Figure 26 | RT-PCR anaylysis of hMSCs differentiation in aligned *vs.* isotropic environments. The bar graph shows the relative mRNA expression measured by RT-PCR of six marker genes for three different lineages (normalized to GAPDH): alkaline phosphatase (ALP) and osteopontin (OPN) as bone cell markers; aggrecan (AGC1) and collagen II alpha I (COL2A1) as cartilage markers; desmin (DES) and alpha smooth muscle actin (ACTA2) as muscle cell markers. Error bars represent the mean ± standard deviation of the mean for triplicate samples.

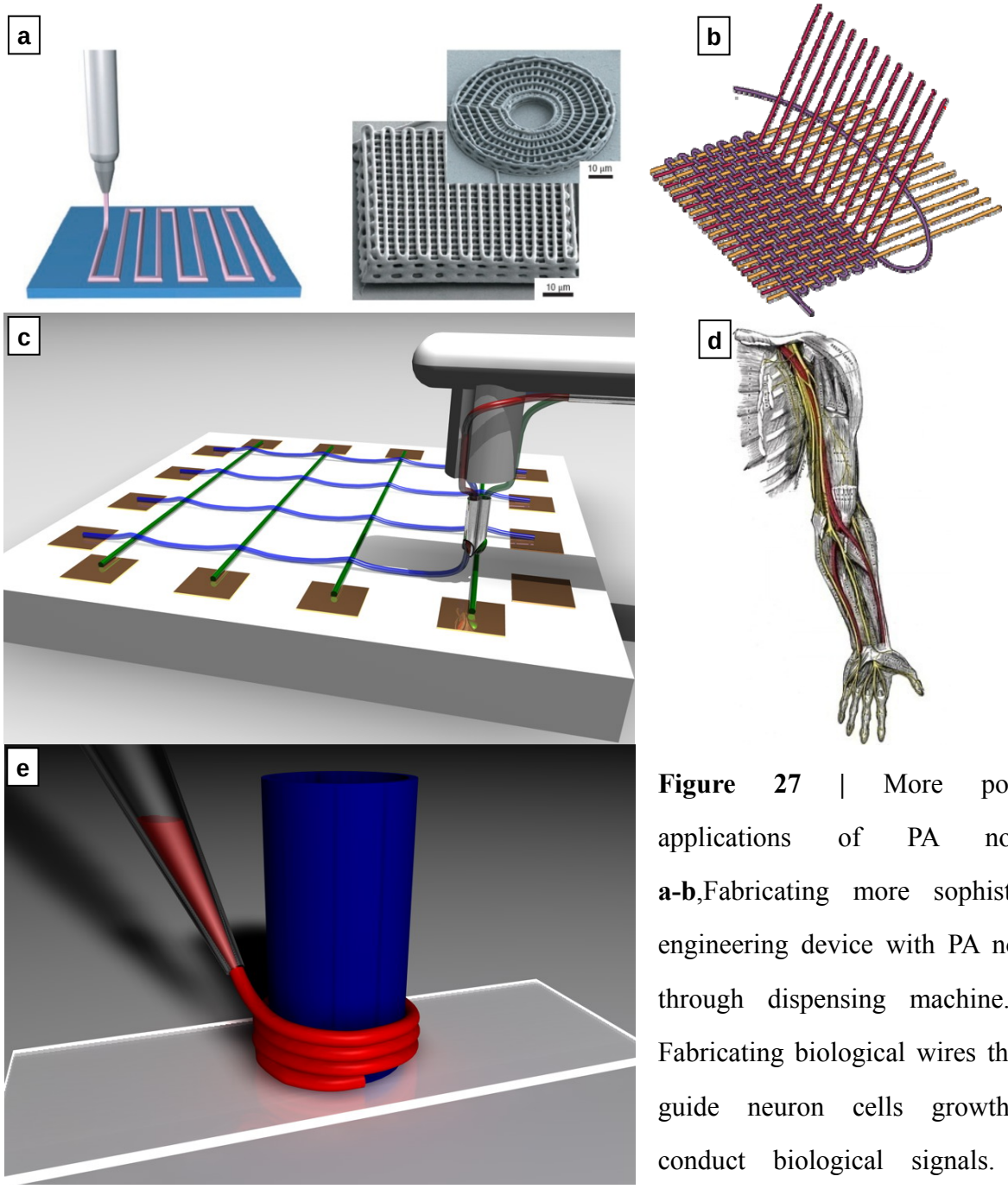

Figure 27 | More potential applications of PA noodles. **a-b**,Fabricating more sophisticated engineering device with PA noodles through dispensing machine. **c-d,** Fabricating biological wires that can guide neuron cells growth and conduct biological signals. Such wires can be used to study cellular communication and replace damaged nerves in human body. **e** Wrapping PA noodle around scaffold materials to achieve desired cellular orientation on scaffold. (**a** is reproduced from [121], **c,e** image courtesy of Mark Seniw, **d** is reproduced from Answers.com)

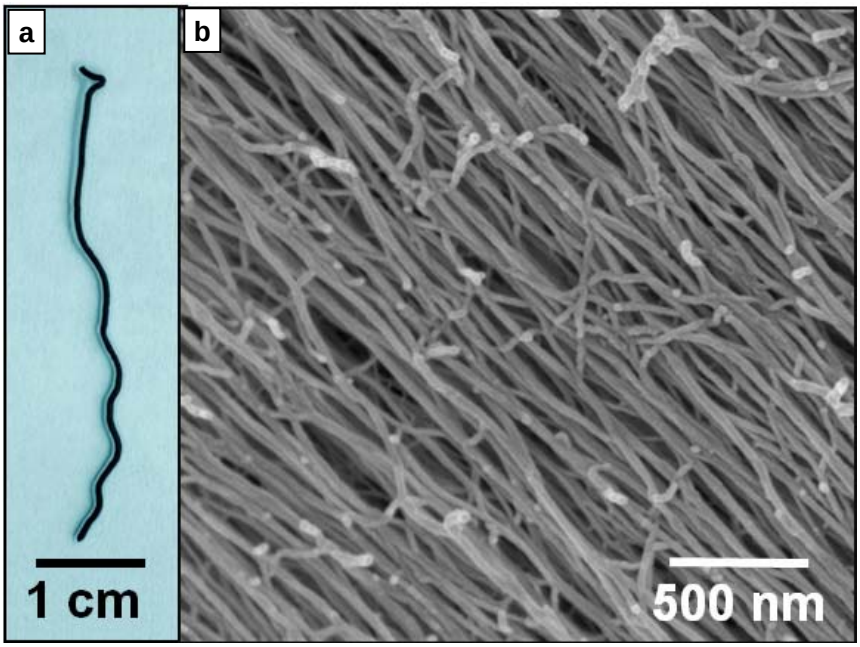

Figure 28 | Example of using PA noodle with other materials. **a,** A "black noodle" formed with PA and carbon nanotubes. **b,** SEM micrograph showing aligned fibrils in the black noodle (SEM image courtesy of Jason Mantei and Dr. Alvaro Mata).

2.6 Summary

In this chapter we have described a thermal energy pathway that greatly changes self-assembly process and results in different final macroscopic structure. The roles of several other factors, such as pH value, aging, etc, were also studied. With these developments, we were able to create aligned PA nanofibers over arbitrary length. The alignment of PA nanofibers usually requires extensive surface patterning or the use of strong mechanical forces. Here it can be easily accessed from an aqueous solution using a minimal applied force. We have demonstrated some interesting biological applications for these systems, but with different chemistries they could also be useful to template macroscopic orientation of one-dimensional nanostructures for nonbiological applications.

2.7 Experimental Details

2.7.1 PA Molecules That Can Be Made Into Noodle after Heat Treatment

Table 1 | Tested PA Noodle Candidates

Tested PA Noodle Candidates		Forming Noodle?
PA1	$C_{15}H_{31}CO$-VVVAAAEEE(COOH)	Yes
PA2	$C_{15}H_{31}CO$-VVVAAAKKK(COOH)	Yes
PA3	$C_{15}H_{31}CO$-VVAAEE(NH_2)	Yes
PA4	$C_{15}H_{31}CO$-VVVAAAEEEGS(P)G(COOH)	Yes
PA5	$C_{15}H_{31}CO$-VVVEEE(COOH)	Yes
PA6	$C_{15}H_{31}CO$-IIIEEE(COOH)	Yes
PA7	$C_{15}H_{31}CO$-VVVAAAEEEGRGDS(COOH)	NO
PA8	$C_{15}H_{31}CO$-VVVAAAEEEGIKVAV(COOH)	NO
PA9	$C_{15}H_{31}CO$-AAAAGGGEEE(COOH)	NO
PA10	$C_{11}H_{23}CO$-KVVVAAAEEESGGGYPVHPST(NH_2)	NO

2.7.2 Rheology Study

Rheological data were collected with a Paar Physica Modular Compact Rheometer 300 operating in 25 mm parallel-plate configuration. All samples had a total volume of 300 μL. Once the gels were formed, the top plate was lowered onto samples to a gap distance of 0.5 mm. Mineral oil was dropped around the edge of the plate and wet tissues were placed at the perimeter of a chamber around the gel to minimize evaporation. The stage temperature was maintained at 37°C by a Peltier heating system. Samples were allowed to equilibrate one hour

before testing. Strain sweeps were preformed on all samples to determine the linear viscoelastic regime. Gels were tested at 0.5% oscillatory strain from 100 to 1 rad/s. G′ and G″ were averaged over a minimum of two trials. Samples were prepared by gelling 0.75 wt % PA ($C_{15}H_{31}CO$-VVVAAAEEE(COOH)) solutions (with or without heat treatment) with $CaCl_2$ (Figure 29). Result shows that for filler PA that had heat treatment history has a significant increase on both storage and loss modulus. On average a fourfold increase in storage modulus can be found in samples that have been heat treated over those without heat treatment.

Rheology studies described above were carried out on gels formed with PA solutions and Ca^{2+}. The differences between PA solution with and without heat treatment might have been overwhelmed by the existence of Ca^{2+}. A temperature dependent viscosity study was performed to compare these two conditions before gelling with Ca^{2+}. In this study, PA solutions were maintained at 25°C, 50°C and 80°C for half an hour before cooled back to 25°C. The solutions were then mixed with fluorescent polystyrene beads with three or four times of pipetting. Using a homemade high speed camera, the movement of fluorescent beads were tracked and used to calculate viscosity of PA solution. PA concentration used was 1.0 wt%.

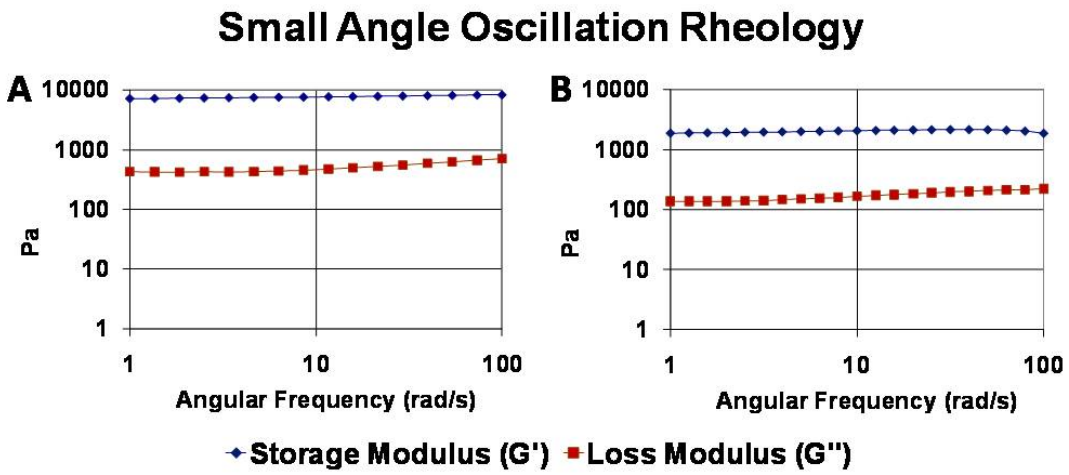

Figure 29 | Frequency sweep of a gel formed with PA. **a**, after heat treatment and **b**, before heat treatment.

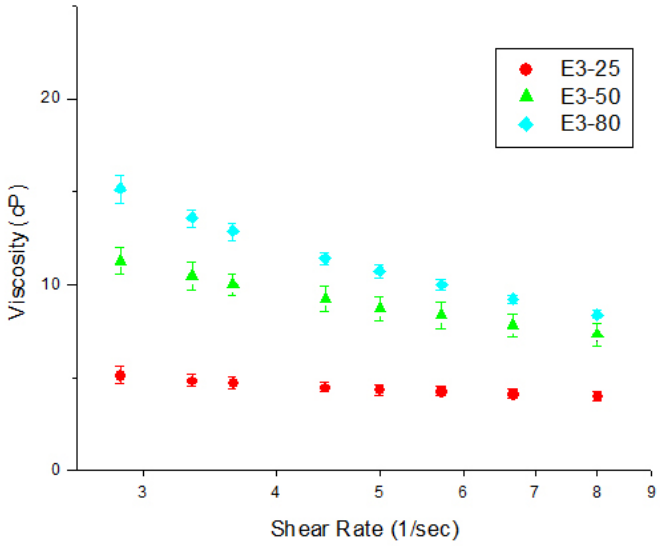

Figure 30 | PA solution's viscosity changes with heating temperature and shear rate; Change shows that when heat treatment temperature increase from 25°C to 80°C, viscosity of 1.0 wt% filler PA solution increases approximately 2-3 times without adding divalent cations, such as Ca^{2+}. Viscosity of PA solution decreases with increasing shear rate. (Figure courtesy of Ryan Forster)

2.7.3 Temperature Dependent SEM Morphologies of PA Noodle

Critical point drying was used to preserve the structure of PA gels for SEM analysis. After the gels were made, the water was slowly exchanged with a gradient of water-ethanol mixtures until the gel was in 100% ethanol. The samples were then critically point dried in a Polaron E3000 Critical Point Drying Apparatus and sputter coated with 3nm of a gold palladium alloy in a Cressington 208 HR Sputter Coater. Samples were then imaged on a Hitachi S-4800 II SEM (Hitachi, Pleasanton, CA).

2.7.4 Capturing Plaque Structure with Ca^{2+}

$C_{15}H_{31}CO$-VVVAAAEEE(COOH) PA powder was dissolved in pure water at 1 wt% and placed in a water bath at 80°C. Separately, a 50 mM $CaCl_2$ solution was heated to 80°C in a hot water bath. After both solutions were equilibrated at 80°C for 5 minutes, the heated $CaCl_2$ solution was rapidly injected into the heated PA solution, resulting in the formation of a dense gel. This gel was prepared for SEM by critical point drying and imaged as described above. Sample composition was studied with energy dispersive X-ray spectroscopy (EDX) (Figure 32, Figure 33 and Table 2).

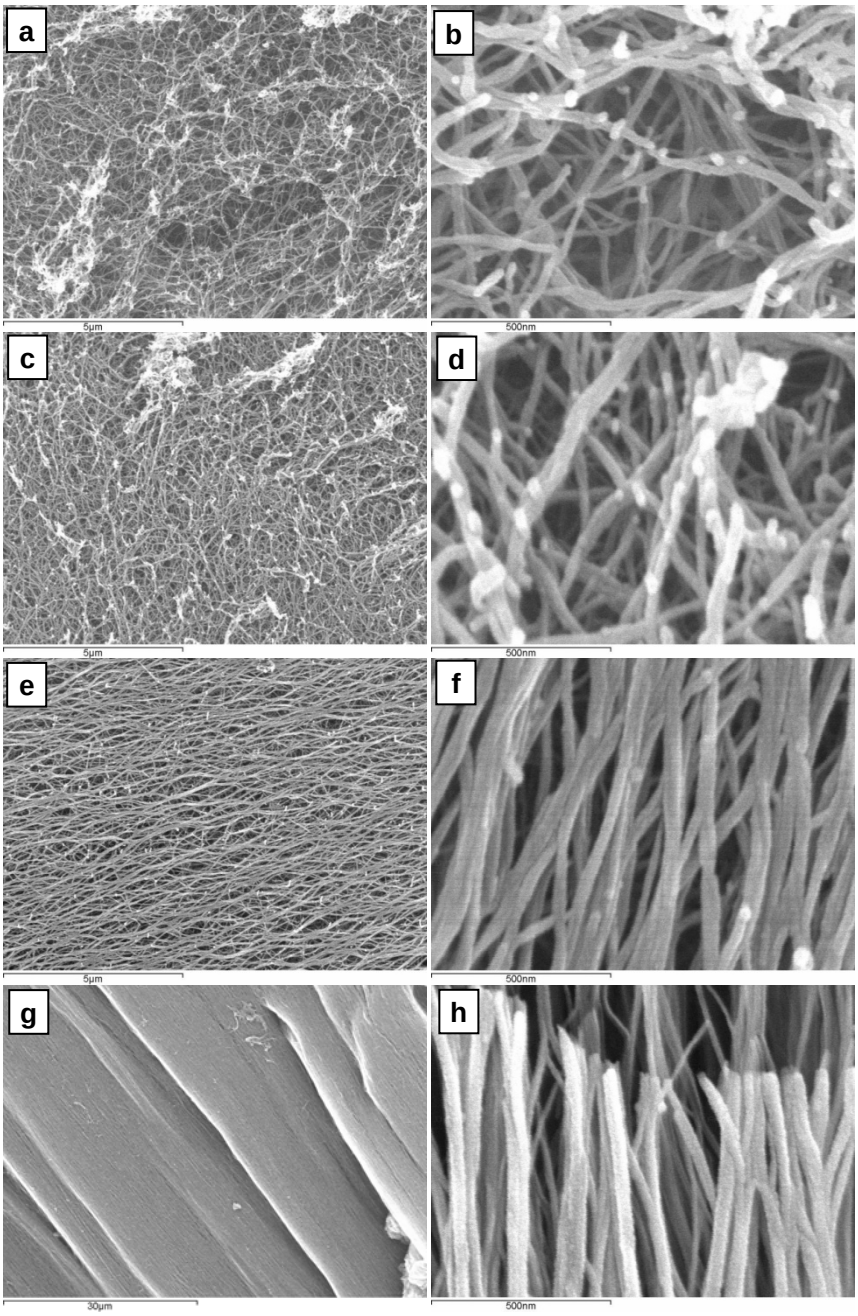

Figure 31 | SEM results showed PA noodle morphology transition with temperature. **a-b**, Room temperature gel, fibers are randomly intertwined. There is no orientation preference. **c-d,** PA was heated treated at 50°C before gelling. Fiber orientation in such gel is not obvious. **e-f,** PA was heated treated at 65 °C before gelling. Preferential orientation of fibers is observed, but not perfect. **g-h**, PA was heated treated at 80°C before gelling. Macroscopically aligned PA matrix can be formed with extensional flow.

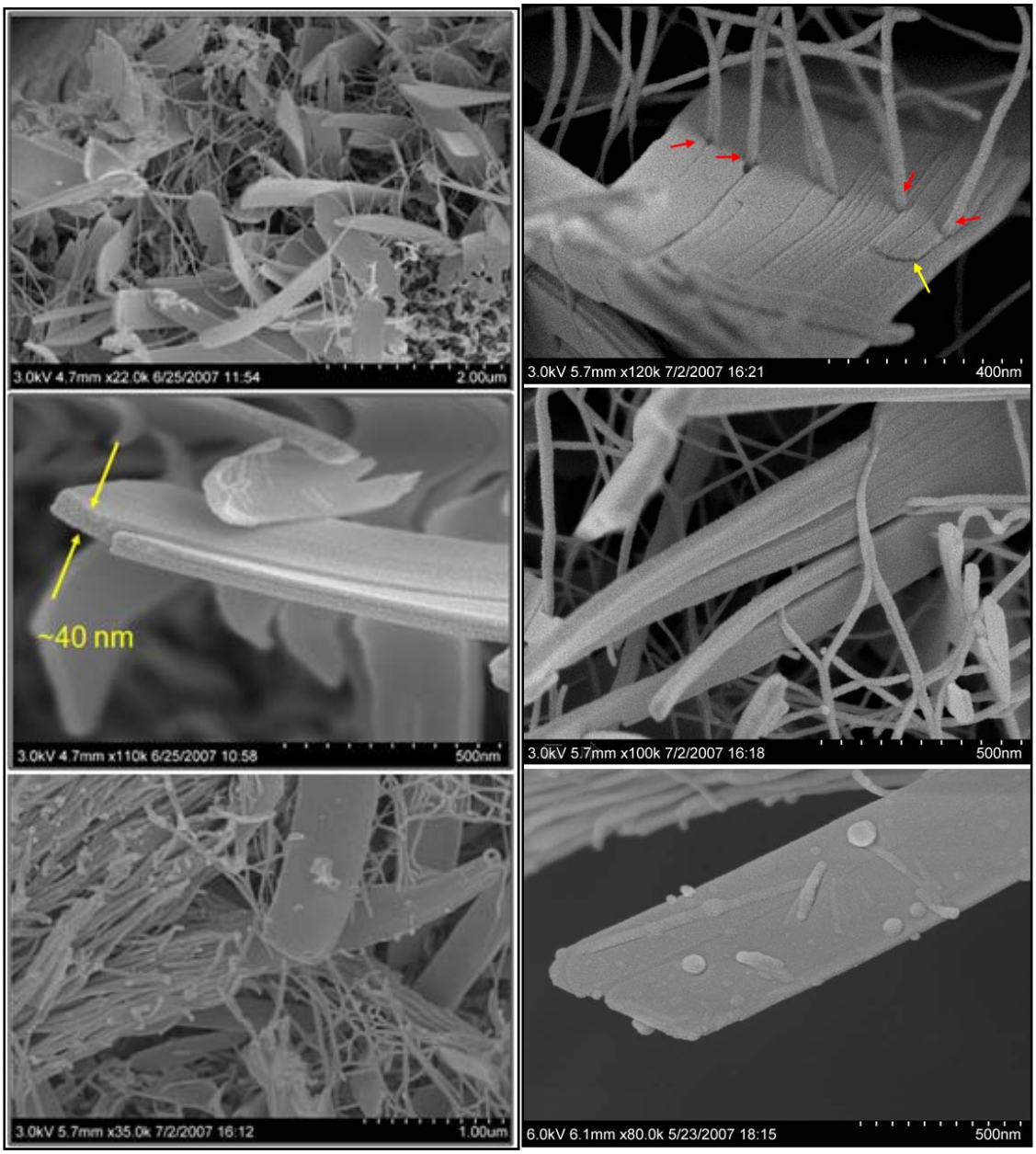

Figure 32 | Capturing self-assembly structure at 80 °C with Ca^{2+}. When Ca^{2+} ions are added at elevated temperature, some plaque-like structures crack and form bigger bundles of PA nanofibers.

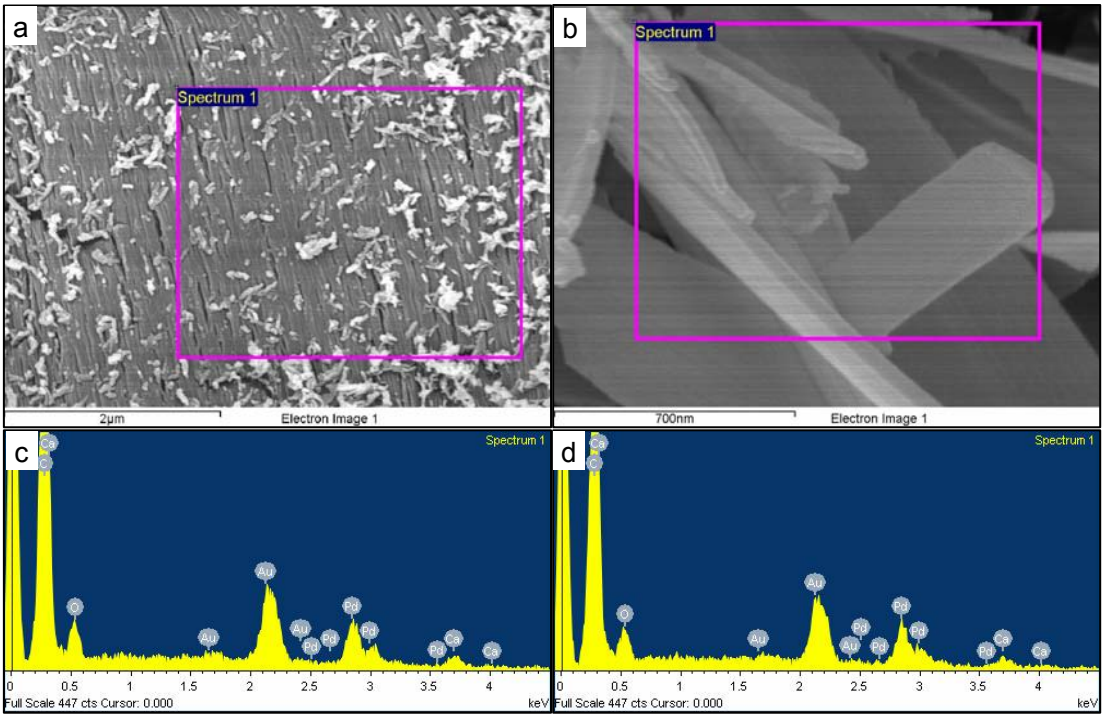

Figure 33 | EDX data shows that the composition of nanofiber bundles and plaque structures found in SEM samples have the same atomic compositions. **a**, **b**, SEM micrographs of dense fibers and plaque regions. **c**, **d**, EDX composition spectrum collected from boxed regions in **a** and **b**, quantitative data is listed in Table 2.

Table 2 | EDX composition analysis of nanofiber bundles and plaque structures formed by Ca^{2+} induced gelation at 80°C

Fibers Composition		
Element	Weight%	Atomic%
C K	42.56	79.84
O K	7.99	11.25
Ca K	2.87	1.61
Pd L	20.28	4.29
Au M	26.31	3.01
Totals	100.00	

Plaque Composition		
Element	Weight%	Atomic%
C K	41.28	80.33
O K	6.96	10.17
Ca K	2.69	1.57
Pd L	20.95	4.60
Au M	28.11	3.34
Totals	100.00	

2.7.5 Temperature Dependent QFDE

Our QFDE method was adapted from H.K. Lee*, et al.*[2]. Briefly, a 30-uL aliquot of sample was placed on an aluminum tab and slam frozen (Gentleman Jim Slam Freezing Apparatus) onto a copper block chilled to liquid nitrogen temperature (–195°C). After transfer into a freeze-fracture apparatus (Model CFE-40; Cressington Scientific Instruments, Watford, UK), the frozen sample was fractured, etched for 25 minutes at -95°C, rotary shadowed with a platinum–carbon mixture at a 20° angle, and then strengthened with carbon evaporated from a 90° angle overhead. The resulting replica was then separated from the organic sample and mounted on a copper grid for TEM observation. All samples were imaged with a JEOL 1230 Transmission Electron Microscope at 80 or 100kV. Figure 34 shows the morphologies transition with temperature.

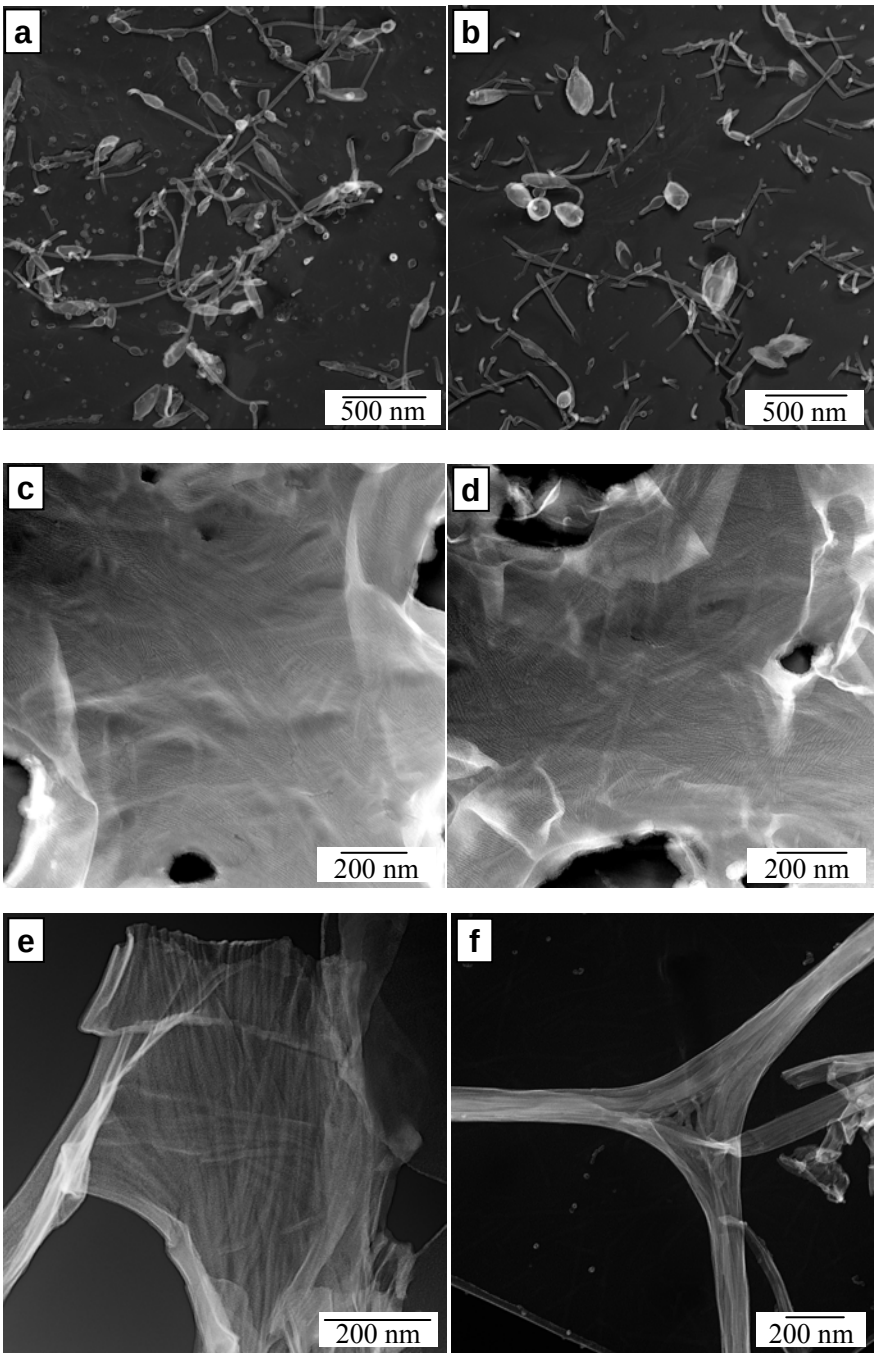

Figure 34 | QFDE-TEM micrographs showing the transition of assembled structures with temperature; **a-b,** At 25°C freshly dissolved PA solution contains small tube or vesicle-like structures. **c-d,** At 80°C structures seen at 25°C disappear and form large sheet-like structures. **e-f,** After cooling back to 25°C, nanofibers forms locally aligned fiber bundles. (Images courtesy of Megan Greenfield)

2.7.6 Small Angle X-Ray Scattering

SAXS measurements were performed using beam line 5ID-D, in the DuPont-Northwestern-Dow Collaborative Access Team (DND-CAT) Synchrotron Research Center at the Advanced Photon Source, Argonne National Laboratory. An energy of 15 keV corresponding to a wavelength λ=0.83 A^{-1} was selected using a double-crystal monochromator. The data were collected using a CCD detector (MAR) positioned 245 cm behind the sample. The scattering intensity was recorded in the interval $0.00025 < q < 0.25$ A^{-1}. The wave vector defined as, $q = (4 \pi / \lambda) \sin(2\theta / 2)$, where 2θ is the scattering angle. Samples were placed in 1.5 mm quartz capillaries. The exposure times were between 2 and 4 seconds. For the temperature controlled measurements samples were sealed within 1.5 mm glass capillaries that were placed in a Lincoln THMS thermo stage. See Figure 35 for the equipment setup. The samples (1 wt% $C_{15}H_{31}$CO- VVVAAAEEE(COOH), dissolved in water with pH adjusted to 7.0 by NaOH) were heated at a rate of 10 °C/min and held for 1 h at 80C before cooling at a rate of 1 °C/min. The 2-D SAXS images were azimuthally averaged to produce one-dimensional profiles of intensity, *I*, *vs.* *q*, using the two-dimensional data reduction program FIT2D. The scattering of capillary and solvent (water) were also collected subtracted from the corresponding solution data. No attempt was made to convert the data to an absolute scale.

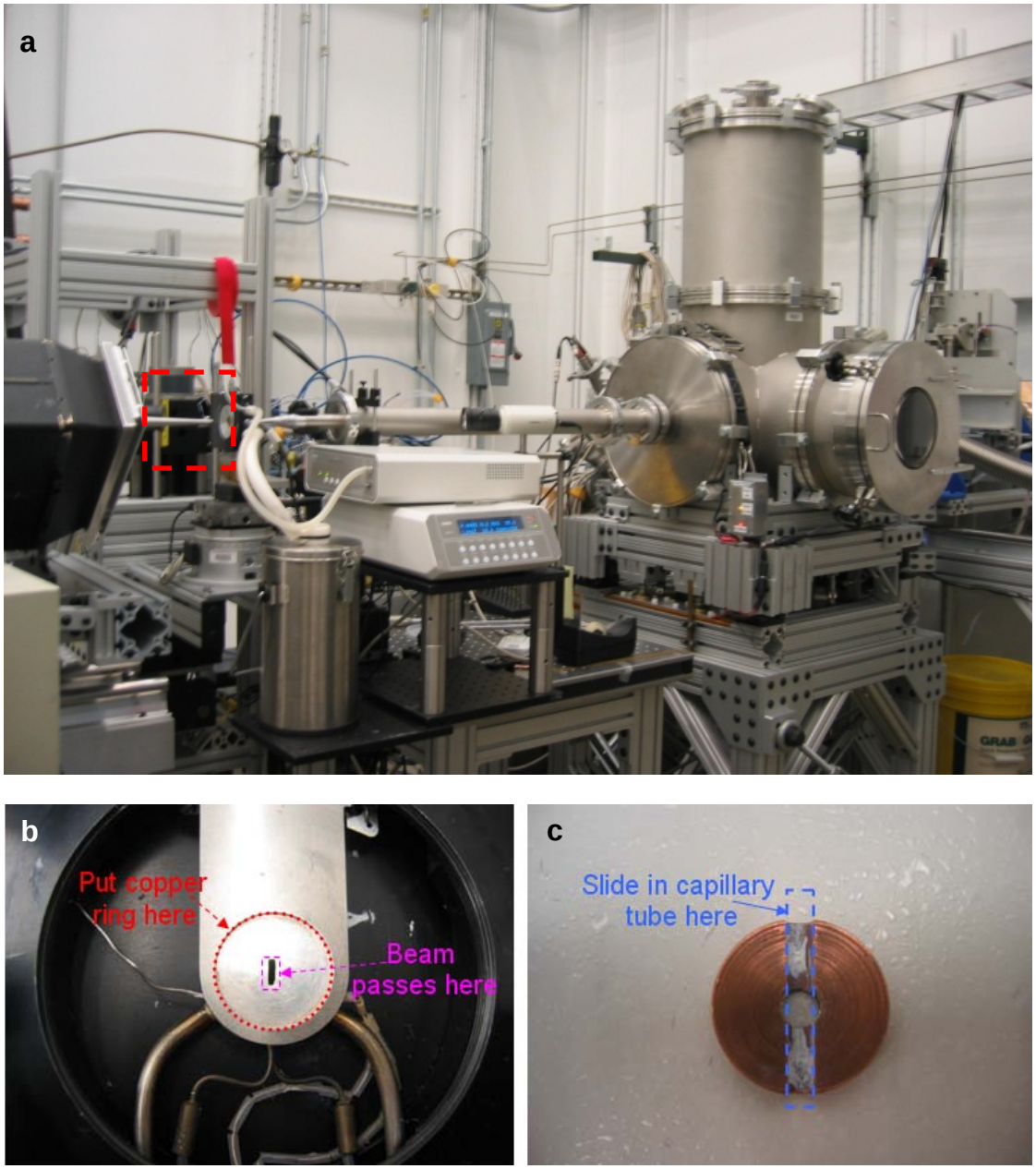

Figure 35 | SAXS equipment setup; **a,** setup of SAXS at Argonne National Lab; Red box is the sample holder position; **b-c,** a cutaway view of capillary heating control unit and capillary holder.

2.7.7 CD Spectroscopy

CD was used to study how elevated temperature affects the secondary structure of peptide amphiphiles. The CD signal was recorded (J-715 CD spectrometer, JASCO Inc., Easton, MD) during heating from 25°C to 80°C and then during cooling from 80°C to 25°C (Figure 36). Experiment used 1 mm quartz cell and 0.1 mg/ml freshly dissolved PA in distilled water. System was kept at each temperature (listed in figures) for 5 minutes before scanning. A strong beta sheet signature was seen over the entire temperature range covered. The CD signal of freshly dissolved filler PA solution slightly decreased as temperature increased from room temperature to 80°C but changed little during cooling from 80°C to 25°C, consistent to what has been reported before.

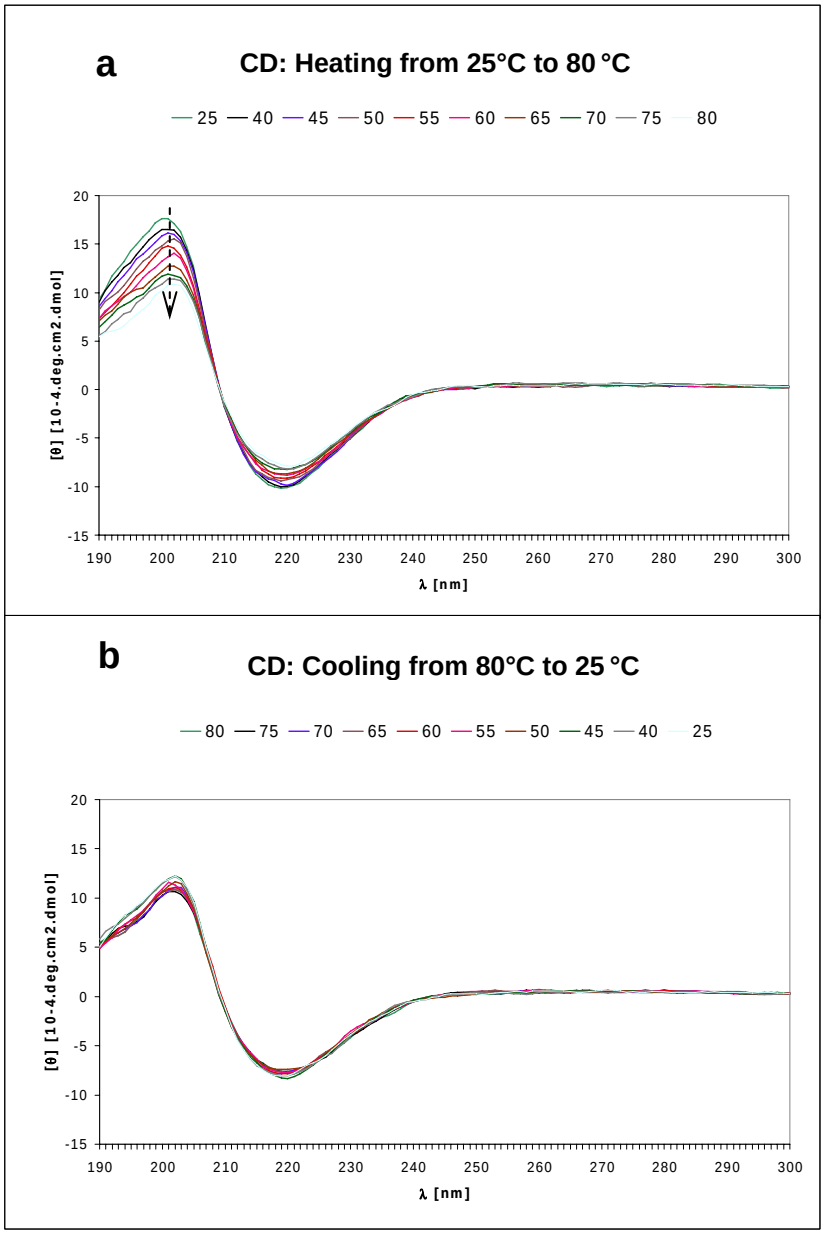

Figure 36 | CD scans from freshly prepared 0.01 wt% PA ($C_{15}H_{31}CO$-VVVAAAEEE (COOH)) solution at different temperatures during heating up and cooling down cycle. **a,** Scan while heating up. **b,** Scan while cooling down. (Figures courtesy of Dr. Conrado Aparicio)

2.7.8 Real Time RT-PCR

hMSCs were cultured in aligned and isotropic environments for two weeks in hMSC osteogenic, chondrogenic, or regular growth medium (Cambrex, Walkersville, MD). After culturing, RNA was isolated and reverse transcripted into cDNA with TRIZOL® Reagent and SuperScript® III First-Strand Synthesis System from Invitrogen. Real-time PCR was done with Bio-Rad iQ5 Real-Time PCR system and Promega's Plexor® qPCR System. Several lineage specific marker genes and housekeeping genes were picked for real-time RT-PCR (*Alkaline Phosphatase,(ALP), Osteopontin (OPN), Aggrecan (AGC1),Collagen II Alpha I (COL2A1), Desmin (DES), Alpha Smooth Muscle Actin (ACTA2) and Glyceraldehyde 3-phosphate dehydrogenase (GAPDH)*). Primer pair sequences are listed in Table 4.

CHAPTER THREE

Aligned PA Matrix and Its Application in Biology

Chapter 3: Aligned PA Matrix and Its Application in Biology

3.1 Introduction

Controlled cellular orientation and outgrowth is commonly seen in natural tissues and is closely related to tissue function. For example, in arteries, smooth muscle cells (SMCs) and collagen fibrils are circumferentially oriented to provide mechanical support [122, 123]. In the adult myocardium, cardiomyocytes elongate and orient in parallel to form a syncytium, which enables propagation of electrical signals [124]. Enamel, which provides superb mechanical properties to teeth, is formed by highly aligned ameloblasts producing hydroxyapatite crystals in an ordered manner [125]. The successful formation of neural circuits *in vitro* and nerve regeneration *in vivo* also depends on guiding neuronal growth cones along specific pathways to help them find correct targets [126]. Reproducing these ‘‘*in-vivo*-like’’ orientation and organization of the cells in an engineering system therefore is a very intriguing and challenging subject.

The established ‘‘contact guidance’’ theory illustrates that in many cases, cells or cell processes have bidirectional responses to anisotropic chemical, structural and mechanical properties of the substratum [118, 127]. Based on this observation, researchers have successfully used techniques such as electro-spinning [113, 114], laser nanotopography [128], micro-contact printing [129-131], microfabrication and mircromachining [132-135] to create patterned surfaces and demonstrated the capability to orient cells on two-dimensional (2-D) substrates (Figure 37).

Unfortunately, techniques that can be used to align cells in three-dimensional (3-D) environment are limited, within which dynamic culture conditions [136] and gradient chemotropic guidance [137] were the most explored. More recently, researchers also developed photolabile hydrogels, and used light to guide cell growth [138]. These methods, however, are difficult to be used as they are in tissue regeneration. A more general and simpler method is still preferred.

In the current study, we introduce a novel hydrogel material and processing method to create a synthetic extracellular matrix, which can be used to control cellular orientation and outgrowth in both 2-D and 3-D environments. With the materials and methods described, preferentially oriented hydrogel matrixes have been rapidly prepared over centimeter scale. Birefringence and scanning electron microscopy (SEM) observations revealed that these macroscopically oriented matrixes are composed of a highly aligned nanofiber array. Since it is anticipated that the aligned fiber matrix could provide physical guidance over cellular orientation and outgrowth, we encapsulated three different types of cells in this matrix and studied their behavior. As a result, we found these cells preferentially aligned and outgrew along the long axis of the nanofiber.

The hydrogel materials under discussion were self-assembled from surfactant peptide molecules [81] with epitopes that are known to be bioactive [139, 140]. We can customize the matrix composition by coassembling PA molecules bearing different signaling sequences. At the same time, matrix mechanical properties can be adjusted by changing hydrogel concentrations. With this flexibility, we believe these functional ECM analogues have great potential in many biomedical systems.

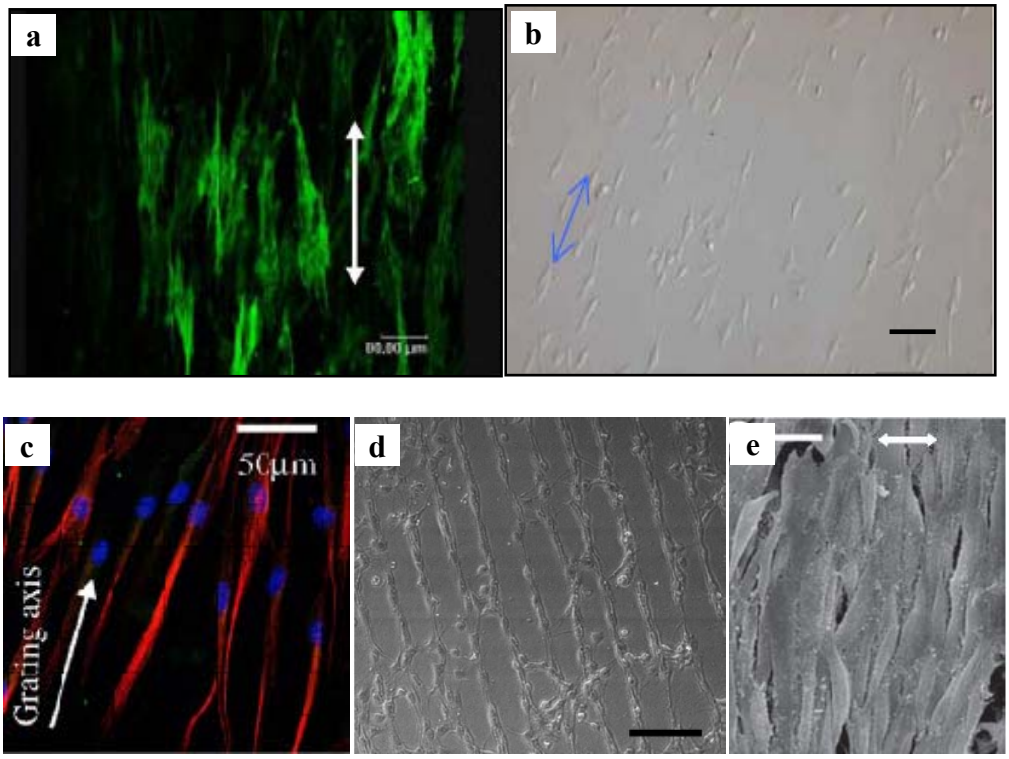

Figure 37 | Examples of preferential cell alignment on 2-D substrates. **a,** SMCs aligned on nanofibrous scaffold prepared with electrospinning. **b,** C6 glioma cell aligned on laser processed nanogrooves. **c,** Myoblast aligned on cell culture substrates with microscale topography. **d,** Schwann cells aligned on PMMA patterned with laminin µCP. **e,** Muscle cells cultured under cyclic strain aligned perpendicular to stress direction. (Reproduced from [113, 114, 128, 130, 131, 133-137])

3.2 Materials and Methods

3.2.1 Chemicals

Amino acids and derivatized resins were purchased from NovaBiochem (EMD Biosciences, CA, USA). All chemicals were purchased from Fisher or Sigma-Aldrich and used as provided. All water used was deionized with a Millipore Milli-Q water purifier operating at a resistance of 18.2 MΩ.

3.2.2 Cells and Reagents

Human mesenchymal stem cells (Poietics™ hMSCs), human bladder smooth muscle cells (Clonetics™ bSMCs) and their growth media were purchased from Lonza Walkersville, Inc., MD, USA. hMSCs used in the experiments were at passage 6-9 and bSMCs used were at passage 7-8. DRG cells were obtained by digesting freshly acquired DRG tissue from CD-1 mice at postnatal day 1. The DRG were treated with 0.25% trypsin for 30 min at 37°C and then mechanically dissociated by trituration. The DRG cells were cultured in DMEM/F-12 with 10% FBS, 1% pen/strep, 25 ng/ml nerve growth factor (NGF) and 20 μ mol Cytosine β-D-arabinofuranoside (Ara–C) (Sigma-Aldrich), an anti-proliferative agent to remove all non-neuronal cells.

3.2.3 Fabricating Preferentially Aligned PA Matrix

Materials used in this study are prepared using PA molecules (Figure 38) and their mixtures. They were dissolved in either pure water or phosphate-buffered saline (PBS) at concentrations of 0.5 wt% to 1.5 wt%. A vortexer was used to help dissolve samples. The solutions were then heated to 80 °C, held at that temperature for about 30 minutes, and slowly cooled down to room temperature. Dip-coating (vertically immerse and drain) with the resulting solution, we can create long-range alignment of PA nanofibers on surfaces. Pipetting and dragging this solution in 20 mM $CaCl_2$ solution (Figure 39 and Figure 50) results in a noodle-like gel composed of highly aligned nanofibers. The materials (henceforth called "PA noodle") were rinsed and collected with water or culture media for further studies.

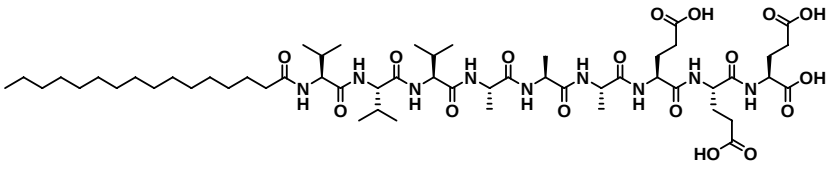

(a)

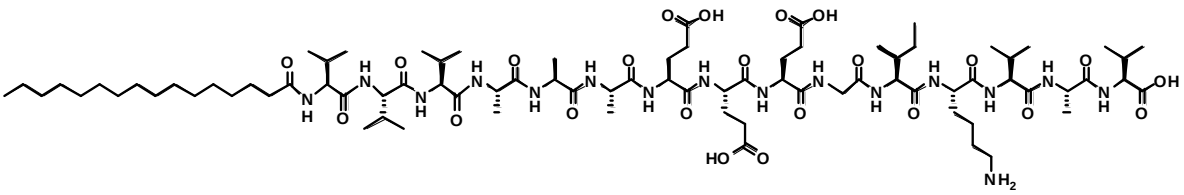

(b)

Figure 38 | Peptide amphiphile molecules used in this chapter;
a, PA1: $C_{15}H_{31}CO$- VVVAAAEEE(COOH); **b,** PA2: $C_{15}H_{31}CO$-VVVAAAEEEGIKVAV(COOH)

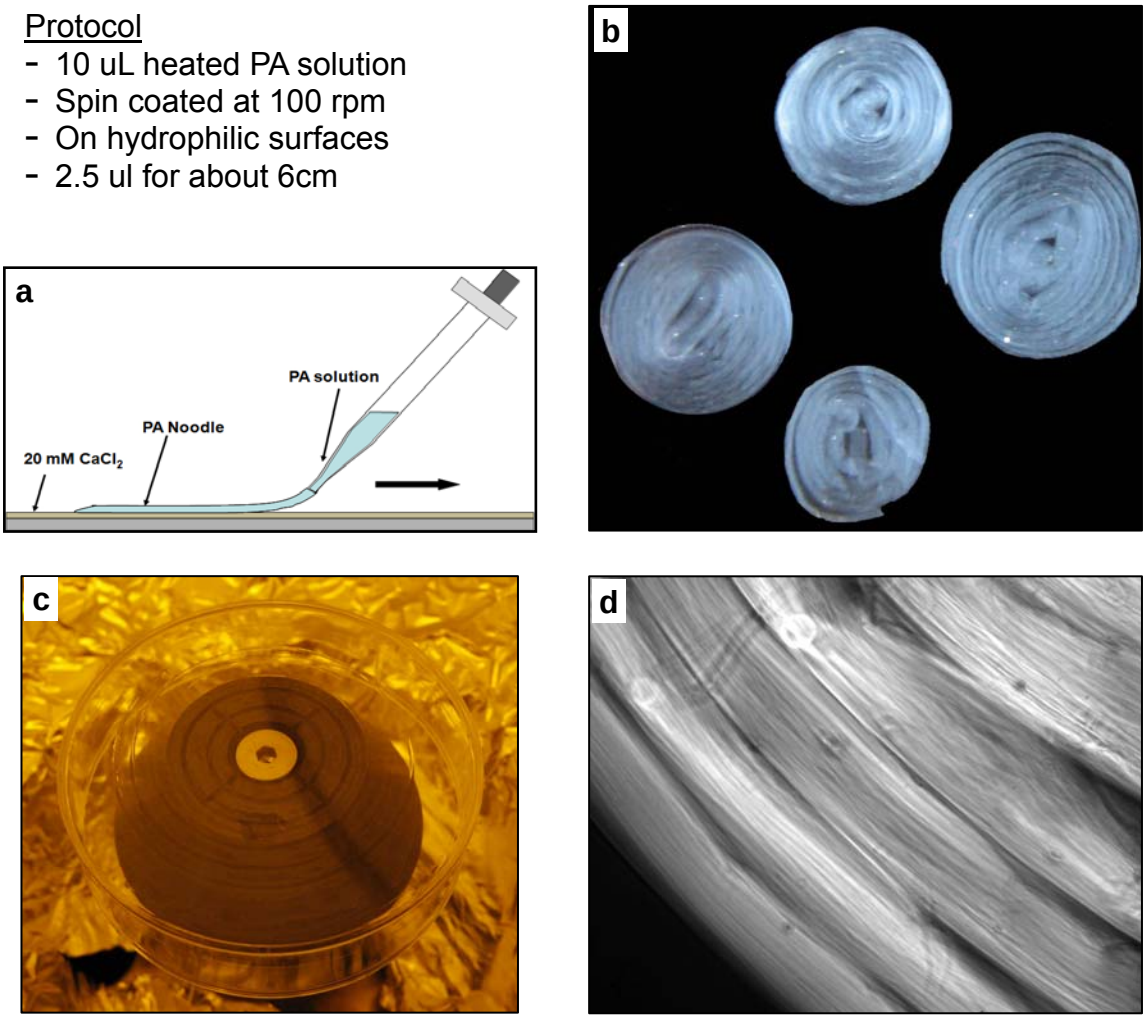

Figure 39 | **a,** Heated and cooled peptide amphiphile solution is dragged and gelled into PA noodle on glass substrate soaked with gelling reagent. **b,c** PA noodle can be rolled into a spiral shape by depositing on a rotating spinner. **d,** Preferentially aligned PA noodle under crossed polars.

3.2.4 Controlling Cellular Orientation with PA Noodle

Tissue culture flasks with 80-90% confluent hMSCs or bSMCs were treated by 0.5% Tripsin/EDTA. After cells detached from the flask, their number was counted with a hemocytometer. For PA coated 2-D surfaces, cells were randomly seeded on top. To encapsulate them inside the PA noodle, the suspension of cells was centrifuged into a pellet. A heated and cooled PA solution was then used to re-suspend the cells pellet at a density of 1000-5000 cells/µl. The concentration of PA solution is 0.75-1.0 wt% for hMSCs and 0.5 wt% for bSMCs and DRG cells. After the cells were encapsulated in the PA noodle, they were cultured in corresponding media and incubated at 37 °C. Culture media were changed every 3 or 4 days.

3.2.5 Cell Morphology Studies

3.2.5.1. Optical Light Microscopy

Polarized light microscopy, phase-contrast light microscopy and fluorescent light microscopy were all performed with Nikon, Eclipse TE2000U. These techniques were used to study the alignment of PA nanofibers as well as the interactions and alignment of cells with surrounding scaffold. In fluorescent light microscopy study, live hMSCs and bSMCs cells were labeled with Calcein Am (Invitrogen Corp., CA, USA) for better visualization. The labeling was done by submerging a PA noodle in 5 mM Calcein Am solution for 30 min at 37 °C.

3.2.5.2. Scanning Electronic Microscopy

SEM was employed to study the morphology of cells grown in the PA noodle. Samples

with encapsulated cells were fixed in 1X phosphate buffer containing 2% glutaraldehyde (Electron Microscopy Sciences, PA, USA) and 3% sucrose at 4°C and pH 7.4. After fixation, the samples were dehydrated using a gradient of 10% to 100% ethanol and critical point dried with Polaron critical point dryer (Model 3100). These samples were sputter-coated with a 3-nm coating of Au/Pd and imaged with a Hitachi S-4800-II SEM.

3.3 Results

3.3.1 Fiber Orientation

SEM micrographs of 1 wt% PA noodle shown in Figure 40 revealed that the PA noodle comprises nanofiber bundles with diameters around ~30 nm. These bundles orient along the longitudinal axis of PA noodle and form a nanofibrous scaffold. As polarized light microscopy can distinguish between isotropic and anisotropic materials or material domains with different refraction indexes, it offers a simple method to study the alignment of nanofibers in PA noodle (Figure 41). The uniform brightness in Figure 41 indicates that the high level of nanofiber alignment observed by SEM exists throughout the whole PA noodle sample.

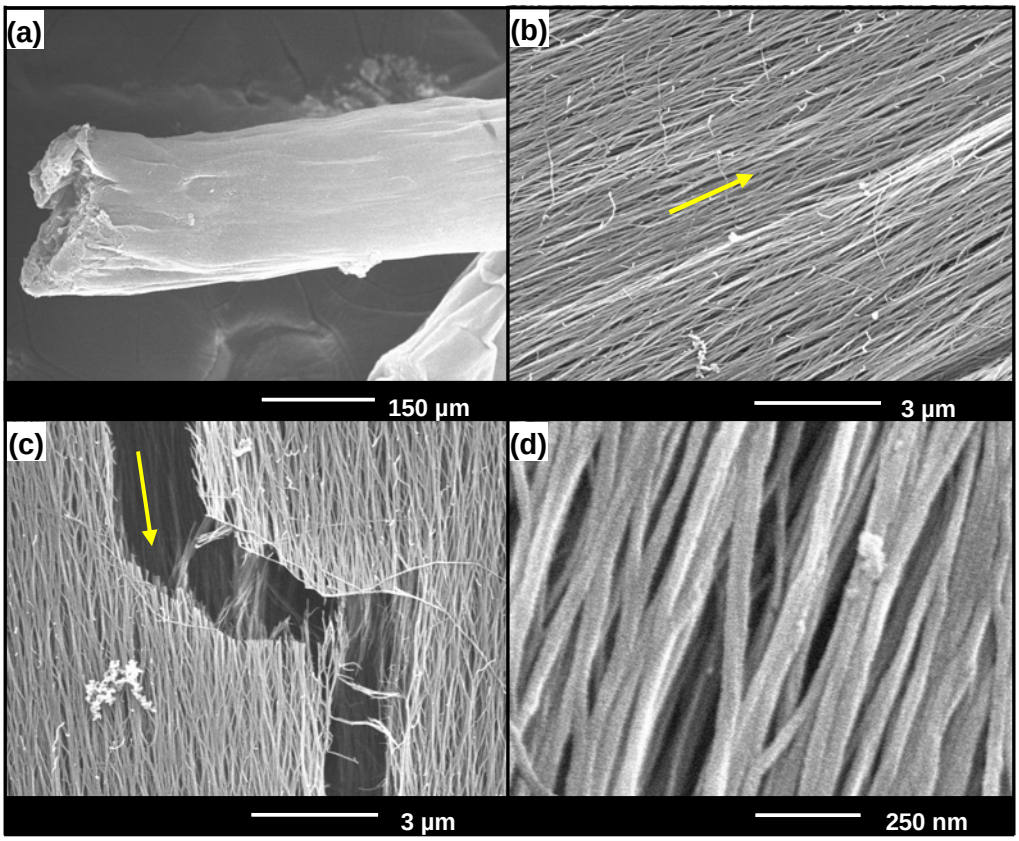

Figure 40 | SEM micrographs of aligned PA noodle; **a**, overall image of an oriented PA noodle, **b**, zoom in images of a, arrow indicates nanofibers orientation, **c,** inside the crack (indicated by arrow), nanofibers alignment is just as good as on the surface, **d,** nanofibers are perfectly aligned to the nanometer scale (Image courtesy of Dr. Alvaro Mata).

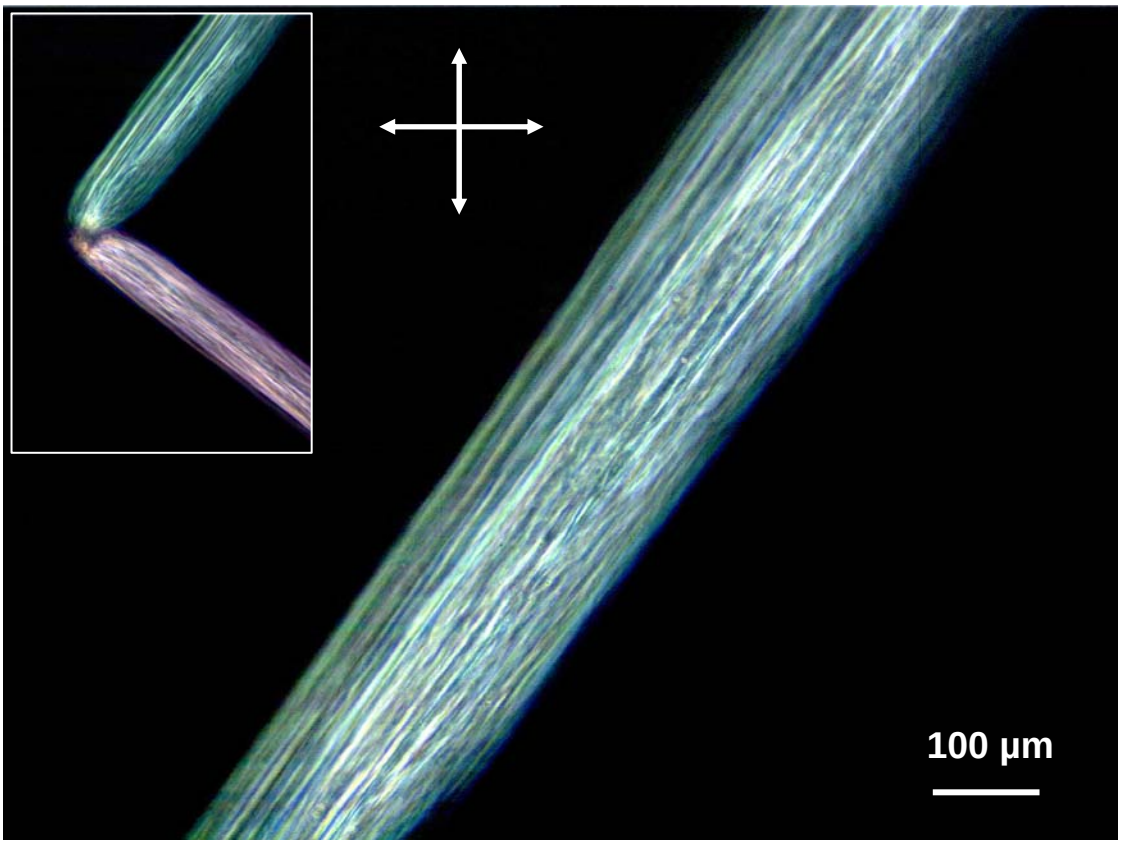

Figure 41 | PA noodle observed with crossed polars (indicated by arrows) shows uniform birefringence proves overall alignment of nanofibers inside PA noodle. Inset: one noodle bends at 90 degree.

3.3.2 Cellular Orientation

Our cellular experiment results show that the highly oriented PA noodle matrix effectively controlled the orientation and outgrowth of three different cell types (hMSCs, bSMCs and DRG cells), presenting a simple method to promote cell alignment on coated 2-D surfaces and in 3-D matrixes. As shown in Figure 42 and Figure 43, bSMCs cultured on top of coated glass maintained bipolar spindle shapes and oriented in the same directions as nanofibers in substrate coating. In contrast, bSMCs grew in random directions on bare glass. More interestingly, encapsulated hMSCs extended and preferentially aligned in 0.75 wt% PA noodle after 3 days of incubation (Figure 44 a-b). As cells were distributed in a truly 3-D environment, many fluorescents cells in these figures were out of focus plane. Since seeding density can play a pivotal role in a variety of cell dynamics [141], we seeded bSMCs at density of 1000 and 5000 cells/μl in 0.5 wt% PA gel (Figure 44 c-d). The cellular alignment of bSMCs is similar to that of hMSCs. And the PA noodle system is capable of getting cells aligned at high cellular density. In blood vessel engineering, such alignment of SMCs is crucial since natural vessels are composed of axially aligned SMCs in regions of vortex blood flow [142].

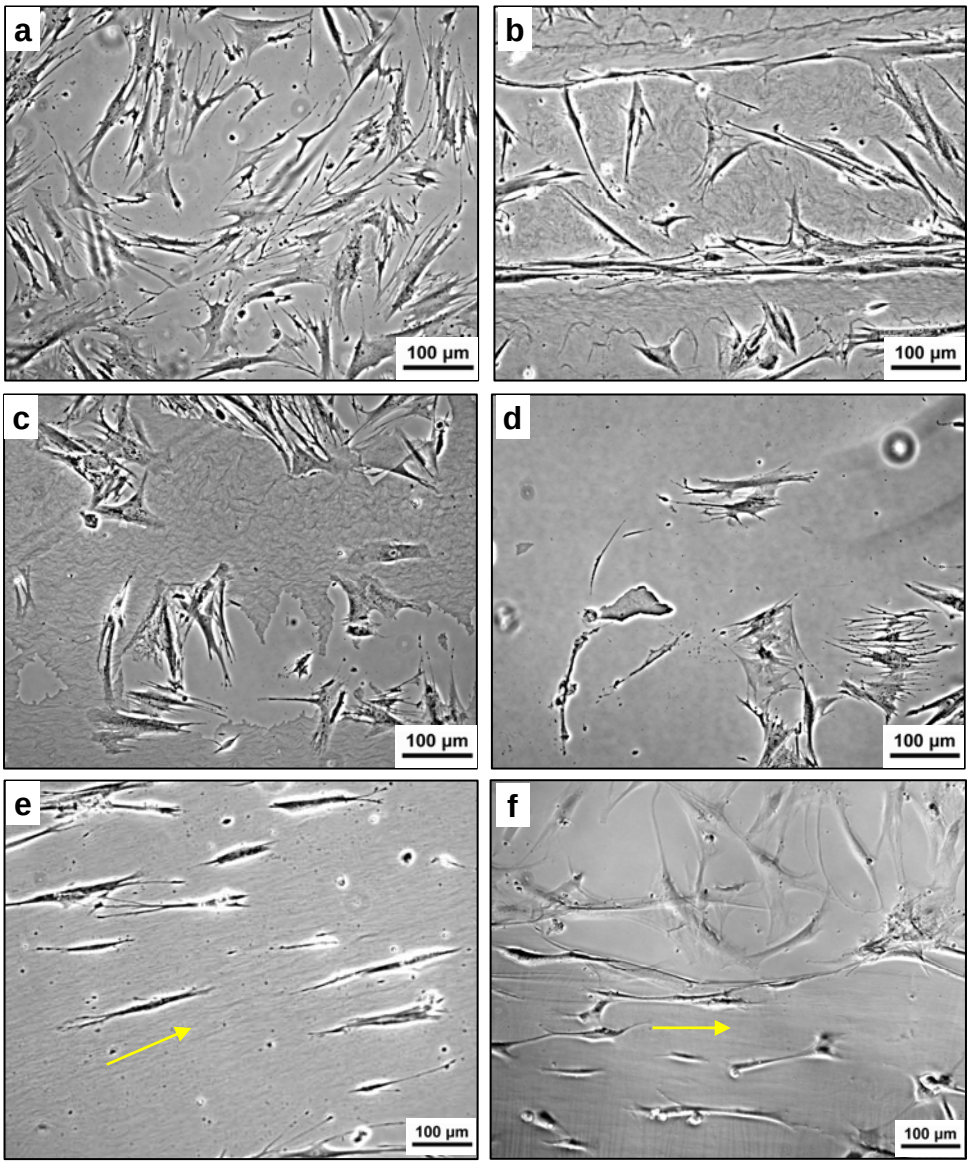

Figure 42 | SMCs on glass with different PA coating. **a,** SMC on glass grow in random directions. **b,** SMC grow in random directions on heated filler PA coating without proper alignment. **c, d,** Non-heated PA coating came off glass substrate after 48 hours, cells also grow in random orientations. **e,** bSMCs grew on coated glass maintained a bipolar shape and oriented in the same direction as substrate nanofibers. **f,** bSMCs grew in random directions on bare glass (upper half), but in parallel on coating (bottom half). Arrows indicate surface nanofiber orientation.

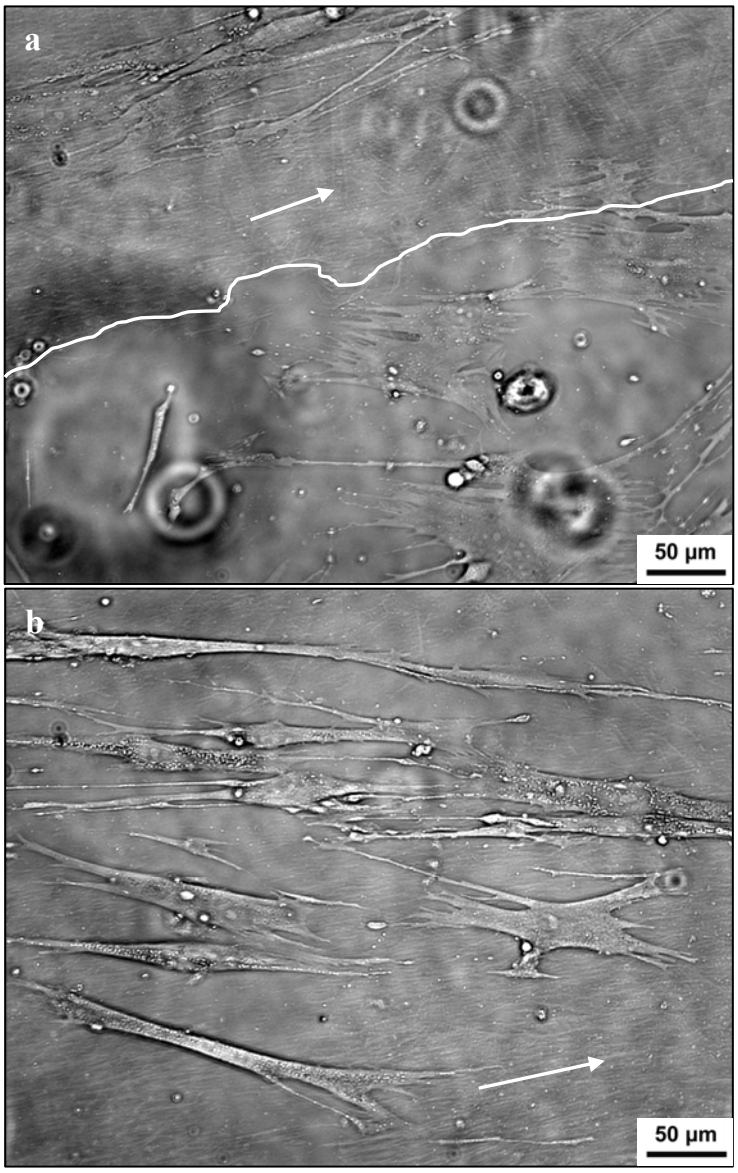

Figure 43 | SMCs preferentially aligned to substrate coating direction (indicated by arrows). **a,** Cells on the coated region grow in one direction, whereas growth of nearby cells on glass are random. **b,** Another field of observation, texture of underneath PA coating can be seen clearly.

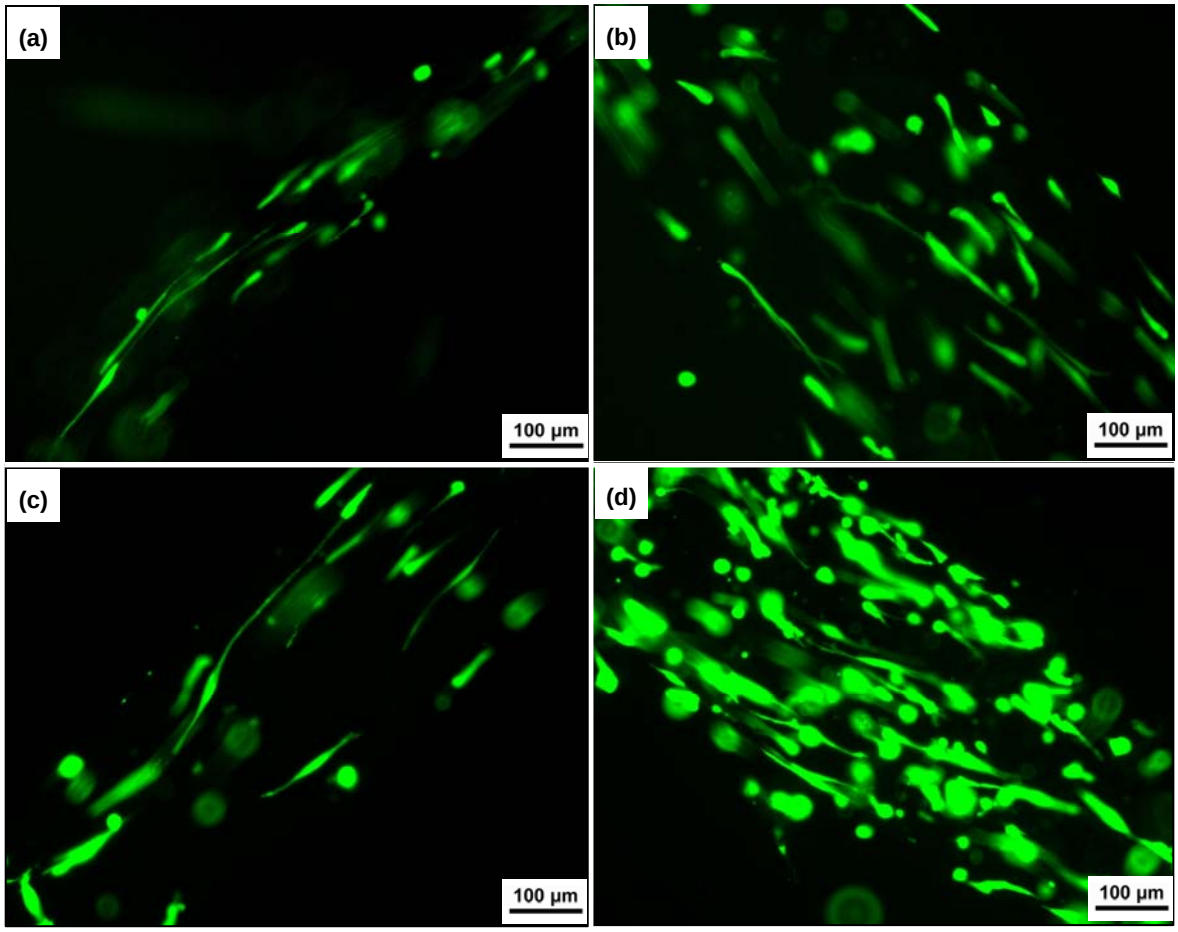

Figure 44 | Optical micrographs of hMSCs and bSMCs cultured in PA noodle; **a,b,** hMSCs seeded in 0.75 wt% PA noodle at 1000 cells/µl densities; **c,d**, bSMCs seeded in 0.5 wt% PA noodle at 1000 cells/µl and 5000 cells/µl densities. Both cell types were labeled with Calcein Am after 3 days culture to help visualization.

We also investigated cells' behavior when cultured for longer period of time. As in Figure 45, the PA noodle (0.75 wt%, 1000 hMSC/μl) remained birefringent and the encapsulated cells remained aligned after one month incubation. At the same time, the cell density increased significantly, which means they were actively proliferating inside PA noodle during the one month culturing time. Representative SEM micrographs of cells (hMSCs) cultured in a PA noodle are shown at different magnifications in Figure 46. The cell body had an apparent bipolar elongated morphology, which follows the same direction of PA nanofibers. Cell filopodia are partly embedded and tightly grabbing to the fibers. It is difficult to visualize how the completely encapsulated cells interact with their surrounding matrix using SEM. However, it is clear that cells are interacting with PA and their orientation has a close relation with the surrounding nanofibers.

Encouraged by these results, we explored the opportunities to neurons. Earlier work of Silva et al [143] has demonstrated that nanofibers presenting high density IKVAK epitope cause more selective differentiation of neural progenitor cells to neurons. Therefore, we adjusted the gel composition for DRG cells by adding 10% of PA2, which contained the IKVAV epitope (Figure 38 b). The mixture of PA molecules was then treated as described above. Freshly retrieved DRG cells were disassociated and then suspended in the PA noodle at a density of 5000 cells/μl. Since DRG cells are much smaller than hMSCs and bSMCs, we expected this system to accommodate an even higher cell density. Phase-contrast light microscopy showed that, after 3 days, neurites of DRG cells are mostly aligned along the PA nanofiber direction (Figure 47) and

the preferential orientation can be observed on different focal planes. Since freshly retrieved DRG contains many glial cells, which may proliferate, we added Ara-C media to suppress their growth and to only allow neuron cells to grow in these materials [144]. Many factors, such as Ca^{2+} concentration, gel stiffness and time of tripsin/EDTA treatment, influence the viability of neuron cells in PA noodle. We are still optimizing these parameters. However, the effect of controlling neuron cells' orientation is obvious under all of the conditions tested.

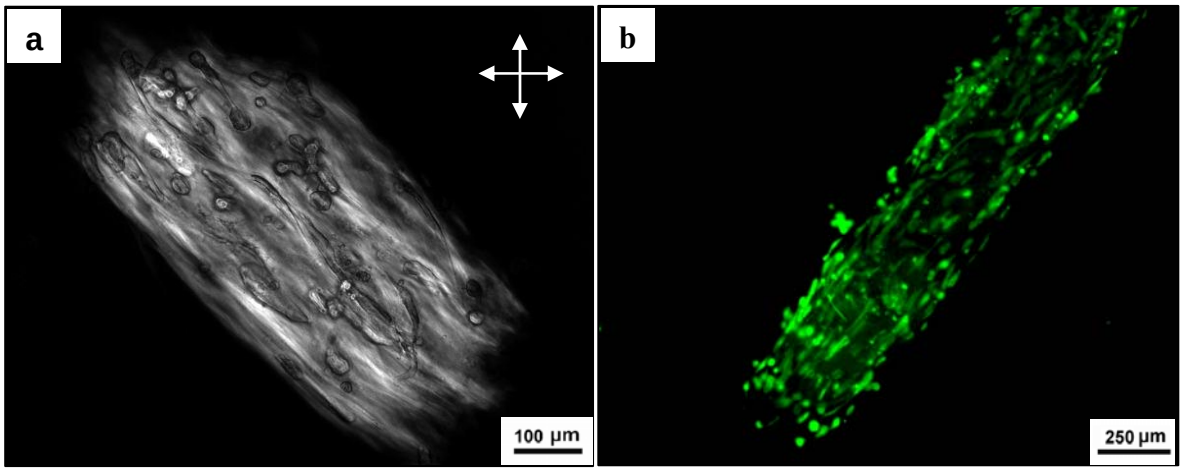

Figure 45 | After one month incubation in media, **a,** PA noodle originally having 1000 hMSCs/µl remained birefringent when observed with crossed polarizers. **b,** hMSCs encapsulated inside this PA noodle also remained aligned with the PA noodle axis. At the same time, cell density increased significantly (compare to Figure 44). Cells were labeled with Calcein Am to help visualization.

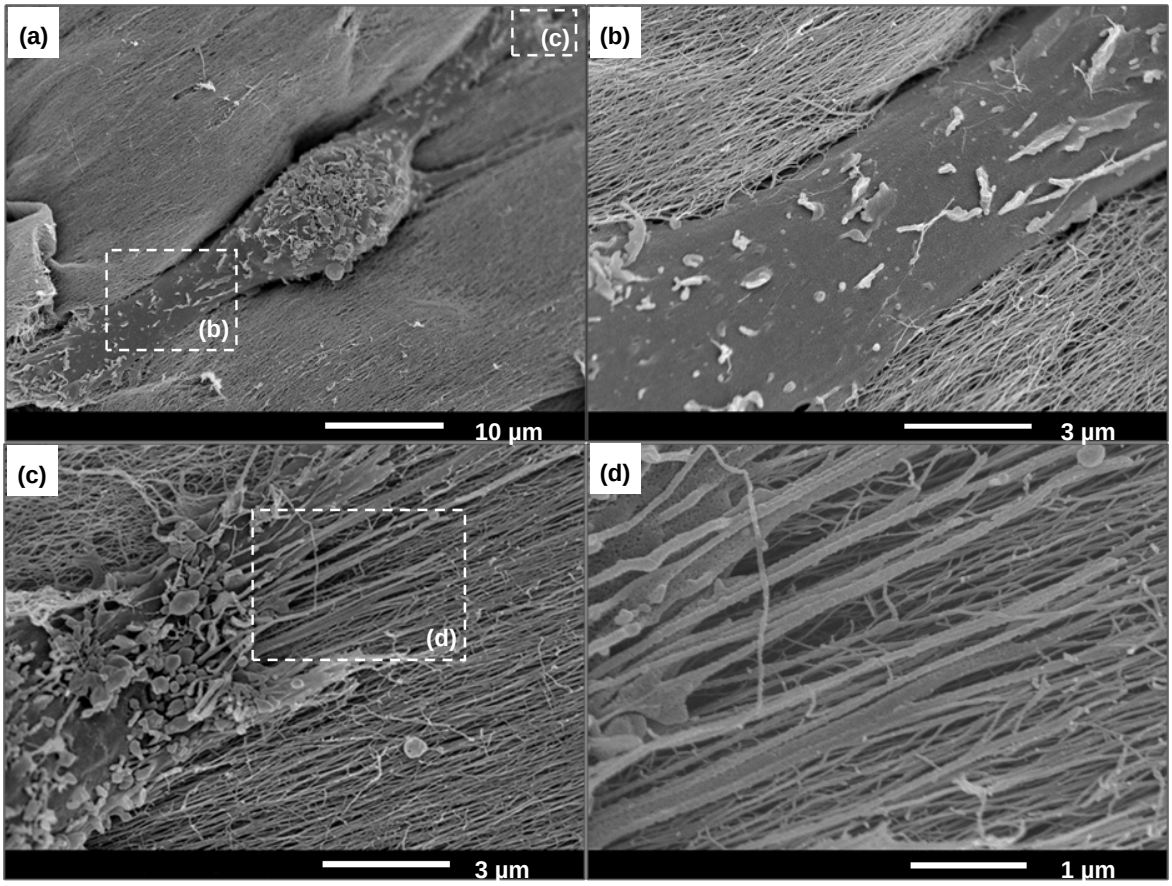

Figure 46 | SEM micrographs showing hMSCs aligned with oriented peptide amphiphile matrix; **a**, hMSCs interacting with oriented PA matrix; **b-d**, zoom in images of white box regions. Both cell body and filopodia are aligned with nearby nanofibers (Images courtesy of Dr. Alvaro Mata).

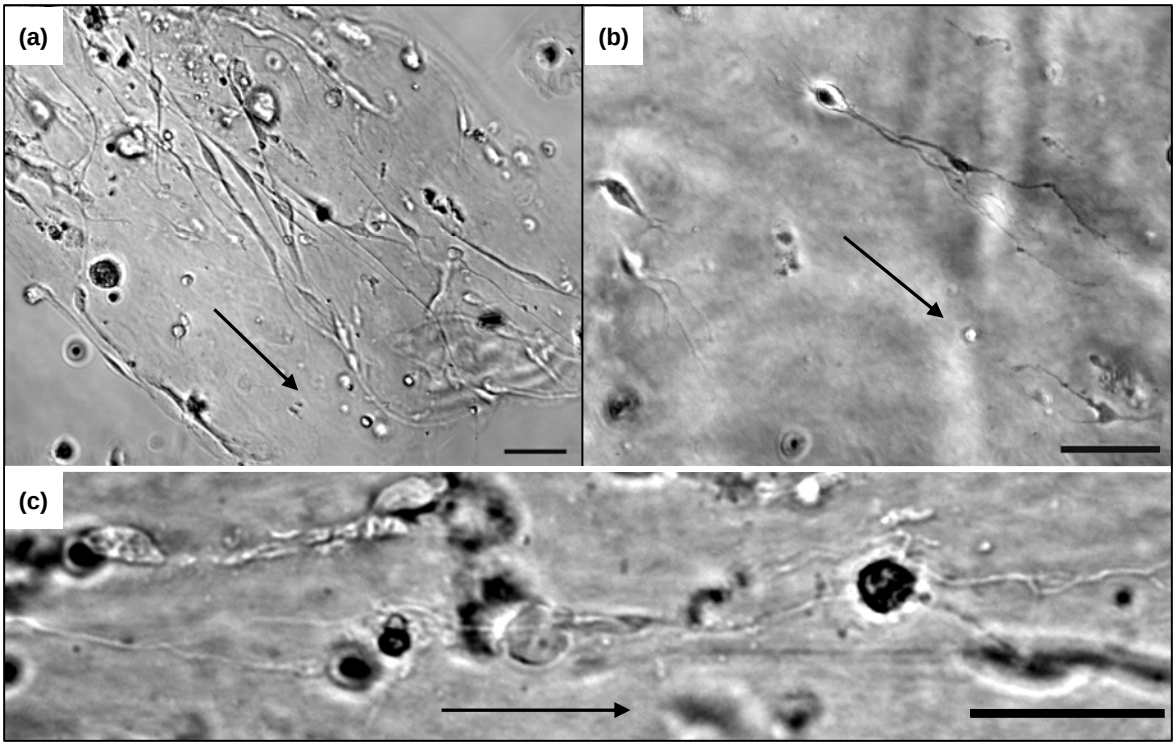

Figure 47 | Optical micrographs of DRG cells encapsulated in PA noodle after 3 days, arrows indicate PA noodle axis, which is also the matrix nanofibers orientation [scale bar= 50 μm].

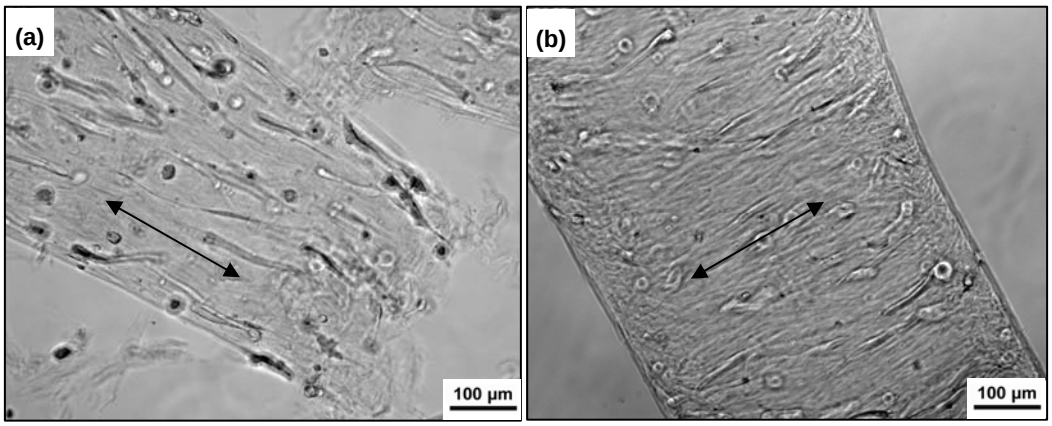

Figure 48 | Optical micrographs showing preferential cellular orientations are different in PA noodles formed by dragging or extruding process. **a,** In the dragging process, elongation flow aligned nanofibers along PA noodle axis; encapsulated hMSCs therefore aligned parallel to this direction. **b,** In extrusion process, shear flow aligned nanofibers perpendicular to PA noodle axis; encapsulated hMSCs therefore aligned perpendicular to PA noodle axis.

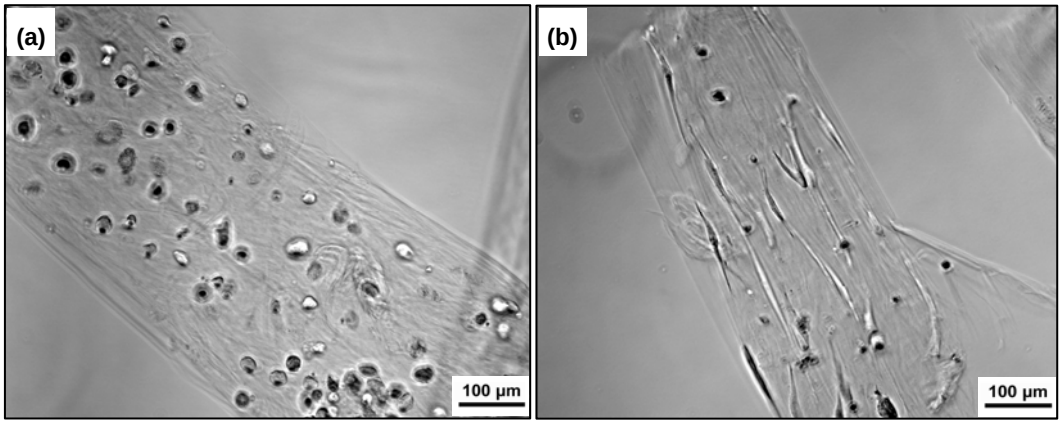

Figure 49 | Optical micrographs showing PA concentration changes morphologies of encapsulated cells. **a,** In 1.5 wt% PA noodle, encapsulated hMSCs stay rounded morphology after 3 days of culturing. **b,** However, in 0.75 wt% PA noodles, they exhibit bipolar spindle shape after the same culturing time.

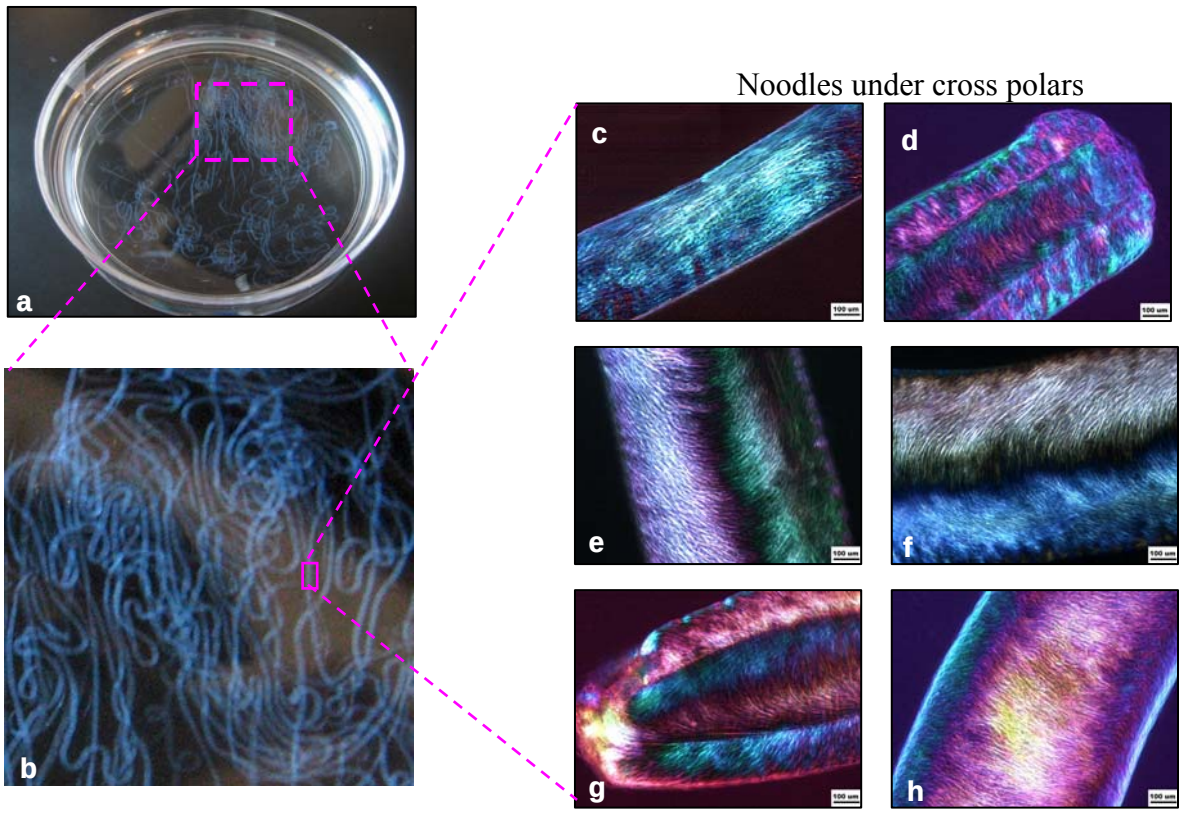

Figure 50 | The orientation of nanofibers inside a noodle is dependent on the method of extrusion. **a,b,** Noodle-like gel formed by injecting heat treated PA solution in salty media. **c-h** Higher magnification view of PA noodle in b. Birefringence in these images clearly indicates that alignment of nanofibers is dependent on extruding parameters. Extensional flow is required to achieve alignement seen in **c**.

3.4 Discussion

The most distinct characteristic of the PA noodle is the high level alignment of the nanofibers, which subsequently leads to preferential cellular orientation and outgrowth. To manipulate this orientation factor in device fabrication, we need to control the shear forces applied to nanofibers during gelling process. As shown in Figure 48, two cells containing PA noodles were made by dragging (a) and extruding (b) the same PA/Cells mixture in Ca^{2+} gelling reagent. Although the composition is the same, cellular orientations in these two PA noodles were apparently different (in Figure 48 a, cells grew in parallel to the PA noodle axis while in Figure 48 b they grew in perpendicular). This result indicates that the nanofibers are orientated differently with elongation flow (dragging) and shear flow (extruding) (see Figure 50) [145]. Cellular orientation is a consequence of nanofiber orientation. On this basis, we can employ this method to create ordered cellular structures in a controllable fashion.

It is already known that optimal matrix stiffness is not the same for all cell types. In the case of hMSCs, the matrix stiffness alone can have profound effects in cell fate [120]. With the PA noodle system, we can easily adjust optimal mechanical properties for each cell type by simply changing the concentration. For example, we found hMSCs cultured in 1.5 wt% PA noodle maintain a rounded morphology (Figure 49 a). However, when the concentration is decreased to 0.75 wt%, hMSCs are mostly bipolar spindle shape (Figure 49 b), which indicates a contractile phenotype. Our results also showed bSMCs and DRG cells spread out faster in gel of 0.5 wt% or less.

We can also adjust the chemical composition of the PA noodle by adding signaling or cytokine-binding molecules. As an example, in the experiment with DRG cells, we mixed PA 1 with the complementary PA 2 bearing the epitope IKVAV, which is believed to be beneficial for neuron cells. Addition of such signaling molecules does not seem to bring any significant change to fiber alignment or overall mechanical properties. PA molecules that promote cell adhesion [146], accelerate biomineralization [81, 147], bind to bone morphogenetic protein (BMP) [148], have also been synthesized. Introducing these derivatives into PA noodle provides us great possibilities of customizing chemical compositions for individual cell type.

There are many approaches that can translate our findings into improved methods of tissue engineering. As a simple example, they can be used to create desired surface patterns that guide cellular orientation and outgrowth, a simple route for fabricating patterned *in vitro* neuron networks. More interesting applications include aligning neuron cells in PA noodle to form a "neuron wire" that can transmit signals between biological and/or artificial devices, fabricating multi-layer ECM analogs with different cellular orientations and compositions and templating oriented biomineralization etc.

3.5 Summary

In this chapter, we proved that PA noodle can be used to control cellular orientation and outgrowth. Due to the simplicity of preparation and outstanding biological performance, such materials have great potential for tissue engineering applications.

CHAPTER FOUR

Creation of Robust PA Noodles

Chapter 4: Creation of Robust PA Noodles

4.1 Introduction

Peptide amphiphile (PA) materials are known to self-assemble into nanofibers and form biocompatible hydrogel scaffolds [81, 82]. In previous chapters, we have shown that, by heating PA solution to an elevated temperature and cool back to room temperature, a nematic liquid crystalline phase could be formed from an isotropic solution. Furthermore, we demonstrated that by dragging the solution in a salty medium this LC phase could be fixed into a macroscopic hydrogel string of aligned nanofibers (also called PA noodle) [149]. PA matrices with such a high degree of orientation could have great potential to control preferential cellular orientation and outgrowth in building neuron wires, muscle strings etc [150]. One of the remaining practical challenges in using this material is the mechanical properties of PA noodles. Specifically, the noodle structures are sometimes brittle and difficult to manipulate, limiting their applications in tissue regeneration and engineering devices.

To address these problems, we have explored the underlying role of intermolecular forces on the macroscopic mechanical properties of PA hydrogel and have applied our insights to develop a more robust PA noodle. We first studied the mechanical properties of the PA gels by oscillatory rheometry and focused on how the material responded to a wide range of strains. From these experiments we found hydrogel with higher Tanδ value is generally more robust. Also known as dumping factor, Tanδ is the ratio of the loss modulus (G”) to the storage modulus

(G') and indicates to the fluidity of a gel. We then demonstrated that the increase of Tanδ value in the PA hydrogel can be achieved via various means, such as lowering the solvent pH or by using lower valency of ions for gelation. Alternatively, we can also optimize molecular design for the same purpose. With these new developments, we improved the mechanical properties of the PA noodle and boosted its potential for in field applications. The same principle and testing methods may be helpful for others who study hydrogel systems.

4.2 Materials and Methods

4.2.1 Rheological Test

Oscillatory rheological strain sweeps were conducted over PA gel with allowed strain ranges gradually increase (from 0.1, 0.5, 1, 2, 5, 20, 50, to 100 percent). Tanδ (shown in each figures) value was acquired in the linear viscoelastic region of first round oscillatory strain sweep test. Rheological data were collected with a Modular Compact Rheometer 300 (Paar Physica, Germany) operating in 25 mm parallel-plate configuration. All samples had a total volume of 300 μL. Once the gels were formed, the top plate was lowered onto samples to a gap distance of 0.5 mm. Mineral oil was dropped around the edge of the plate and wet tissues were placed at the perimeter of a chamber around the gel to minimize evaporation. Stage temperature was maintained at 25°C by a Peltier heating system. Samples were allowed to equilibrate one hour before testing. G′ and Tanδ value were averaged over a minimum of two trials.

4.2.2 CD

In this chapter, CD was used to study how the increase of pH value in PA solution affects the β-sheet formation during PA self-assembly. All tests were performed with 2mm quartz cell and J-715 CD spectrometer (JASCO Inc., Easton, MD, USA). PA concentration used was 0.1mM. Data was shown earlier in Chapter II.

4.2.3 SAXS

SAXS experiment was performed over 2 wt% PA noodle (PA6 in Table 3) using Rigaku S-MAX 3000 High Brilliance SAXS System in J.B. Cohen X-Ray Diffraction Facility. PA noodle was soaked in water and sealed in a 1.5 mm quartz thin-walled capillary tube (Charles Supper Company, MA, USA) by resin. 2D scattering pattern was acquired by 18 hours of scattering in vacuum with water background subtracted.

4.2.4 PA noodle Fluoresce Staining

For better visualization, PA noodle in Figure 54 was labeled with 0.03 wt% of pyrenebutyric acid (PBA). To disperse PBA evenly, PBA was first dissolved in tetrahydrofuran (THF) at 1.0 wt%, and then dilute it 50 times in 1.0 wt% PA H_2O solution. Heat the mixture at 80°C to anneal the solution and remove THF (THF's boiling temperature is 66 °C). Photo was then taken in dark room under UV.

4.2.5 Cell Culture and Staining

Cells used in this study are Poietics™ hMSCs (passage 6) from Lonza Walkersville, Inc., MD, USA. Related reagents are from the same company. Cells were encapsulated in PA solution at a density of 2000 cells/μl. Growth media was changed every 3-4 days during culture. Calcein AM was used to label live cells encapsulated in PA noodle after 48 hours in culture.

4.3 Result and Discussion

The mechanical properties of PA nanofiber gels are influenced by a several parameters, including the stiffness and strength of individual nanofibers, the degree of fiber bundling, and the density of crosslinks between nanofiber bundles. Factors that can lead to changes in these aspects are therefore our tools for adjusting hydrogel mechanical properties.

In Figure 51 A the same 10mM PA water solution were separately gelled with 10X PBS and 25mM $CaCl_2$. Mechanical properties of these gels were investigated by oscillatory rheometry. Specifically, gels were exposed to a series of strain sweeps, with each subsequent test achieving a higher maximum strain. The breakdown of each PA gel was also assessed by determining the strain sweep after which the gel start to lose its initial G' and unable to recover under low strain. The purpose was to compare how valencies of gelling ions affect the hydrogel properties. Ions concentrations were chosen based on an empirical observation known as the Schulze–Hardy rule, which states that the critical coagulation concentration (CCC) scales with the inverse sixth power of the counterion valence, i.e., $CCC \propto 1/z^6$ [103]. According to this rule, 10X PBS, which

contains about 1600 mM mono-valent ions is close to 25 mM Ca^{2+} ($1600/2^6$) in terms of its gellation capability. The stress-strain curve (G' vs. γ) showed gel in Figure 51 A (short for "gel A") has much lower G' and higher Tanδ (G' ~200 Pa, Tanδ ~0.25) than gel in Figure 51 B (short for "gel B", G' ~10,000 Pa, Tanδ ~0.14). However, the seemingly "weak" gel A was more robust than gel B and could tolerate large deformation without breaking. In contrast, gel B had a higher G' value, but it breaks down quickly with increasing strains. Reflected in G'/ γ curves, the multiple runs of strain sweeps in gel A showed greater overlapping profile than those of gel B. The observed difference can be explained by how the divalent and monovalent ions interact with the molecules. Specifically, the divalent Ca^{2+} ions support inter- and intra- fiber ionic bridging, which locks fibers in place and results in stiff but more brittle networks. The monovalent ions, on the other hand, can only screen the electrostatic repulsion between the molecules and fibers. With no strong interaction exists, such network is not as stiff, and can smoothly adjust to external deformation by viscous sliding among fibers. These results suggest that, at least within the examined regime, the robustness of a gel is correlated to its fluidity, as represented by Tanδ. Increasing Tanδ value in hydrogels can potentially solve our previous brittleness problems.

To increase Tanδ value, our strategy is to decrease crosslink density among fibers by pH adjustment and addition of monovalent ions before calcium crosslinking. For future applications using cells, we limited the pH range between 6.0 and 7.5 and used monovalent ion concentration at 0 or 160 mM NaCl (close to 1X PBS). All of the PA molecules used in this study contain multiple carboxyl groups. It is these groups that interact with divalent ions to make crosslinks.

Lowering the pH of the PA solutions leads to less deprotonation of the carboxyl groups and therefore reduces crosslink density among fibers. The pK_a values for the α-carboxyl group and side chain carboxyl group of glutamic acid are 2.1 and 4.1 [151]. With these pK_a values, most of the carboxyl groups should have been deprotonated at pH 6.0-7.5. However, as previously reported [99] supramolecular aggregates of peptide amphiphile show complex pH titration curves with transitions occurring over wide ranges, implying the change of apparent pK_a values of the carboxyl groups in the assembled state. On the other hand, adding monovalent ions before calcium crosslinking results in more carboxyl groups associated with monovalent ions and further reduces crosslinks made by divalent ions. Neither of these two methods makes a significant change on its own (Figure 51 C and Figure 52 A). However, the synergy of them effectively increased Tanδ, leading to overlapping strain sweep profile (Figure 52 B-C) and good mechanical properties for handling.

Since we have shown that increasing gel fluidity (larger Tanδ) significantly improves the PA gel's performance, we decided to investigate whether the same effect could be achieved through changes in molecular design, which has been shown to be a powerful tool for tailoring hydrogel properties [83, 108]. To test our hypothesis we synthesized several PA molecules of three designs (Figure 53, Table 3). These designs are similar in structures, but the locations of carboxyl groups in the molecules are varied so that after PA molecules assemble into nanofibers, deprotonated carboxyl groups available for interfiber ionic bridging would be presented on the fiber surface (design A), close to fiber surface (design B) or buried inside the fiber (design C).

We hypothesized that this modification would directly change the amount of potential interfiber ionic bridging during gelation, thereby resulting in a change in the gel's macroscopic properties. Like many other PA molecules used in our lab, these designs all contain a hydrophobic tail, a β-sheet forming peptide segment, and a charged peptide segment. During the self-assembly process, the hydrophobic tails collapse and hydrogen bonds form between adjacent β-sheet forming peptide segments. At the same time, the charged peptide segments repel one another and inhibit the assembly and aggregation process. All of the designed PA molecules self-assemble into high-aspect-ratio cylinders that were indistinguishable from $C_{15}H_{31}CO$-VVVAAAEEE(COOH), the PA used in Figure 51 and Figure 52. Similar oscillatory rheological studies were performed with each of these PA gels. The results summarized in Table 3 again showed that lower pH values correspond to higher Tanδ and better conservation of mechanical strength. It is not surprising to see little difference between design A and B, because their close resemblance. Interestingly, a significant increase in Tanδ was observed in design C, which agrees with our hypothesis that a network with decreased interfiber bridging will have increased fluidity. We also noticed a drop in G', which is probably caused by the inaccessibility of carboxyl groups for interfiber crosslinking.

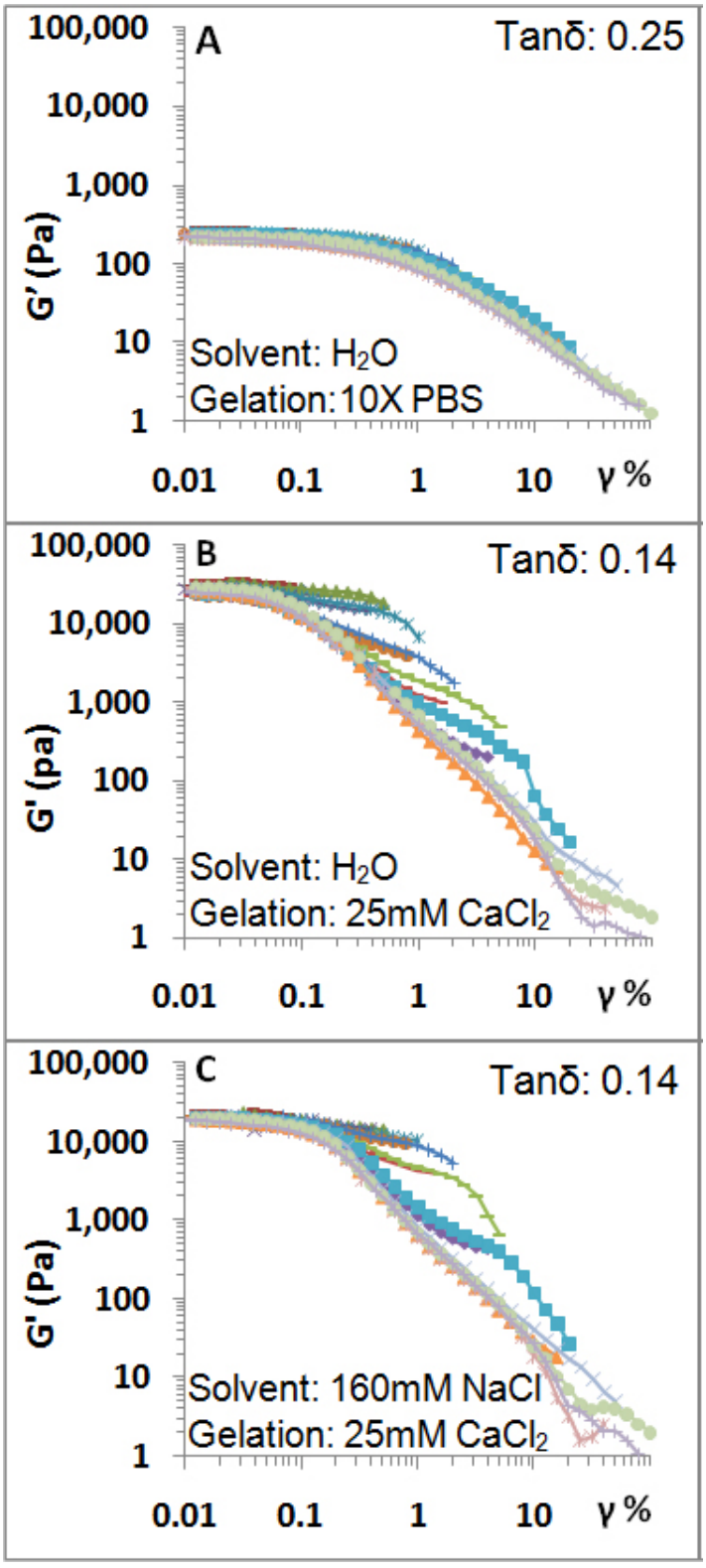

Figure 51 | Different solvents and gelation conditions make the same molecule ($C_{15}H_{31}CO$-VVVAAAEEE(COOH)) form different materials. Solvent used were H_2O or 160mM NaCl. Solutions' pH value were adjusted to 7.5 before heat treatment. Gelation conditions used were 10X PBS or 25mM $CaCl_2$ as labeled in the graph. Results show that valency of gelation ions can significantly change G' and Tanδ value. Within tested range, higher Tanδ value corresponds to increased resistance to deformation and an overlapping profile of sequential runs of strain sweep.

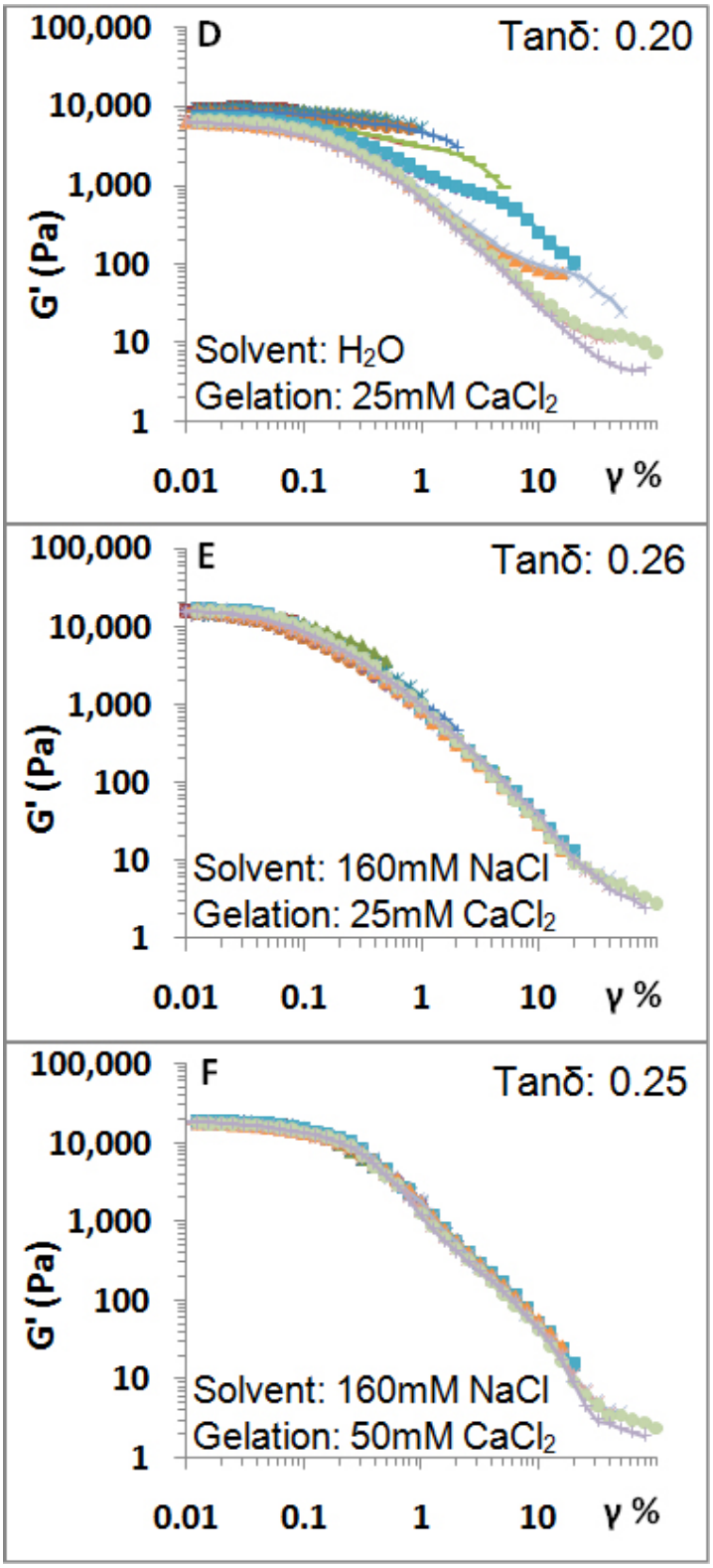

Figure 52 | Continuation of Figure 51. Solvent used were H_2O or 160mM NaCl. Solutions' pH values were adjusted to 6.0 before heat treatment. Gelation conditions were 25mM $CaCl_2$ or 50mM $CaCl_2$ as labeled in the graph. Results show that decreasing solution pH value can also help increase Tanδ value. The synergy of monovalent ions in solution and reduce solution pH value can significantly increase Tanδ values and lead to overlapping profile of sequential runs of strain sweep.

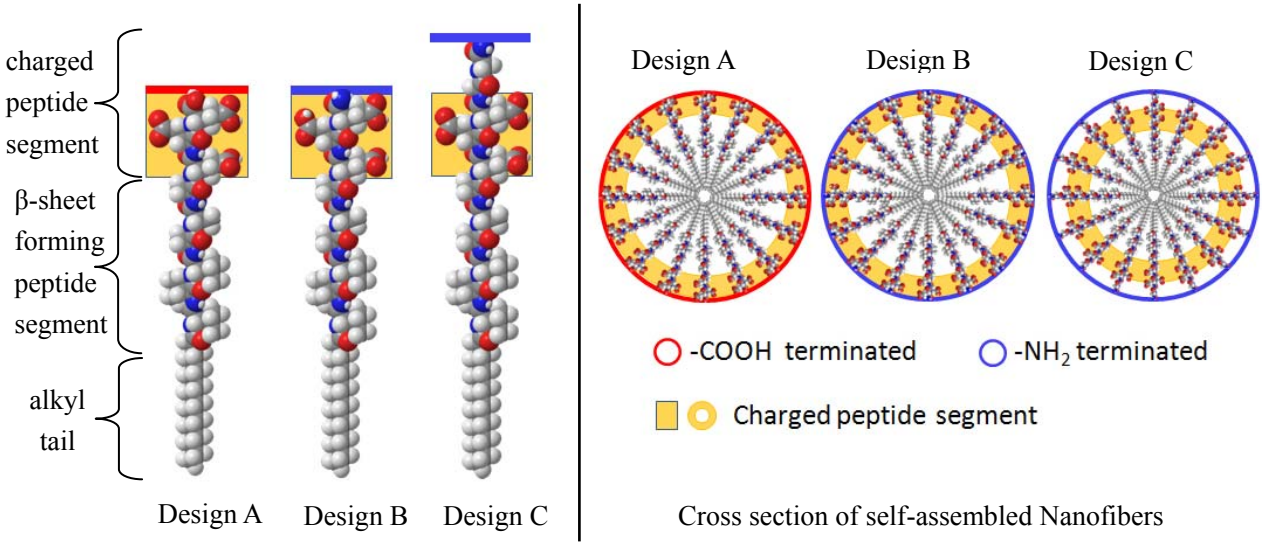

Figure 53 | Illustration of three PA molecular designs: A, B and C that after assembly form nanofibers differ in their capabilities for interfiber ionic bridging. The designs listed on the left all contain a hydrophobic alkyl tail, β sheet forming peptide segment and a charged peptide segment. However, the locations of carboxyl groups are varied. After assembly, they form fibers with cross sections illustrated on the right. As the charged peptide segment is gradually moved deeper inside the fibers, the chance of interfiber ionic bridging is reduced.

Table 3 | Oscillatory Strain Sweeps Study of Bulk PA Hydrogel

PA #	Structures	-COOH	Design	Low pH*			High pH#		
				G' (kPa)	Tanδ	G'/γ overlap	G' (kPa)	Tanδ	G'/γ overlap
1	$C_{15}H_{31}CO$-VVVAAAEEE(COOH)	4	A	17.5±2.8	0.26±0.02	Good	20.2±0.7	0.14±0.02	Poor
2	$C_{15}H_{31}CO$ -VVVAAAEEE(NH_2)	3	B	20.4±0.2	0.24±0.02	Good	19.5±2.2	0.15±0.00	Poor
3	$C_{15}H_{31}CO$ -VVAAEE(COOH)	3	A	19.8±5.7	0.15±0.01	Poor	97.6±7.6	0.08±0.00	Poor
4	$C_{15}H_{31}CO$ -VVAAEE(NH_2)	2	B	Not Soluble			8.7±0.2	0.18±0.02	Medium
5	$C_{15}H_{31}CO$ -VVVAAAEE(NH_2)	2	B	Not Soluble			15.9±2.2	0.10±0.00	Poor
6	$C_{15}H_{31}CO$ -VVVAAAEEEGG(NH_2)	3	C	6.8±0.2	0.24±0.01	Good	5.2±0.6	0.30±0.01	Good

*All PA were dissolved in 160mM NaCl and gelled at 25mM final $CaCl_2$ concentration. Tests were done over multiple samples. *Low pH value corresponds to pH 6.0 for PA 1-5 and pH 6.5 for PA 6-7. #High pH value corresponds to pH 7.5 for all PAs except PA5, where pH 10.0 was used. pH 6.5 and 10.0 were used because of insolubility of PA molecules at lower values.*

Of course, removing carboxyl groups from PA molecules or lowering the pH value has more impact than reducing the amount of deprotonated carboxyl groups for crosslinking. These changes also reduce the electrostatic repulsion between molecules and have effects over self-assembly. Improved performance in hydrogel may be caused by the shift of completion between hydrophobic interaction, hydrogen bonding *vs.* electrostatic repulsion. Earlier in Figure 18, we showed a pH dependent CD study over three PA molecules containing two, three or four carboxyl groups in the charge peptide segment. The result tells us, for a given alkyl tail and β-sheet forming segment, PA molecules with less carboxyl groups preserve β-sheet better at higher pH value. The shift of competition did happen. However, comparing PA1-PA7 at the same pH, we can see the shift of competition does not account for all the changes we see in Table 3. For example, at both low and high pH PA1 and PA2 are very close in Tanδ. Therefore, how ionic bridging is controlled in the gel is still very important.

With the exploration in gelation media and molecular design, now we can control the mechanical properties of the PA noodle materials as desired. As shown in Figure 54, PA noodles with improved robustness are indistinguishable from previous “brittle” PA noodle in morphology through SEM and orientation order through SAXS. However, they are more flexible and easy to handle. As a testimony of their robustness, we could even make knots with these hydrogel strings. Preferential alignment of cells in such knots or strings is similar to those seen in Chapter 2 and 3.

4.4 Summary

In this chapter we used oscillatory rheometry to study the hydrogel's response to a wide range of strains and how they fail with deformation. We found increased fluidity can make a hydrogel more robust. In PA hydrogel system, such adjustment can be achieved by methods that control the potential interfiber ionic bridging. Changing the pH value, adding monovalent screening ions and modifying the molecular design all work for this purpose. With improved mechanical properties, PA noodle technology is more likely to be used in tissue regeneration and engineering devices.

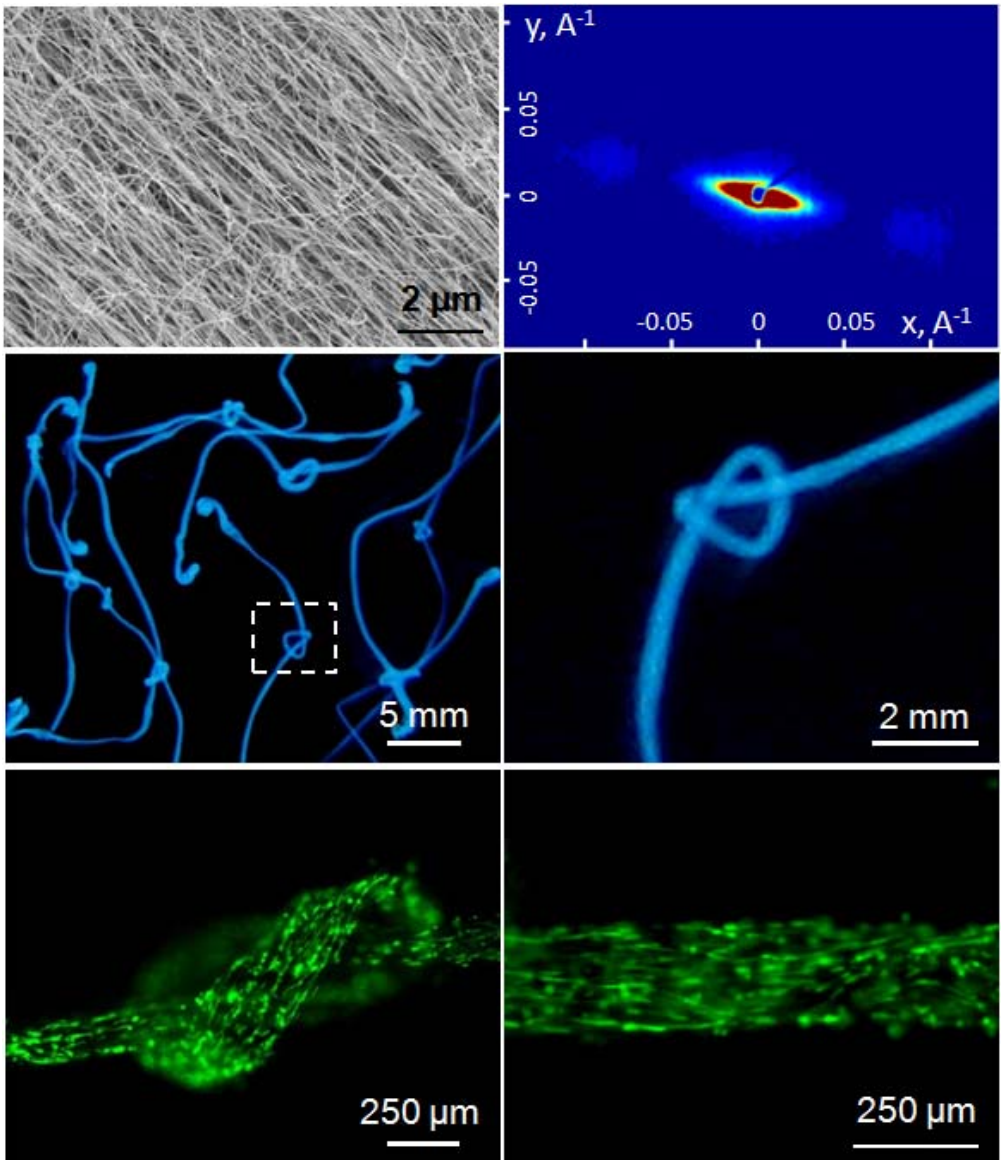

Figure 54 | Demonstration of PA noodle with improved mechanical properties. **a,** SEM micrographs showing increased hydrogel fluidity does not change the alignment of nanofibers in PA noodle. **b,** SAXS of PA noodle made with PA6 showed high degree of preferential alignment. **c-d,** With increased Tanδ value, PA noodles are much more robust. As a testimony knots were made with these hydrogel strings. For better visual effect, 0.02 wt% of pyrenebutyric acid (PBA) was mixed evenly into 1.0 wt% PA H_2O solution before heat treatment. Photo was taken under UV. **f-g,** Encapsulated hMSCs preferentially aligned in PA noodle after 48 hours culture. The knots and noodle are stable for long term culture.

CHAPTER FIVE

Parallel Assessment of Cells/Hydrogel Interaction by RT-PCR

Chapter 5: Parallel Assessment of Cells/Hydrogel Interaction by RT-PCR

5.1 Introduction

It is well known that extracellular matrix (ECM) can influence the behavior of cells quite markedly through biochemical determinants, such as anchorage for growth factors or signaling molecules, as well as physical cues like topography and mechanical properties. Therefore, cells often change their behaviors once isolated from surrounding ECM and constrained to Petri dishes [152, 153]. To address this long standing obstacle of tissue engineering, researchers have created highly hydrated 3-D hydrogels with structure and composition designed to carry appropriate chemical, biological, and physical cues [81, 154-156]. Such hydrogels provide cells desired cellular microenvironments and encourage the development of tissue-like structures *in vitro*. Further developments in arrays of these hydrogels that contain cells can be very useful for applications such as biosensing, drug screening or used to monitor cellular effects of multiple chemical and biological candidates [157-159]. However, as amplification methods (such as PCR) are usually not available for such array systems, quantitative study of the interaction of cells with their microenvironments is difficult. Also as the potential diversity of hydrogel composition could increase tremendously during a combinatorial study, systems for rapid synthesis and testing of material-cell interaction is severely needed.

In this research, we introduce a proof-of-concept methodology to rapidly prepare and analyze arrays of hydrogels that can contain varying concentrations and types of peptide

amphiphile (PA) solutions, growth factors, and cells (see Figure 55). Liquid handling robots Beckman Coulter "Biomek FX 96 Multichannel" and "Biomek FX Span-8" were used to facilitate this process. All of the components needed to grow cells within PA scaffolds (e.g. PA solutions, growth factors, media, gelling agents, etc) can be preloaded and dispensed at varying ratios and quantities in a 96-well plate to create an array of different culture conditions.

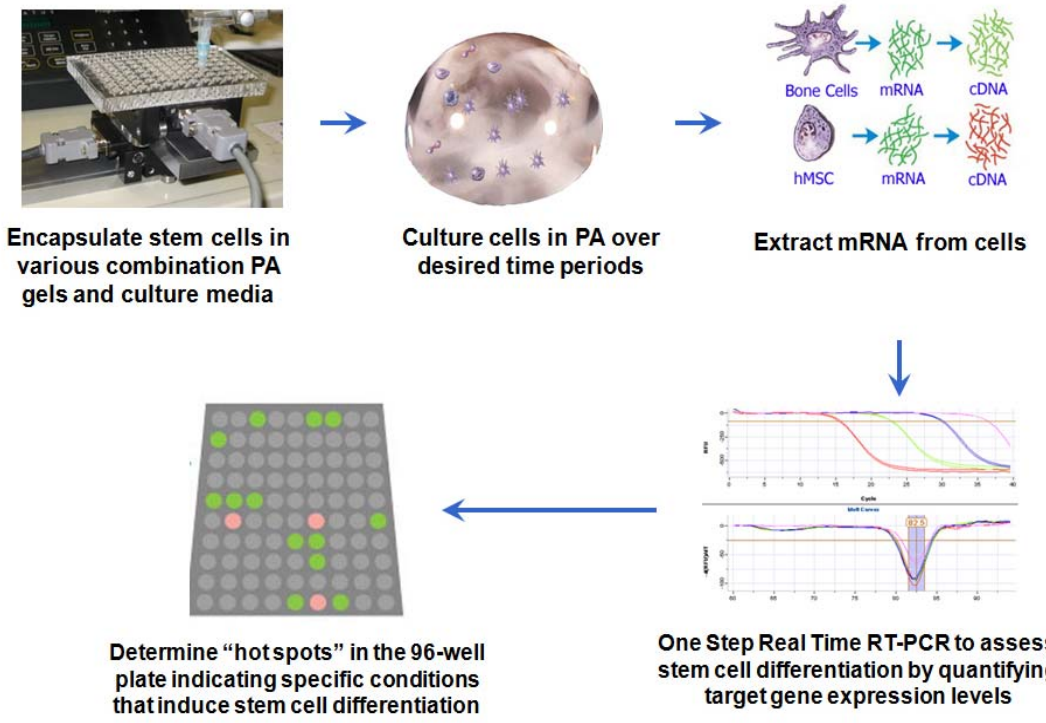

Figure 55 | Concept for arrayed Cell/Materials interactions

After culturing, cells were retrieved from hydrogel in parallel and used for real time RT-PCR study. This protocol provides a quick and economic method for high throughput assessing cell differentiation under various culture conditions and could enable significant expansion of experimental variables explored simultaneously.

5.2 Experiment Design

As a proof of concept experiment for the proposed methodology, a combinatorial scheme of 96 well hydrogel plates was created as shown in Figure 56. In this experiment plate, rows A to H are combinations of different PA molecules. The mixing ratios of different PA molecules in each row are listed in the right side box. Columns 1-2, 3-4, 5-6, 7-8, 9-10, and 11-12 have different growth factor concentration in the gels. Each gel has a total volume of 25 µl, 0.6% PA molecules and two repeats. After 14 days of culturing, plates were analyzed by RT-PCR.

	1	2	3	4	5	6	7	8	9	10	11	12		F : F-RGDS : F-BMP2 : F-S(P)
	0 ng/ml BMP		100 ng/ml BMP		400 ng/ml BMP		0 ng/ml BMP		100 ng/ml BMP		400 ng/ml BMP			
A	S01	S01	S09	S09	S17	S17	S25	S25	S33	S33	S41	S41	←	10 : 0 : 0 : 0
B	S02	S02	S10	S10	S18	S18	S26	S26	S34	S34	S42	S42	←	8 : 2 : 0 : 0
C	S03	S03	S11	S11	S19	S19	S27	S27	S35	S35	S43	S43	←	8 : 0 : 2 : 0
D	S04	S04	S12	S12	S20	S20	S28	S28	S36	S36	S44	S44	←	8 : 0 : 2 : 1
E	S05	S05	S13	S13	S21	S21	S29	S29	S37	S37	S45	S45	←	6 : 2 : 2 : 0
F	S06	S06	S14	S14	S22	S22	S30	S30	S38	S38	S46	S46	←	6 : 2 : 0 : 2
G	S07	S07	S15	S15	S23	S23	S31	S31	S39	S39	S47	S47	←	6 : 0 : 2 : 2
H	S08	S08	S16	S16	S24	S24	S32	S32	S40	S40	S48	S48	←	4 : 2 : 2 : 2
	Growth Media						Osteogenic Media							

Figure 56 | Combination scheme of proof of principle experiment

PA molecules used in this study include PA1 (F), PA2 (F-RGDS), PA3 (F-S(P)) and PA4 (F-BMP2) as listed in Figure 57. By mixing PA molecules that carry different epitopes, we tried to access many possibilities of combinations and test them for various applications. In previous chapters, PA1 has shown both satisfactory biocompatibility and mechanical properties. Therefore, it was used as “filler”, which provides the basic support and integrate other PA molecules together. PA2 contains the peptide sequence arginine-glycine-aspartic acid (RGD) sequence, a common ligand present on several ECM proteins [160, 161], for triggering cell adhesion. PA3

helps the bio-mineralization process[82]. PA4 helps to retain BMP2 growth factor in gel matrix by a BMP2 binding sequence [148]. These molecules were then mixed at various ratios and combined with cells, growth factors and culture media in a 96 well plate. The cells used in this study are mesenchymal stem cells (MSCs), which are bone marrow derived, self-renewing and multipotent progenitors.

After culturing for 6 and 14 days, plates were harvested and assessed by parallel real time RT-PCR assay. Four target genes and one housekeeping gene were tested with RT-PCR assay. These genes include RUNX2, Colagen I, Osteopontin and Alkaline Phosphatase, GAPDH. RUNX2 (or cbfa1) is an osteoblast transcription factor, which is needed for osteoblast commitment [162]. Type I collagen is the most abundant bone matrix protein. It is also upregulated in the early period of osteoblast differentiation accompanying that of RUNX2 [163]. Osteopontin and ALP are also widely used as bone differentiation markers [164]. Expression profiles of these genes depict the interactions of human mesenchymal stem cells and hydrogel materials. With this information, we would like to pick out the best hydrogel matrix candidate and culturing condition.

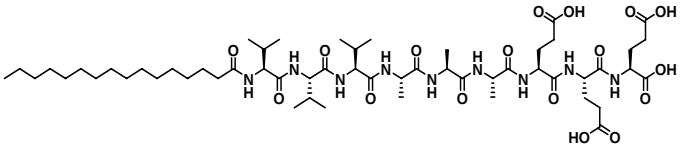

(a) PA1: $C_{15}H_{31}CO$-VVVAAAEEE(OH)

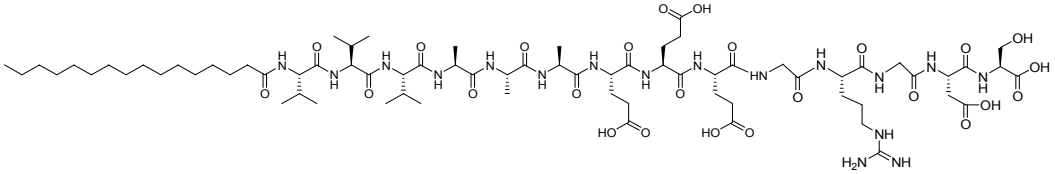

(b) PA2: $C_{15}H_{31}CO$-VVVAAAEEEGRGDS(OH)

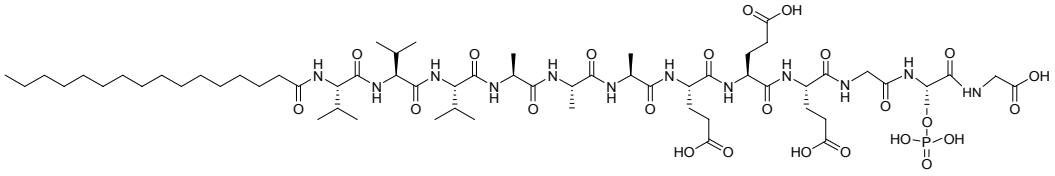

(c) PA3: $C_{15}H_{31}CO$-VVVAAAEEEGS(P)G(OH)

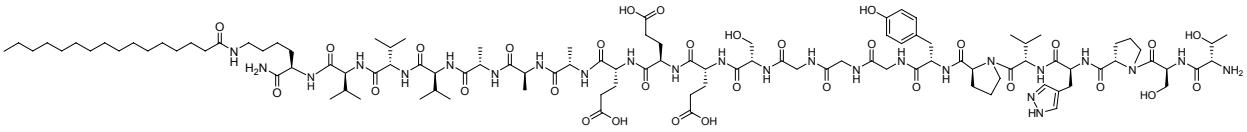

(d) PA4: $C_{11}H_{23}CO$-KVVVAAAEEESGGGYPVHPST(NH2)

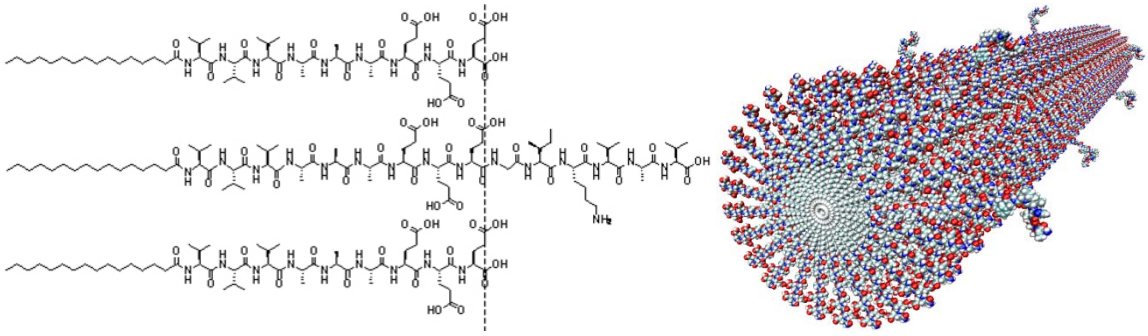

(e) Mixing of PA molecules with different functionalities

Figure 57 | PA molecules used in combinatorial study.

(**a**) PA1 : $C_{15}H_{31}CO$-VVVAAAEEE(OH), (**b**) PA2 : $C_{15}H_{31}CO$-VVVAAAEEEGRGDS(OH)

(**c**) PA3 : $C_{15}H_{31}CO$-VVVAAAEEEGS(P)G(OH)

(**d**) PA4 : $C_{11}H_{23}CO$-KVVVAAAEEESGGGYPVHPST(NH2)

(**e**) An illustration of PA molecules with different functionalities mixed together

5.3 Materials and Methods

5.3.1 Array Generation

5.3.1.1 Materials

All chemicals were purchased from Fisher or Aldrich and used as provided. Amino acid derivatives, derivatized resins were purchased from NovaBiochem (EMD Biosciences, CA, USA). All water used was deionized with a Millipore Milli-Q water purifier operating at a resistance of 18.2 M Ω. PAs were synthesized using a method previously described [81, 165]. After high performance liquid chromatography (HPLC) purification, they were lyophilized into powder and stored in -20 °C freezer before usage.

5.3.1.2 Cells and Growth Factor BMP2

MSCs have been shown to be capable of differentiating into multiple cell types including adipocytes, chondrocytes, osteocytes, hepatocytes, cardiomyocytes and neurons. In our study, human mesenchymal stem cells (Poietics™ hMSCs), growth media and osteogenic media were purchased from Lonza Walkersville, Inc., MD, USA. hMSCs used in the experiments were at passage 5-6. Media were changed every 3 or 4 days. The growth factor used in this study is bone morphogenetic protein (BMP2) (PeproTech Inc., NJ, USA), a member of the TGF-beta gene superfamily. When implanted locally to animals with appropriate carriers, recombinant human BMP2 (rhBMP2) produces very potent, ectopic bone forming activity. *In vitro*, rhBMP2 is also

shown to induce differentiation of mesenchymal stem cells into osteoblast and chondroblast cells. In the experiment, rhBMP2 was reconstituted in water containing BSA (50µg of BSA per 1µg of BMP2) to a concentration of 50 ng/µl before use.

5.3.1.3 Cell Encapsulation

With the help of Biomek FX 96 Multichannel and Biomek FX Span-8, combination array of PA molecules, mesenchymal stem cells, $CaCl_2$ solution and culture media can be made automatically. As cell is the only time sensitive component, it is added toward the end of this protocol before cross-linking reagent (calcium chloride) and culture media. Cell concentration in each gel is 1000 cells/µl, with 25,000 cells in each well. After encapsulation, media needed to be changed every 3 days.

To make sure cells survive and maintain their normal function in such hydrogel. We investigated the viability of cells encapsulated in the hydrogel arrays using LIVE/DEAD viability assay. In this assay, cells were soaked in 5µM Calcein AM and ethidium homodimer at 37°C for half an hour before examine with fluorescent microscopy. Live cells will be labeled green while dead cells labeled red. Therefore, it is evident that in Figure 58 encapsulated cells were viable in PA hydrogel.

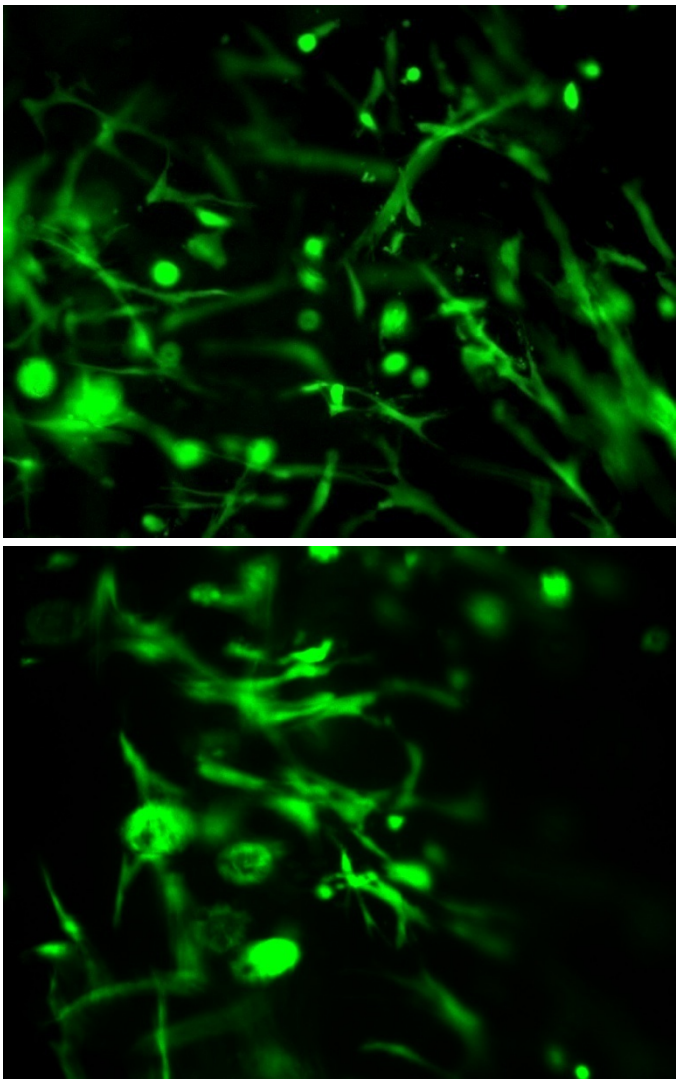

Figure 58 | Calcein AM live staining of hMSCs cultured for 14 days in hydrogel. Only a few cells were dead in the staining for dead cells. The staining of dead cells is not shown here due to intense autofluorescence from hydrogel matrix.

5.3.2 Cell Separation

After cells have been cultured for the desired period of time, they need to be separated from the matrix for RT-PCR. Otherwise, the negatively charged nanostructures will interact with divalent ions that are needed for reverse transcription or amplification process. This separation procedure needs to preserve the integrity of cell membrane in order to prevent RNA degradation. For this purpose, we have tried using different methods such as pepditase cleavage or EDTA degradation to remove PA matrix. Both methods were intended to be simple and low cost.

5.3.2.1 Peptidase-based Cell Separation

Peptide-cleaving peptidase includes endopeptidases and exopeptidase. Endopeptidases are enzymes which split peptides and polypeptides into smaller peptides by targeting break peptide bonds of nonterminal amino acids. Exopeptidases are enzymes that catalyze the cleavage of the terminal (last) or next-to-last peptide bond from a polypeptide or protein. Each peptidase only cleaves specific sites on the peptide chain. Among easily acquired peptidases, Elastase can potentially degrade the hydrogel matrix, because Elastase cleaves peptide bond from C-terminal of A, G, S, and V, which are abundant in the PA molecules we are using. The result however was not satisfactory, which may be caused by the inefficiency of elastase on supramolecular assemblies, or suboptimal parameters such as temperature, pH value and incubation. As EDTA-based methods showed promising results, we will not discuss peptidase method in detail.

5.3.2.2 EDTA-based Cell Separation

EDTA is widely used to sequester di- and trivalent metal ions (Ca^{2+} and Mg^{2+} for example). It binds to these ions via four carboxylate and two amine groups and forms especially strong complexes. With the removal of these ions, PA hydrogels formed with Ca^{2+} can be degraded into clear solution, which makes cell separation much easier. Shown in Figure 59, PA1 crosslinked with Ca^{2+} can be quickly degraded with EDTA into clear solution. Based on this mechanism, it is easy to understand that this method cannot be used on hydrogels formed with PA molecules of opposite charges (Figure 59). After PA gel is degraded by EDTA into clear solution, cells can be separated by filtration (Figure 60) or centrifugation (Figure 61). As the filter used in the filtration procedure adds to the cost and may decrease the yield by RNA binding on glass fiber, centrifugation is preferred.

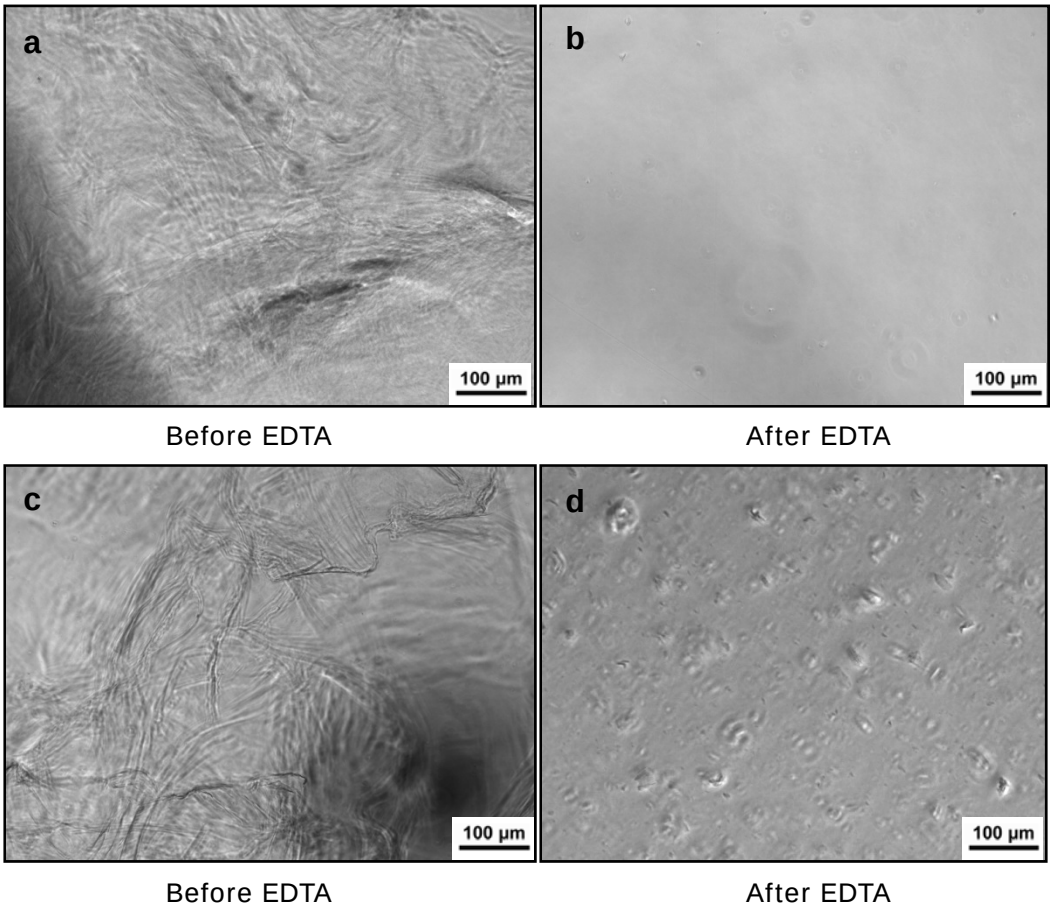

Figure 59 | Using EDTA to dissolve PA gel; **a,b,** EDTA can dissolve Ca^{2+} crosslinked PA gel into clear solution. **c,d,** PA molecules carry opposite charges form large aggregates that cannot be degraded by EDTA.

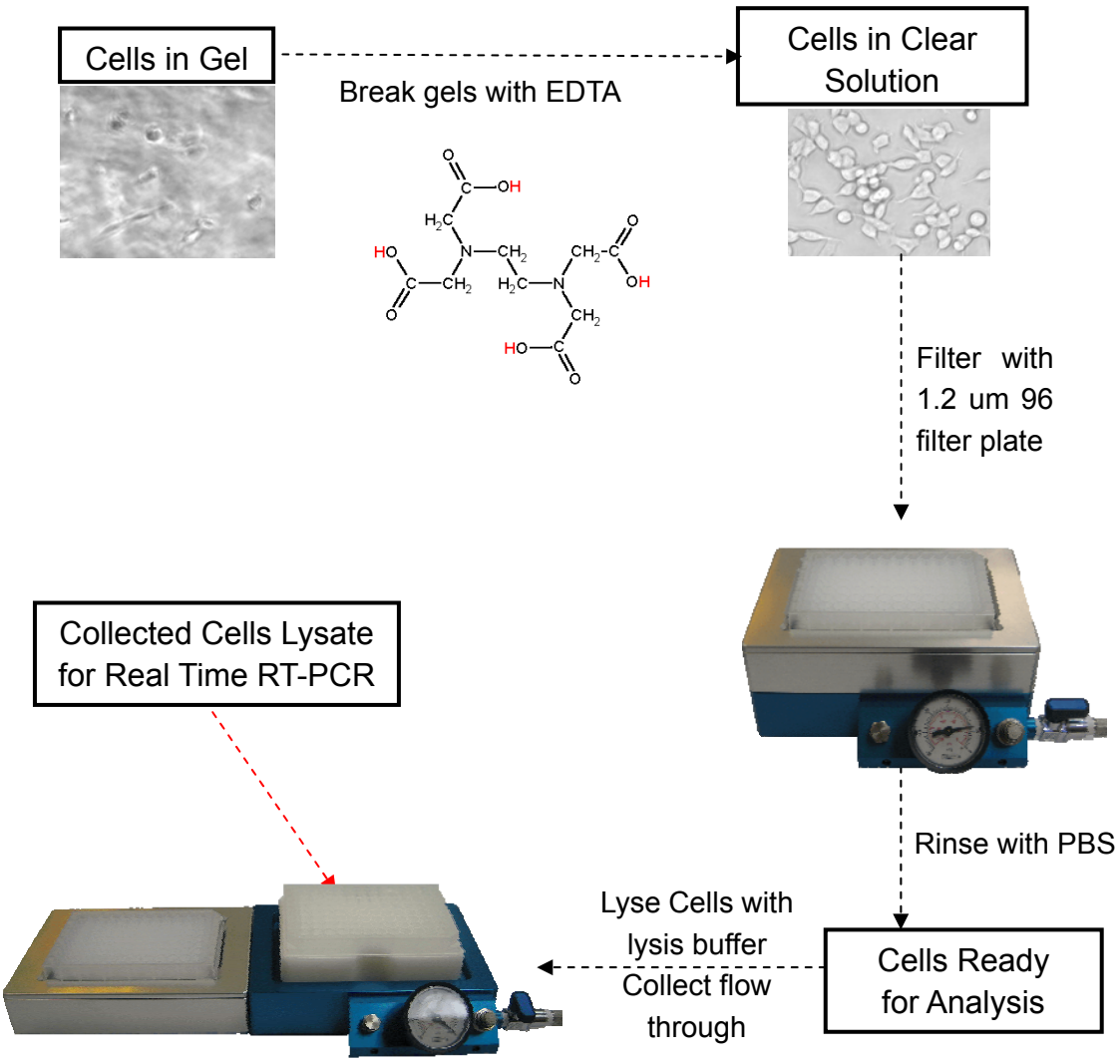

Figure 60 | Scheme for separating cells with filtration plate

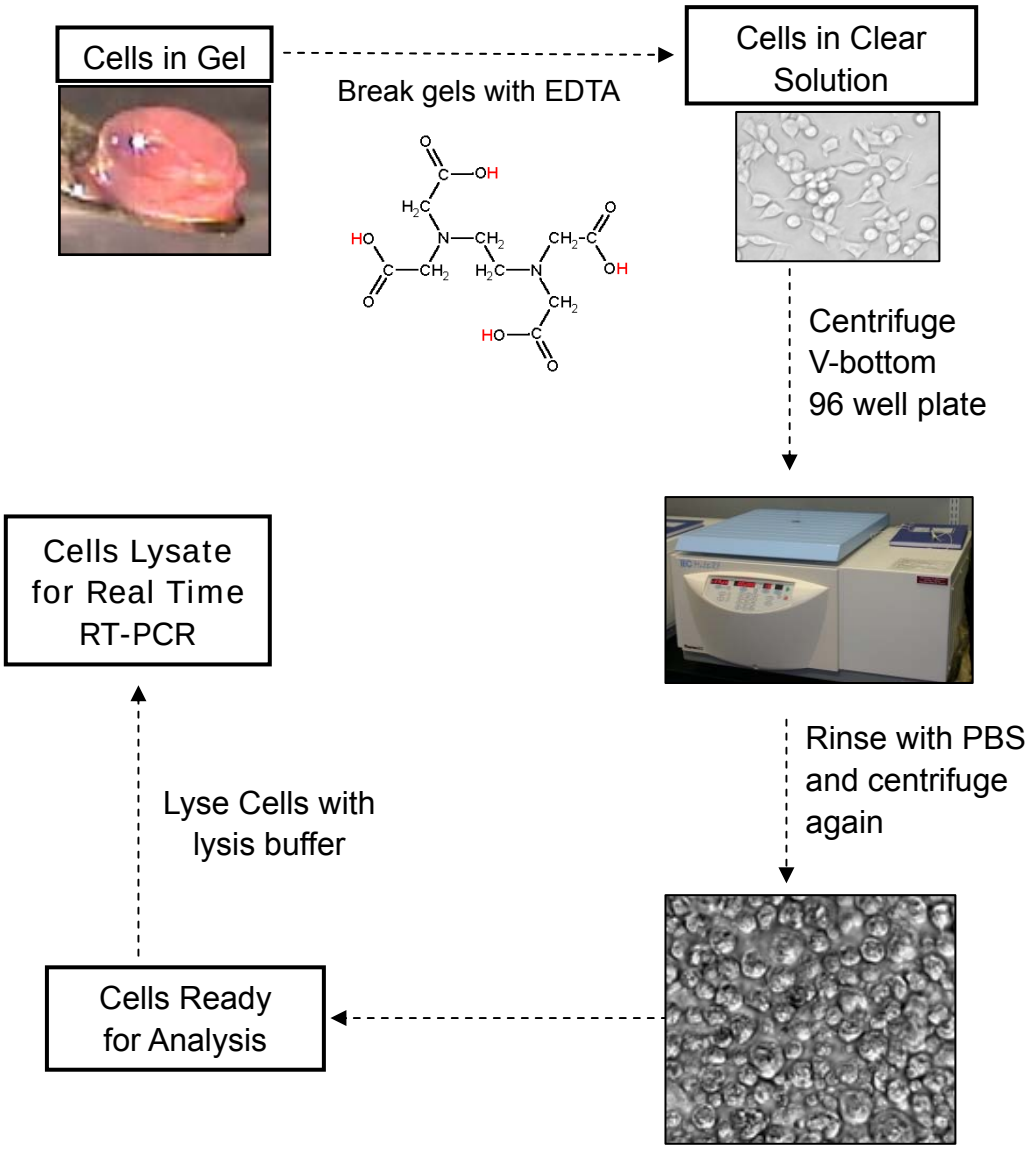

Figure 61 | Scheme for separating cells with centrifugation

5.3.3 RNA Isolation and Real Time RT-PCR

5.3.3.1 RNA Isolation

RNA extraction and purification process is in many cases the most problematic step of RT-PCR studies for samples of small cell numbers, large sample group or both. Various RNA isolation methods such as guanidinium thiocyanate-phenol-chloroform extraction[166], glass fiber filters[167], oligo(dT) functionalized matrix[168, 169] and magnetic beads [170-172] have been modified to facilitate parallel processing. However, RNA may not be efficiently recovered in many of these systems when cell input is very low [173, 174]. Recent development with magnetic beads is making some progress in this aspect. Other options, such as Cells to cDNA and Cells to Signal (Ambion Inc., TX, USA), are costly and don't support multiplex study very well.

Here we use MagMax-96 total RNA isolation kit (Ambion Inc., TX, USA) to isolate RNA after cells separation with centrifugation procedure described earlier. More specifically, cells were separated from PA by dissolving the gels with 20mM EDTA in PBS. Cells were then isolated with centrifugation at 1,000 g for 2-3 minutes. After removing supernatant, cells were lysed with lysis/binding solution provided in the MagMax-96 total RNA isolation kit. Magnetic beads functionalized with oligo (dT) were then added for RNA collection with 5 minutes pipetting. After two rinsing steps, RNA templates were washed off the beads into elution buffer and were then ready for RT-PCR.

5.3.3.2 One-step Real Time RT-PCR

One-step RT-PCR was carried out with iQ5 Real-Time PCR detection system (Bio-Rad, CA, USA) and Plexor One-Step qRT-PCR System [175, 176] (Promega Corp., WI, USA). The reaction components and thermal cycling procedure are listed in Figure 62. All RT-PCR assays were done with each reaction containing three different primer pairs labeled with FAM, Cal Fluor Orange 560 and Cal Fluor Red 610.

Component Listing for Plexor System	
Cells Lysate	5 µl
Reverse Transcriptase	0.2 µl
Nuclease-Free Water	4.8 µl
Control Gene Primer Pair	1.0 µl
Target Gene Primer Pair	1.0 µl
Plexor™ Master Mix	12.5 µl
RNasin® Plus RNase Inhibitor	0.5 µl

Thermo Cycles Programming		
Reverse Transcription	45 ℃ 5 min	
Denaturation/Enzyme Activation	95 ℃ 2 min	
Denaturation	95 ℃ 5 sec	] 40 cycle
Extension	60 ℃ 35 sec	
Melting Curve (0.5 ℃/8 sec)	60 ℃-95 ℃	

Figure 62 | Selecting RT-PCR systems: machine, kit and cycling conditions.

5.3.3.3 Primers

All primers were purchased from Biosearch Technologies, Inc., CA, USA. The reference

housekeeping gene glyceraldehyde-3-phosphate dehydrogenase (GAPDH) was purchased as pre-developed. Other primers were designed with primer3 [177] with sequence information published at http://Ensembl.org. Amplicons are about 110-180 base pairs. In each primer pair, a fluorescent dye was added to the 5' end of one primer. By positioning sense and antisense primers in exons flanking large introns all primer pairs amplify only mRNA [178, 179]. This assumption was proved by negative signals with no RT enzyme controls and single peak observed in melting curves. The genes and primer pairs used in this study can be found in Apendix 3. All primers have Tm between 63 and 65 °C.

5.3.4 Data Analysis

For data analysis, relative quantification method was used. Relative quantification (ΔΔCt) is an approach where researcher compares the Ct for a target in one sample versus the Ct of the same target in another sample. It determines the change in expression of a nucleic acid sequence (target) in a test sample relative to the same sequence in a calibrator sample. The target values were normalized by the amount of endogenous control, housekeeping gene GAPDH. From this comparison, the relative amount of target (the relative starting template amount) in each sample is calculated (e.g., fold change in experimental sample vs control sample). There is no requirement for determining template concentrations from standard curve. Moreover, it does not require that a standard curve be run in the same experiment for the purposes of quantization.

5.4 Results

5.4.1 One-step Multiplex RT-PCR Method Validation

Currently, the most popular RT-PCR protocols used in real time PCR are based on SYBR green dye or Taqman fluorescent probes. However, both of them have some limitations. Taqman probes have high specificity and accuracy but the consumable is too expensive to be used in arrayed samples with multiple target genes to detect. On the other hand, SYBR green dye is low in cost, but non-gene-specific. Each target has to be detected in a separate reaction well. The recent development in RT-PCR chemistry provided us a new alternative, the plexor system. Plexor primers are gene specific, low in cost and support one-step multiplex RT-PCR, where several RNA targets are analyzed in one reaction well without separate RT process. When dealing with large amount of samples, such improvement not only reduces cost, but also expedites data collection procedure.

In Figure 63, RNA isolated from 8000 hMSCs was prepared into a fourfold serial dilution series for one-step multiplex real time RT-PCR assay. Three mRNA targets endoglin (ENG), α-smooth muscle acting (ACTA2) and GAPDH were tested. This experiment is to test the feasibility of multiple target genes detection in one RT-PCR reaction. Representative plots of Ct value versus log10 of template input are presented in Figure 63. Amplifications showed high efficiencies and R^2 value across large detection range (E close to 1, back calculated from line slope $E=10^{-(1/slope)}-1$), indicating faithful amplification of templates. This result therefore

validated the one-step multiplex RT-PCR protocol to be used in following analysis in this chapter.

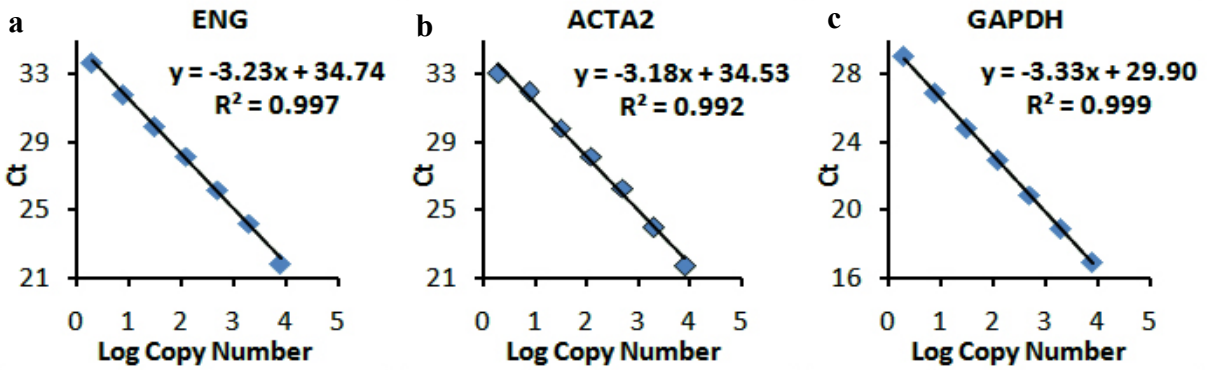

Figure 63 | One-step multiplex RT-PCR with fourfold dilution series of RNA isolated form 8000 hMSCs. Three targets can be tested in one reaction. Here we used ENG, ACTA2 and GAPDH. Result showed high RT-PCR high efficiency E ($E=10^{-(1/slope)}-1$) and R^2 values, which indicated faithful amplification of templates in all detected range and channels.

5.4.2 Small Scale Test

To further validate the whole data collection procedure, we started with a small scale test. Three PAs (F, F-S(P) and F-BMP2 were mixed together at various ratios as shown in Figure 64. The hydrogel were assessed after one month of culture in growth media. Besides the initial 0, 25 and 50 ng in the hydrogel, growth factor BMP2 was also supplemented with each media change at 0, 25 and 50 ng/ml in culture media. RNA isolation and RT-PCR assay were performed manually on these samples column by column. Expression levels of OPN in these samples were

tested, with three repeats for each.

Results in Figure 65 showed that cells cultured in the 8:1:1 combination of F, F-S(P) and F-BMP2 give the highest OPN expression after one month culture in growth media. And this trend is clear in three different tests. However, as we did not test them together due to limited manual handling capacity, the effect of growth factor was not obvious. This also justifies why robotic handling is needed for large scale assays.

	1	3	5		F : F-S(P) : F-BMP2
	0 ng BMP	25 ng BMP	50 ng BMP		
A	S01	S08	S15	←	10 : 0 : 0
B	S02	S09	S16	←	0 : 10 : 0
C	S03	S10	S17	←	9 : 1 : 0
D	S04	S11	S18	←	5 : 5 : 1
E	S05	S12	S19	←	9 : 0 : 1
F	S06	S13	S20	←	0 : 9 : 1
G	S07	S14	S21	←	8 :1 : 1
H				←	
	Growth Media				

Figure 64 | Small scale test combination scheme

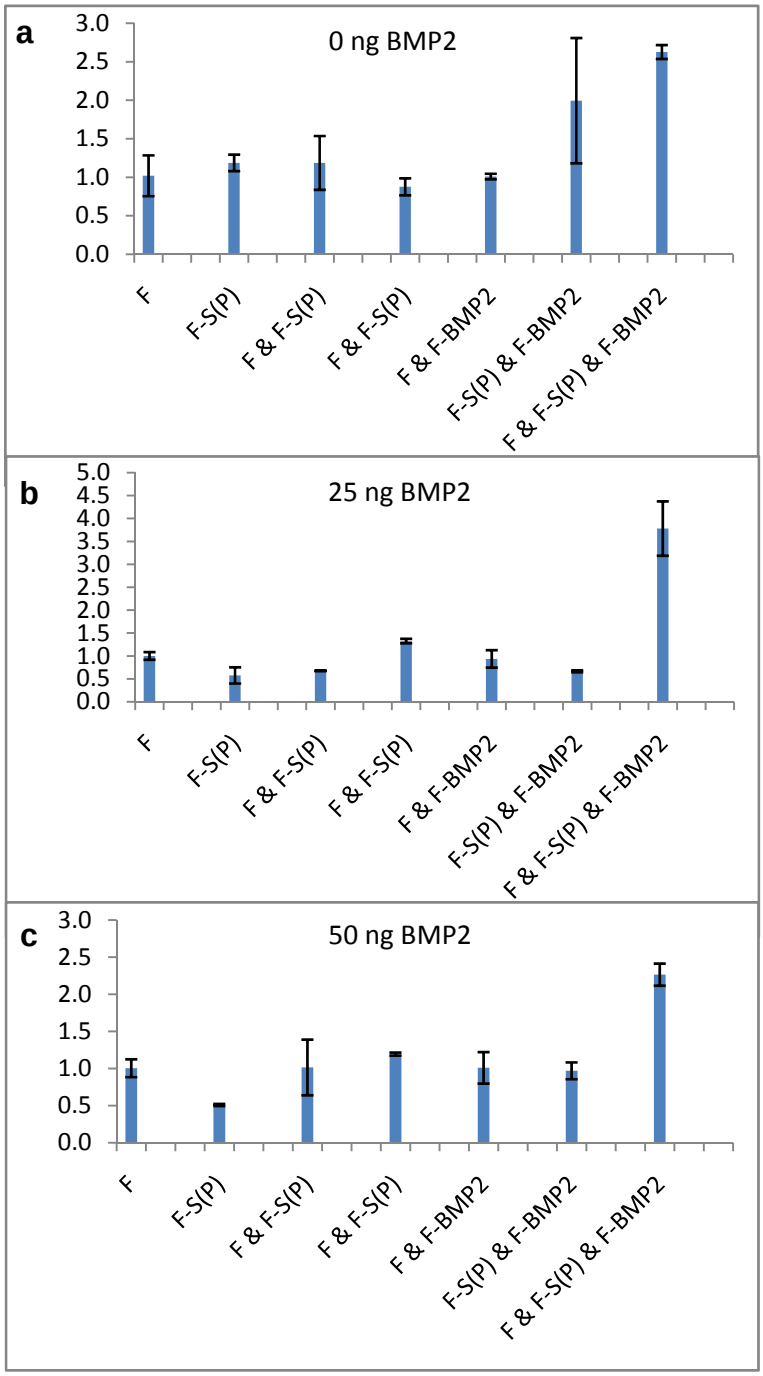

Figure 65 | OPN expression of hMSCs cultured in hydrogel combination as listed in Figure 64. Amount of encapsulated BMP2 is 0 ng in **a**, 25 ng in **b** and 50 ng in **c**. All result show the 8:1:1 combination of F, F-S(P) and F-BMP2 give the highest OPN expression after one month culture in growth media.

5.4.3 Full Plate Test

A full combinatorial plate as illustrated in Figure 56, was created with Biomek FX 96 Multichannel and Biomek FX Span-8 robot (details about the plate have been described in session 5.3). After cells had been cultured for 14 days, the plate was assessed and analyzed with the help of Biomek robots. Expression profile for each target gene was plotted as 2D bar graph in Figure 66.

The results showed a clear difference between OPN and ALP expression profile. In most of the case, hMSCs cultured in osteogenic media has higher ALP expression but lower OPN expression. Cells cultured in growth media, however, have opposite trend. This observation can be explained by OPN working as a biphasic osteogenic regulator [119]. At early stage of differentiation process, it serves as a negative regulator. The result listed in 5.4.2 therefore needs more careful interpretation. COL1A1 and RUNX2 data showed that cells cultured in growth media have slightly more collagen and less RUNX2. These unoptimized result showed high variability in duplicate measurements, therefore improvement is needed for further interpretation of data.

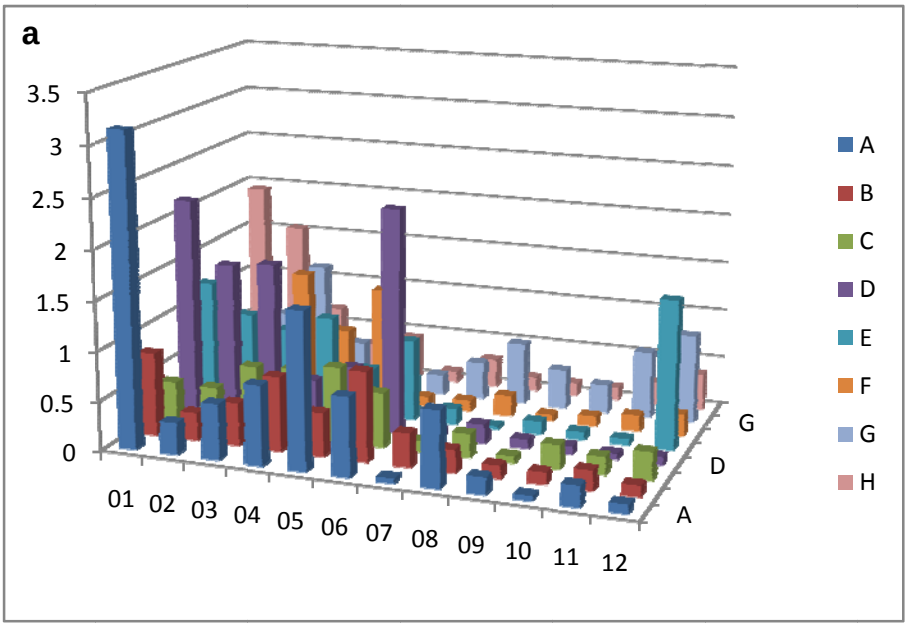

OPN Expression Profile

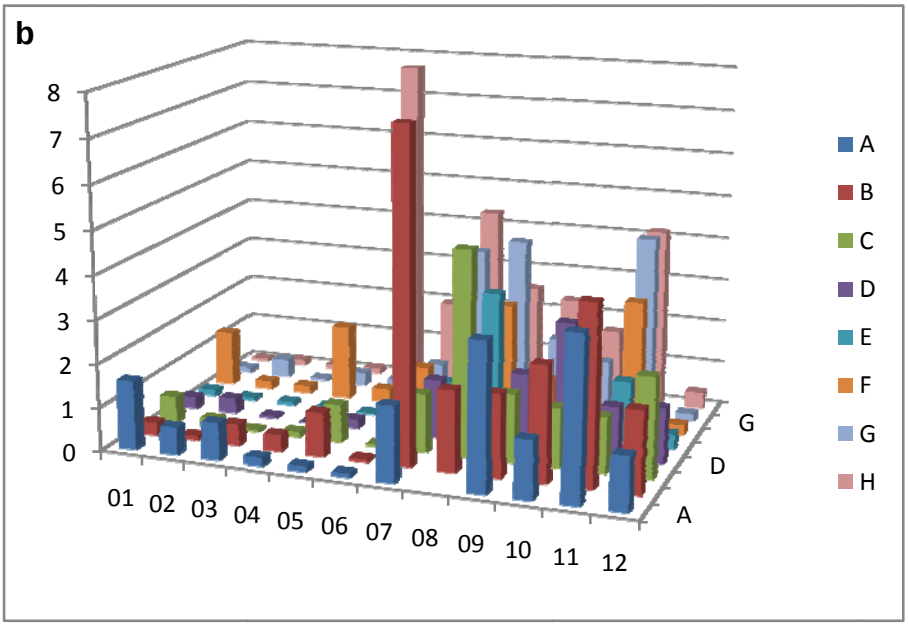

ALP Expression Profile

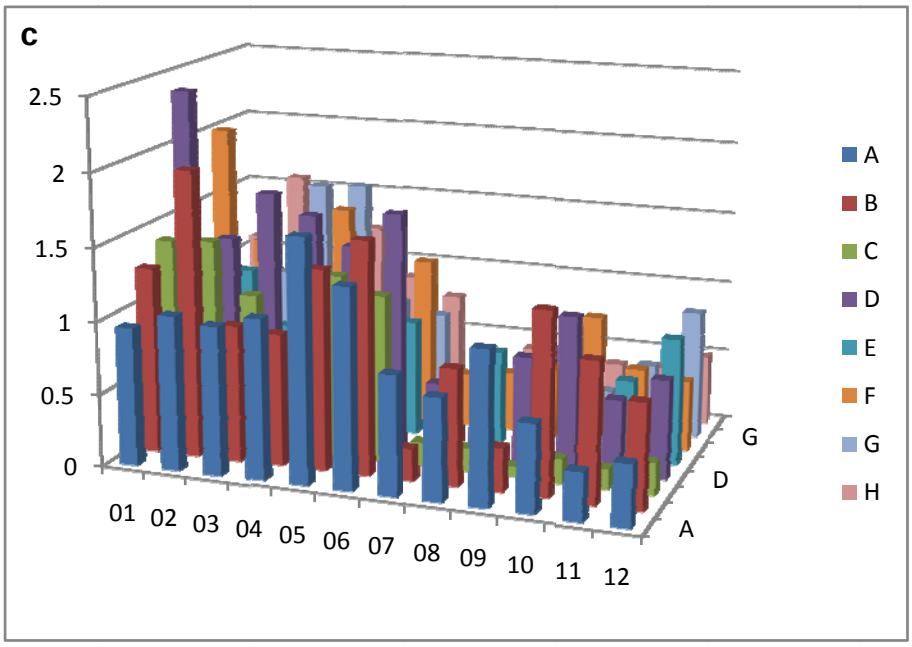

COL1A1 Expression Profile

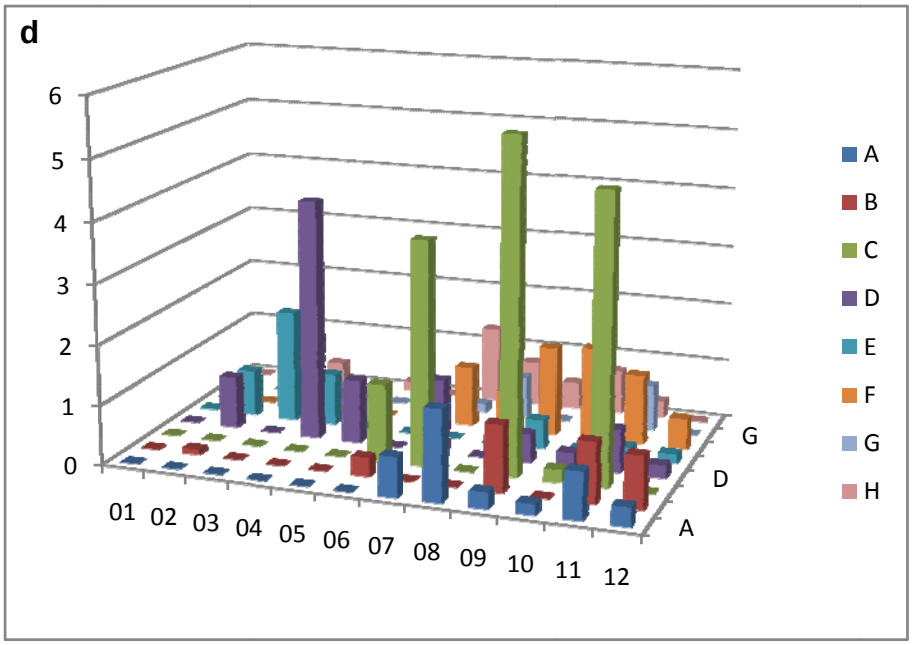

RUNX2 Expression Profile

Figure 66 | Relative quantification of gene expression profile of hMSCs' cultured in combinatory hydrogel array. Refer to section 5.2 for array detail. Tested targets include **a,** OPN **b,** ALP **c,** COL1A1 **d,** RUNX2.

5.5 Discussion

In previous sections of this chapter, we have established the methods for cells encapsulation, cells separation, RNA isolation, RT-PCR protocols and data analysis methods. The remaining stumbling block is the reliability of RT-PCR data collection. The whole data collection procedure includes cells separation, RNA isolation, and RT-PCR. In 5.4.1, we already validated the RT-PCR method. Therefore, improvement should focus on more reliable method to isolate RNA and preserve them before amplification. RNA isolation is commonly practiced in biology research. There are many ways that researchers can get high quality RNA. The unique challenges we have, however, is how to reliably isolate RNA from small amount of cells that are trapped in many individual hydrogels. The existence of PA molecules and the need for simplified protocol also present additional obstacles for acquiring high quality RNA.

To solve these problems, we can try combining the cells separation and RNA isolation steps. Using organic solvents, such as Trizol reagent, with chloroform extraction, hydrogel and cells can be degraded together. RNA and PA molecules will then concentrate in organic and aqueous phase separately. After separation, RNA in the aqueous phase can be collected with magnetic beads based isolation kit. As these reagents contain substance that inhibits RNase activities, RNA templates can be protected from the beginning. Such process requires facilitation of liquid handling machine Biomek FX 96. After isolation, we can also add RNase inhibitor enzyme in storage solution to protect RNA during the storage before usage. With these measures,

quality of RNA should be able to improve, which eventually would result in more reliable data.

5.6 Summary

In this chapter, we investigated the strategies and methods to create and analyze combinatorial hydrogel array with encapsulated cells. To create such array, PA molecules carrying different epitopes were mixed at various ratios with growth factors and cells. After culturing, cells were separated from PA gels for RNA isolation and downstream RT-PCR assay. To analyze cells' interactions with this combinatorial hydrogel array, we first proved that with small amount of cells, RNA can be isolated and analyzed by one-step multiplex RT-PCR. Then we showed cells cultured in different hydrogel combination have different mRNA expression pattern. While the system still needs more optimization, it could potentially facilitate our efforts for discovering material candidates to be used in biomedical applications.

References and Notes

1. Vonrecum, A.F. and M. Laberge, *Educational-Goals for Biomaterials Science and Engineering - Prospective View.* Journal of Applied Biomaterials, 1995. **6**(2): p. 137-144.

2. Williams, H.P., *Sir Harold Ridley's vision.* Br. J. Ophthalmol. , 2001. **85** (9): p. 1022.

3. Ratner, B.D., *Biomaterials Science: An Introduction to Materials in Medicine* 1st ed. 2004, San Diego: Elsevier Academic Press.

4. Dumitriu, S., *Polymeric Biomaterials*. 2nd ed. 2002, New York: Marcel Dekker.

5. Hench, L.L. and E.C. Ethridge, *Biomaterials: An Interfacial Approach* 1982, San Diego: Academic Press.

6. Bronzio, J.D., *The Biomedical Engineering Handbook*. 1995, Boca Raton, Fla.: CRC Press.

7. Jandt, K.D., *Evolutions, revolutions and trends in biomaterials science - A perspective.* Advanced Engineering Materials, 2007. **9**(12): p. 1035-1050.

8. Biehl, V. and J. Breme, *Metallic biomaterials.* Materialwissenschaft Und Werkstofftechnik, 2001. **32**(2): p. 137-141.

9. Stupp, S.I., *Biomaterials for regenerative medicine.* Mrs Bulletin, 2005. **30**(7): p. 546-553.

10. Sarikaya, M., et al., *Molecular biomimetics: nanotechnology through biology.* Nature Materials, 2003. **2**(9): p. 577-585.

11. Fratzl, P. and R. Weinkamer, *Nature's hierarchical materials.* Progress in Materials Science, 2007. **52**(8): p. 1263-1334.

12. Stupp, S.I., et al., *Expanding frontiers in biomaterials.* Mrs Bulletin, 2005. **30**(11): p. 864-873.

13. http://brainmaps.org.

14. Kibiuk, L., *Neuron Migration and Brain Disorders.* Society for Neuroscience, 1995.

15. Stupp, S.I., *Introduction to functional nanostructures.* Chemical Reviews, 2005. **105**(4): p. 1023-1024.

16. Whitesides, G.M. and B. Grzybowski, *Self-Assembly at All Scales.* Science, 2002. **295**(5564): p. 2418-2421.

17. Lehn, J.-M., *Toward Self-Organization and Complex Matter.* Science, 2002. **295**: p. 2400-2403.

18. Lehn, J.M., *Supramolecular Chemistry*. 1995, New York: VCH Press.

19. Reinhoudt, D.N. and M. Crego-Calama, *Synthesis Beyond the Molecule.* Science, 2002. **295**: p. 2403-2407.

20. Ikkala, O. and G.t. Brinke, *Functional Materials Based on Self-Assembly of Polymeric Supramolecules.* Science, 2002. **295**: p. 2407-2409.

21. Kato, T., *Self-Assembly of Phase-Segregated Liquid Crystal Structures.* Science, 2002. **295**: p. 2414-2418.

22. Whitesides, G.M., et al., *Noncovalent Synthesis - Using Physical-Organic Chemistry to Make Aggregates.* Acc. Chem. Res. , 1995. **28**: p. 37-44.

23. Stupp, S.I., et al., *Supramolecular Materials: Self-Organized Nanostructures.* Science, 1997. **276**: p. 384-389.

24. Jolliffe, K.A., P. Timmerman, and D.N. Reinhoudt, *Noncovalent Assembly of a Fifteen-Component Hydrogen-Bonded Nanostructure.* Angew. Chem. Int. Ed., 1999. **38**: p. 933-937.

25. Thurmond, K.B., T. Kowalewski, and K.L. Wooley, *Shell Cross-Linked Knedels: A Synthetic Study of the Factors Affecting the Dimensions and Properties of Amphiphilic Core-Shell Nanospheres.* J. Am. Chem. Soc., 1997. **119**: p. 6656-6665.

26. Hartgerink, J.D., E. Beniash, and S.I. Stupp, *Self-Assembly and Mineralization of Peptide-Amphiphile Nanofibers.* Science, 2001. **294**(5527): p. 1684-1688.

27. Hartgerink, J.D., E. Beniash, and S.I. Stupp, *Peptide-amphiphile nanofibers: A versatile scaffold for the preparation of self-assembling materials.* Proc. Natl. Acad. Sci. U.S.A., 2002. **99**(8): p. 5133-5138.

28. Hill, J.P., et al., *Self-Assembled Hexa-peri-hexabenzocoronene Graphitic Nanotube.* Science, 2004. **304**(5676): p. 1481-1483.

29. Messmore, B.W., et al., *Synthesis, self-assembly, and characterization of supramolecular*

polymers from electroactive dendron rodcoil molecules. J. Am. Chem. Soc., 2004. **126**(44): p. 14452-14458.

30. Messmore, B.W. and S.I. Stupp, *Mirror Image Nanostructures.* Journal of the American Chemical Society, 2005. **127**(22): p. 7992-7993.

31. Kurth, D.G., N. Severin, and J.P. Rabe, *Perfectly Straight Nanostructures of Metallosupramolecular Coordination-Polyelectrolyte Amphiphile Complexes on Graphite.* Angew. Chem. Int. Ed., 2002. **41**: p. 3681-3683.

32. Schenning, A., et al., *Supramolecular Organization of Alpha,Alpha '-Disubstituted Sexithiophenes.* J. Am. Chem. Soc., 2002. **124**: p. 1269-1275.

33. Bowden, N.T., A.; Carbeck, J.; Whitesides, G. M, *Self-Assembly of Mesoscale Objects into Ordered Two-Dimensional Arrays.* Science, 1997. **276**: p. 233-235.

34. Stupp, S.I., et al., *Bulk Synthesis of 2-Dimensional Polymers - the Molecular Recognition Approach.* Journal of the American Chemical Society, 1995. **117**(19): p. 5212-5227.

35. Krejchi, M.T.A., E. D. T.; Waddon, A. J.; Fournier, M. J.; Mason, T. L.; Tirrell, D. A., *Chemical Sequence Control of Beta-Sheet Assembly in Macromolecular Crystals of Periodic Polypeptides.* Science, 1994. **265**: p. 1427-1432.

36. Kato, T.K., H.; Kumar, U.; Uryu, T.; Frechet, J. M. J., *A Liquid-Crystalline Polymer Network Built by Molecular Self-Assembly through Intermolecular Hydrogen-Bonding.* Angew. Chem. Int. Ed., 1994. **33**: p. 1644-1645.

37. Kato, T.F., J. M. J., *New Approach to Mesophase Stabilization through Hydrogen-Bonding Molecular-Interactions in Binary-Mixtures.* J. Am. Chem. Soc., 1989. **111**: p. 8533-8534.

38. Hamley, I.W., *Nanotechnology with soft materials.* Angew. Chem. Int. Ed., 2003. **42**: p. 1692-1712.

39. Hoeben, F.J.M., et al., *About Supramolecular Assemblies of pi-Conjugated Systems.* Chem. Rev., 2005. **105**(4): p. 1491-1546.

40. Steed, J.W. and J.L. Atwood, *Supramolecular Chemistry*. 2000, Chichester: Wiley & Sons.

41. Tirrell, M., E. Kokkoli, and M. Biesalski, *The role of surface science in bioengineered materials.* Surface Sci., 2002. **500**: p. 61-83.

42. Doig, A.J.W., D. H., *Binding-Energy of an Amide Amide Hydrogen-Bond in Aqueous and Nonpolar-Solvents.* J. Am. Chem. Soc., 1992. **114**: p. 338-343.

43. Wilbur, J.L., et al., *Scanning Force Microscopies Can Image Patterned Self-Assembled Monolayers.* Langmuir, 1995. **11**(3): p. 825-831.

44. Alivisatos, A.P., et al., *From molecules to materials: Current trends and future directions.* Advanced Materials, 1998. **10**(16): p. 1297-1336.

45. Stupp, S.I., *Biomaterials for Regenerative Medicine.* MRS Bull., 2005. **30**(7): p. 546-553.

46. Stupp, S.I., et al., *Expanding frontiers in biomaterials.* MRS Bull., 2005. **30**(11): p. 864-873.

47. Stendahl, J.C., et al., *Intermolecular forces in the self-assembly of peptide amphiphile nanofibers.* Adv. Funct. Mater., 2006. **16**: p. 499-508.

48. Guler, M.O., et al., *Presentation of RGDS Epitopes on Self-Assembled Nanofibers of Branched Peptide Amphiphiles.* Biomacromol., 2006. **7**(6): p. 1855-1863.

49. Rajangam, K., et al., *Heparin Binding Nanostructures to Promote Growth of Blood Vessels* Nano Lett., 2006. **6**(9): p. 2086-2090.

50. Jiang, H. and S.I. Stupp, *Dip-Pen Patterning and Surface Assembly of Peptide Amphiphiles.* Langmuir, 2005. **21**(12): p. 5242-5246.

51. Silva, G.A., et al., *Selective Differentiation of Neural Progenitor Cells by High-Epitope Density Nanofibers.* Science, 2004. **303**(5662): p. 1352-1355.

52. Zubarev, E.R. and S.I. Stupp, *Dendron rodcoils: Synthesis of novel organic hybrid structures.* Journal of the American Chemical Society, 2002. **124**(20): p. 5762-5773.

53. Li, L.M., et al., *Chemical structure and nonlinear optical properties of polar self-assembling films.* Macromolecules, 2002. **35**(7): p. 2560-2565.

54. Stupp, S.I., et al., *Self-assembly of organic nano-objects into functional materials.* MRS Bull., 2000. **25**(4): p. 42-48.

55. Braun, P.V., et al., *Nanostructure templating in inorganic solids with organic lyotropic liquid crystals.* Journal of the American Chemical Society, 1999. **121**(32): p. 7302-7309.

56. Stupp, S.I., *Self-assembly of rod-coil molecules.* CURRENT OPINION IN COLLOID & INTERFACE SCIENCE, 1998. **3**(1): p. 20-26.

57. Stupp, S.I., *The challenge of assembling molecules into materials.* Macromolecular Symposia, 1997. **117**: p. 1-9.

58. Anderson, D.G., J.A. Burdick, and R. Langer, *Smart Biomaterials.* Science, 2004. **305**: p. 1923.

59. Bitton, R., et al., *Self-Assembly of Model DNA-Binding Peptide Amphiphiles.* Langmuir, 2005. **21**(25): p. 11888-11895.

60. Gore, T., et al., *Self-Assembly of Model Collagen Peptide Amphiphiles.* Langmuir, 2001. **17**(17): p. 5352-5360.

61. Yu, Y.-C., M. Tirrell, and G.B. Fields, *Minimal Lipidation Stabilizes Protein-Like Molecular Architecture.* J. Am. Chem. Soc., 1998. **120**(39): p. 9979-9987.

62. Hartgerink, J.D., et al., *Self-Assembling Peptide Nanotubes.* J. Am. Chem. Soc., 1996. **118**(1): p. 43-50.

63. Klok, H.A., et al., *Self-assembling biomaterials: L-lysine-dendron-substituted cholesteryl-(L-lactic acid)n.* Macromolecules, 2002. **35**(16): p. 6101-6111.

64. Paramonov, S.E., H.-W. Jun, and J.D. Hartgerink, *Self-Assembly of Peptide-Amphiphile Nanofibers: The Roles of Hydrogen Bonding and Amphiphilic Packing.* J. Am. Chem. Soc., 2006. **128**: p. 7291-7298.

65. Bellomo, E.G., et al., *Stimuli-responsive polypeptide vesicles by conformation-specific assembly.* Nature Materials, 2004. **3**(4): p. 244-248.

66. Lamm, M.S., et al., *Laminated Morphology of Nontwisting -Sheet Fibrils Constructed via Peptide Self-Assembly.* J. Am. Chem. Soc., 2005. **127**(47): p. 16692-16700.

67. Pochan, D.J., et al., *Toroidal Triblock Copolymer Assemblies.* Science, 2004. **306**: p. 94-97.

68. Yamada, N., et al., *Regulation of b-Sheet Structures within Amyloid-Like -Sheet Assemblage from Tripeptide Derivatives.* J. Am. Chem. Soc., 1998. **120**(47): p. 12192-12199.

69. Yamada, Y. and H.K. Kleinman, *Functional domains of cell adhesion molecules.* Curr. Opin. Cell Biol., 1992. **4**: p. 819-823.

70. Behanna, H.A., et al., *Coassembly of Amphiphiles with Opposite Peptide Polarities into*

Nanofibers. J. Am. Chem. Soc., 2005. **127**(4): p. 1193-1200.

71. Guler, M.O., et al., *Presentation and Recognition of Biotin on Nanofibers Formed by Branched Peptide Amphiphiles.* Nano Lett., 2005. **5**(2): p. 249-252.

72. Tover, J.D., R.C. Claussen, and S.I. Stupp, *Probing the Interior of Peptide Amphiphile Supramolecular Aggregates.* J. Am. Chem. Soc., 2005. **127**(20): p. 7337-7345.

73. Li, L.S. and S.I. Stupp, *One-dimensional assembly of lipophilic inorganic nanoparticles templated by peptide-based nanofibers with binding functionalities.* Angewandte Chemie-International Edition, 2005. **44**(12): p. 1833-1836.

74. Stendahl, J.C., et al., *Structural modifications to polystyrene via self-assembling molecules.* Advanced Functional Materials, 2005. **15**(3): p. 487-493.

75. Solis, F.J., S.I. Stupp, and M.O. de la Cruz, *Charge induced pattern formation on surfaces: Segregation in cylindrical micelles of cationic-anionic peptide-amphiphiles.* J. Chem. Phys., 2005. **122**(5): p. 054905.

76. Bull, S.R., et al., *Self-assembled peptide amphiphile nanofibers conjugated to MRI contrast agents.* Nano Letters, 2005. **5**(1): p. 1-4.

77. Beniash, E., et al., *Self-assembling Peptide Amphiphile Nanofiber Matrices for Cell Entrapment.* Acta Biomaterialia, 2005. **1**(4): p. 387-397.

78. Arnold, M.S., et al., *Encapsulation of Carbon Nanotubes by Self-Assembling Peptide Amphiphiles.* Langmuir, 2005. **21**(10): p. 4705-4709.

79. Spoerke, E.D. and S.I. Stupp, *Synthesis of a poly(L-lysine)-calcium phosphate hybrid on titanium surfaces for enhanced bioactivity.* Biomaterials, 2005. **26**(25): p. 5120-5129.

80. Guler, M.O., et al., *Enhanced oligonucleotide binding to self-assembled nanofibers.* Bioconjugate Chemistry, 2005. **16**(3): p. 501-503.

81. Hartgerink, J.D., E. Beniash, and S.I. Stupp, *Self-assembly and mineralization of peptide-amphiphile nanofibers.* Science, 2001. **294**(5547): p. 1684-1688.

82. Hartgerink, J.D., E. Beniash, and S.I. Stupp, *Peptide-amphiphile nanofibers: A versatile scaffold for the preparation of self-assembling materials.* Proceedings of the National Academy of Sciences of the United States of America, 2002. **99**(8): p. 5133-5138.

83. Paramonov, S.E., H.W. Jun, and J.D. Hartgerink, *Self-assembly of peptide-amphiphile*

nanofibers: The roles of hydrogen bonding and amphiphilic packing. Journal of the American Chemical Society, 2006. **128**(22): p. 7291-7298.

84. Storrie, H., et al., *Supramolecular Crafting of Cell Adhesion.* in preparation.

85. Whitesides, G.M., J.P. Mathias, and C.T. Seto, *Molecular Self-Assembly and Nanochemistry - a Chemical Strategy for the Synthesis of Nanostructures.* Science, 1991. **254**(5036): p. 1312-1319.

86. Reches, M. and E. Gazit, *Casting metal nanowires within discrete self-assembled peptide nanotubes.* Science, 2003. **300**(5619): p. 625-627.

87. Kim, S.O., et al., *Epitaxial self-assembly of block copolymers on lithographically defined nanopatterned substrates.* Nature, 2003. **424**(6947): p. 411-414.

88. Nelson, R., et al., *Structure of the cross-beta spine of amyloid-like fibrils.* Nature, 2005. **435**(7043): p. 773-778.

89. Dobson, C.M., *Protein folding and misfolding.* Nature, 2003. **426**(6968): p. 884-890.

90. Ward, M.D., *Directing the assembly of molecular crystals.* MRS Bull., 2005. **30**(10): p. 705-712.

91. Percec, V., et al., *Self-organization of supramolecular helical dendrimers into complex electronic materials.* Nature, 2002. **419**(6905): p. 384-387.

92. Hasenknopf, B., et al., *Self-assembly of a circular double helicate.* Angewandte Chemie-International Edition in English, 1996. **35**(16): p. 1838-1840.

93. Hill, J.P., et al., *Self-assembled hexa-peri-hexabenzocoronene graphitic nanotube.* Science, 2004. **304**(5676): p. 1481-1483.

94. Stupp, S.I., et al., *Supramolecular materials: Self-organized nanostructures.* Science, 1997. **276**(5311): p. 384-389.

95. Jonkheijm, P., et al., *Probing the solvent-assisted nucleation pathway in chemical self-assembly.* Science, 2006. **313**(5783): p. 80-3.

96. Ruzette, A.V. and L. Leibler, *Block copolymers in tomorrow's plastics.* Nature Materials, 2005. **4**(1): p. 19-31.

97. Matsen, M.W. and F.S. Bates, *Unifying weak- and strong-segregation block copolymer theories.* Macromolecules, 1996. **29**(4): p. 1091-1098.

98. Cui, H.G., et al., *Block copolymer assembly via kinetic control.* Science, 2007. **317**(5838): p. 647-650.

99. Behanna, H.A., et al., *Coassembly of amphiphiles with opposite peptide polarities into nanofibers.* Journal of the American Chemical Society, 2005. **127**(4): p. 1193-1200.

100. Ruberti, J.W., et al., *Quick-freeze/deep-etch visualization of age-related lipid accumulation in Bruch's membrane.* Investigative Ophthalmology & Visual Science, 2003. **44**(4): p. 1753-1759.

101. Bull, S.R., et al., *Magnetic resonance imaging of self-assembled biomaterial scaffolds.* Bioconjugate Chemistry, 2005. **16**(6): p. 1343-1348.

102. *DLVO theory, Derjaguin, Landau, Verwey and Overbeek, 1940s.*

103. Caplan, M.R., et al., *Self-assembly of a beta-sheet protein governed by relief of electrostatic repulsion relative to van der Waals attraction.* Biomacromolecules, 2000. **1**(4): p. 627-631.

104. *Developed with Megan Greenfield, Dr. Liam Palmer, Prof. Monica Olvera de la Cruz and Prof. Samuel I. Stupp*. 2008.

105. Jiang, H.Z., M.O. Guler, and S.I. Stupp, *The internal structure of self-assembled peptide amphiphiles nanofibers.* Soft Matter, 2007. **3**(4): p. 454-462.

106. Missel, P.J., et al., *Thermodynamic Analysis of the Growth of Sodium Dodecyl-Sulfate Micelles.* Journal of Physical Chemistry, 1980. **84**(9): p. 1044-1057.

107. Li, L.S., et al., *A torsional strain mechanism to tune pitch in supramolecular helices.* Angewandte Chemie-International Edition, 2007. **46**(31): p. 5873-5876.

108. Muraoka, T., H. Cui, and S.I. Stupp, *Quadruple helix formation of a photoresponsive peptide amphiphile and its light-triggered dissociation into single fibers.* Journal of the American Chemical Society, 2008. **130**(10): p. 2946-2947.

109. Larson, R.G. and D.W. Mead, *The Ericksen Number and Deborah Number Cascades in Sheared Polymeric Nematics.* Liquid Crystals, 1993. **15**(2): p. 151-169.

110. Greiner, A. and J.H. Wendorff, *Electrospinning: A fascinating method for the preparation of ultrathin fibres.* Angewandte Chemie-International Edition, 2007. **46**(30): p. 5670-5703.

111. Salalha, W., et al., *Encapsulation of bacteria and viruses in electrospun nanofibres.* Nanotechnology, 2006. **17**(18): p. 4675-4681.

112. Gensheimer, M., et al., *Novel biohybrid materials by electrospinning: Nanofibers of poly(ethylene oxide) and living bacteria.* Advanced Materials, 2007. **19**(18): p. 2480-+.

113. Xu, C.Y., et al., *Aligned biodegradable nanofibrous structure: a potential scaffold for blood vessel engineering.* Biomaterials, 2004. **25**(5): p. 877-86.

114. Yang, F., et al., *Electrospinning of nano/micro scale poly(L-lactic acid) aligned fibers and their potential in neural tissue engineering.* Biomaterials, 2005. **26**(15): p. 2603-2610.

115. Lin, T., et al., *Using chitosan as a thickener for electrospinning dilute PVA solutions to improve fibre uniformity.* Nanotechnology, 2006. **17**(15): p. 3718-3723.

116. Yu, J.H., S.V. Fridrikh, and G.C. Rutledge, *The role of elasticity in the formation of electrospun fibers.* Polymer, 2006. **47**(13): p. 4789-4797.

117. Dersch, R., et al., *Electrospun nanofibers: Internal structure and intrinsic orientation.* Journal of Polymer Science Part a-Polymer Chemistry, 2003. **41**(4): p. 545-553.

118. Tranquillo, R.T., *Self-organization of tissue-equivalents: the nature and role of contact guidance.* Biochem Soc Symp, 1999. **65**: p. 27-42.

119. Huang, W.B., et al., *Osteopontin is a negative regulator of proliferation and differentiation in MC3T3-E1 pre-osteoblastic cells.* Bone, 2004. **34**(5): p. 799-808.

120. Engler, A.J., et al., *Matrix elasticity directs stem cell lineage specification.* Cell, 2006. **126**(4): p. 677-89.

121. Nie, Z.H. and E. Kumacheva, *Patterning surfaces with functional polymers.* Nature Materials, 2008. **7**(4): p. 277-290.

122. Nerem, R.M. and D. Seliktar, *Vascular tissue engineering.* Annual Review of Biomedical Engineering, 2001. **3**: p. 225-243.

123. Vaz, C.M., et al., *Design of scaffolds for blood vessel tissue engineering using a multi-layering electrospinning technique.* Acta Biomaterialia, 2005. **1**(5): p. 575-582.

124. Eschenhagen, T. and W.H. Zimmermann, *Engineering myocardial tissue.* Circulation Research, 2005. **97**(12): p. 1220-1231.

125. Nishikawa, S., *Correlation of the Arrangement Pattern of Enamel Rods and Secretory*

Ameloblasts in Pig and Monkey Teeth - a Possible Role of the Terminal Webs in Ameloblast Movement during Secretion. Anatomical Record, 1992. **232**(4): p. 466-478.

126. Dickson, B.J., *Molecular mechanisms of axon guidance.* Science, 2002. **298**(5600): p. 1959-1964.

127. Bellairs R, C.A., Dunn G, *Contact guidance of cultured tissue cells: a survey of potentially relevance properties of the substratum.* Cell behavior. Cambridge: Cambridge University Press, 1982: p. 247-280.

128. Zhu, B., et al., *Nanotopographical guidance of C6 glioma cell alignment and oriented growth.* Biomaterials, 2004. **25**(18): p. 4215-23.

129. Hung, A.M. and S.I. Stupp, *Simultaneous self-assembly, orientation, and patterning of peptide-amphiphile nanofibers by soft lithography.* Nano Letters, 2007. **7**(5): p. 1165-1171.

130. Schmalenberg, K.E. and K.E. Uhrich, *Micropatterned polymer substrates control alignment of proliferating Schwann cells to direct neuronal regeneration.* Biomaterials, 2005. **26**(12): p. 1423-30.

131. Wang, D.Y., et al., *Microcontact printing of laminin on oxygen plasma activated substrates for the alignment and growth of Schwann cells.* J Biomed Mater Res B Appl Biomater, 2007. **80**(2): p. 447-53.

132. Alvaro Mata, S.S., *Publication in preparation.* 2008.

133. Lee, P., et al., *Microfluidic alignment of collagen fibers for in vitro cell culture.* Biomed Microdevices, 2006. **8**(1): p. 35-41.

134. Mata, A., et al., *Analysis of connective tissue progenitor cell behavior on polydimethylsiloxane smooth and channel micro-textures.* Biomedical Microdevices, 2002. **4**(4): p. 267-275.

135. Charest, J.L., A.J. Garcia, and W.P. King, *Myoblast alignment and differentiation on cell culture substrates with microscale topography and model chemistries.* Biomaterials, 2007. **28**(13): p. 2202-10.

136. Kanda, K. and T. Matsuda, *Mechanical stress-induced orientation and ultrastructural change of smooth muscle cells cultured in three-dimensional collagen lattices.* Cell Transplant, 1994. **3**(6): p. 481-92.

137. Tessierlavigne, M., et al., *Chemotropic Guidance of Developing Axons in the Mammalian Central Nervous-System.* Nature, 1988. **336**(6201): p. 775-778.

138. Luo, Y. and M.S. Shoichet, *A photolabile hydrogel for guided three-dimensional cell growth and migration.* Nature Materials, 2004. **3**(4): p. 249-253.

139. Niece, K.L., et al., *Self-assembly combining two bioactive peptide-amphiphile molecules into nanofibers by electrostatic attraction.* Journal of the American Chemical Society, 2003. **125**(24): p. 7146-7147.

140. Beniash, E., et al., *Self-assembling peptide amphiphile nanofiber matrices for cell entrapment.* Acta Biomaterialia, 2005. **1**(4): p. 387-397.

141. Bohlin K., O.L.C.I., *Isolation and characterization of human smooth muscle cells from umbilical cord vein and their reconstitution in a vascular co-culture model with underlying endothelial cells.* Methods in Cell Science, 1996. **18**(4): p. 329-341(13).

142. Liu, S.Q., et al., *Pattern formation of vascular smooth muscle cells subject to nonuniform fluid shear stress: mediation by gradient of cell density.* American Journal of Physiology-Heart and Circulatory Physiology, 2003. **285**(3): p. H1072-H1080.

143. Silva, G.A., et al., *Selective differentiation of neural progenitor cells by high-epitope density nanofibers.* Science, 2004. **303**(5662): p. 1352-5.

144. Billingsley, M.L. and H.G. Mandel, *Effects of DNA-Synthesis Inhibitors on Post-Traumatic Glial-Cell Proliferation.* Journal of Pharmacology and Experimental Therapeutics, 1982. **222**(3): p. 765-770.

145. Ide, Y. and Z. Ophir, *Orientation Development in Thermotropic Liquid-Crystal Polymers.* Polymer Engineering and Science, 1983. **23**(5): p. 261-265.

146. Yamada, K.M., *Adhesive Recognition Sequences.* Journal of Biological Chemistry, 1991. **266**(20): p. 12809-12812.

147. Veis, A., B. Sabsay, and B.W. Chou, *Phosphoproteins as Mediators of Biomineralization.* Abstracts of Papers of the American Chemical Society, 1989. **197**: p. 92-Iaec.

148. Jack Donners, S.I.S., unpublished data.

149. Shuming Zhang, M.A.G., Alvaro Mata, Ramille M. Capito, Liam C. Palmer, Conrado Aparicio, Jason R. Mantei, Monica Olvera de la Cruz, Samuel I. Stupp, *A Self-Assembly Pathway to Macroscopic Strings of Aligned Nanofibers.* In preparation, 2008.

150. Shuming Zhang, A.J.M., Eugene T. Pashuck, Takahiro Muraoka, Arun Sharma, Samuel I. Stupp, *Using a Preferentially Oriented Peptide Amphiphile Hydrogel Matrix to Control Cellular Orientation and Outgrowth.* In preparation, 2008.

151. *CRC Handbook of Chemistry and Physics, 66th ed., CRC Press, Boca Raton, Florida (1985).*

152. Petersen, O.W., et al., *Interaction with Basement-Membrane Serves to Rapidly Distinguish Growth and Differentiation Pattern of Normal and Malignant Human Breast Epithelial-Cells.* Proceedings of the National Academy of Sciences of the United States of America, 1992. **89**(19): p. 9064-9068.

153. Liu, H. and K. Roy, *Biomimetic three-dimensional cultures significantly increase hematopoietic differentiation efficacy of embryonic stem cells.* Tissue Engineering, 2005. **11**(1-2): p. 319-330.

154. Zhang, S.G., *Fabrication of novel biomaterials through molecular self-assembly.* Nature Biotechnology, 2003. **21**(10): p. 1171-1178.

155. Chockalingam, K., M. Blenner, and S. Banta, *Design and application of stimulus-responsive peptide systems.* Protein Engineering Design & Selection, 2007. **20**(4): p. 155-161.

156. Haines-Butterick, L., et al., *Controlling hydrogelation kinetics by peptide design for three-dimensional encapsulation and injectable delivery of cells.* Proceedings of the National Academy of Sciences of the United States of America, 2007. **104**(19): p. 7791-7796.

157. Kim, H., et al., *Live lymphocyte arrays for biosensing.* Advanced Functional Materials, 2006. **16**(10): p. 1313-1323.

158. Koh, W.G. and M.V. Pishko, *Fabrication of cell-containing hydrogel microstructures inside microfluidic devices that can be used as cell-based biosensors.* Analytical and Bioanalytical Chemistry, 2006. **385**(8): p. 1389-1397.

159. Albrecht, D.R., et al., *Photo- and electropatterning of hydrogel-encapsulated living cell arrays.* Lab on a Chip, 2005. **5**(1): p. 111-118.

160. Pierschbacher, M.D. and E. Ruoslahti, *Variants of the Cell Recognition Site of Fibronectin That Retain Attachment-Promoting Activity.* Proceedings of the National Academy of Sciences of the United States of America-Biological Sciences, 1984. **81**(19): p. 5985-5988.

161. Pierschbacher, M.D. and E. Ruoslahti, *Cell Attachment Activity of Fibronectin Can Be Duplicated by Small Synthetic Fragments of the Molecule.* Nature, 1984. **309**(5963): p. 30-33.

162. Komori, T., et al., *Targeted disruption of Cbfa1 results in a complete lack of bone formation owing to maturational arrest of osteoblasts.* Cell, 1997. **89**(5): p. 755-764.

163. Horowitz, M., *Matrix proteins versus cytokines in the regulation of osteoblast function and bone formation.* Calcified Tissue International, 2003. **72**(1): p. 5-7.

164. Aubin, J.E., et al., *Osteoblast and Chondroblast Differentiation.* Bone, 1995. **17**(2): p. S77-S83.

165. Hartgerink, J.D., E. Beniash, and S.I. Stupp, *Peptide-amphiphile nanofibers: a versatile scaffold for the preparation of self-assembling materials.* Proc Natl Acad Sci U S A, 2002. **99**(8): p. 5133-8.

166. *Purification of RNA from cells and tissues by acid phenol-guanidinium thiocyanate-chloroform extraction.* Nature Methods, 2006. **3**(2): p. 149-150.

167. Matsuda, K., et al., *Gene expression analysis from nuclear poly(A)(+) RNA.* Biotechniques, 2002. **32**(5): p. 1014-+.

168. Aviv, H. and P. Leder, *Purification of Biologically-Active Globin Messenger-Rna by Chromatography on Oligothymidylic-Acid-Cellulose.* Proceedings of the National Academy of Sciences of the United States of America, 1972. **69**(6): p. 1408-&.

169. Jacobsen, N., et al., *Direct isolation of poly(A)(+) RNA from 4 M guanidine thiocyanate-lysed cell extracts using locked nucleic acid-oligo(T) capture.* Nucleic Acids Research, 2004. **32**(7): p. -.

170. Fang, X., et al., *High-throughput sample preparation from whole blood for gene expression analysis.* Journal of the Association for Laboratory Automation, 2006. **11**(6): p. 381-386.

171. Fang, X., et al., *High-throughput sample preparation for gene expression profiling and in vitro target validation.* Journal of the Association for Laboratory Automation, 2004. **9**(3): p. 140-145.

172. Jost, R., O. Berkowitz, and J. Masle, *Magnetic quantitative reverse transcription PCR: a high-throughput method for mRNA extraction and quantitative reverse transcription PCR.* Biotechniques, 2007. **43**(2): p. 206-11.

173. Kamata, S.I. and S. Suzuki, *Concentration of marine birnavirus from seawater with a glass fiber filter precoated with bovine serum albumin.* Marine Biotechnology, 2003. **5**(2): p. 157-162.

174. Mack, E., A. Neubauer, and C. Brendel, *Comparison of RNA yield from small cell populations sorted by flow cytometry applying different isolation procedures.* Cytometry A, 2007. **71**(6): p. 404-9.

175. Sherrill, C.B., et al., *Nucleic acid analysis using an expanded genetic alphabet to quench fluorescence.* Journal of the American Chemical Society, 2004. **126**(14): p. 4550-4556.

176. Johnson, S.C., et al., *A third base pair for the polymerase chain reaction: inserting isoC and isoG.* Nucleic Acids Research, 2004. **32**(6): p. 1937-1941.

177. Rozen, S. and H.J. Skaletsky, *(2000) Primer3 on the WWW for general users and for biologist programmers. In: Krawetz S, Misener S (eds) Bioinformatics Methods and Protocols: Methods in Molecular Biology. Humana Press, Totowa, NJ, pp 365-386*.

178. Bustin, S.A., *A-Z of quantitative PCR.* International University Line, 2004.

179. Wong, M.L. and J.F. Medrano, *Real-time PCR for mRNA quantitation.* Biotechniques, 2005. **39**(1): p. 75-85.

APPENDIX

Appendix 1: Synthesis, Purification and Characterization of Material Used

The peptide amphiphiles with a *C*-terminal carboxylic acid were synthesized on a 0.25-1 mmol scale using a procedure similar to that reported previously [82]. Briefly, the peptide sequence, such as VVVAAAEEE, was synthesized using an automated peptide synthesizer and Fmoc chemistry starting from pre-functionalized Wang resin. Following Fmoc removal from the final residue, hexadecanoic acid (Aldrich) was conjugated to the free *N*-terminus. The alkylation reaction was accomplished by using eight equivalents of the fatty acid, eight equivalents O-Benzotriazole-*N,N,N',N'*-tetramethyl-uronium-hexafluoro-phosphate (HBTU) and 12 equivalents of diisopropylethylamine in 1:1 dimethylformamide and dichloromethane. The reaction was allowed to proceed for at least 6 hours until the ninhydrin test (Kaiser Assay) was negative. Cleavage of peptide amphiphile from the resin and side-chain protection was carried out in 95% trifluoroacetic acid, 2.5% H_2O, 2.5% triisopropylsilane at room temperature for 2 hours. The cleavage mixture and two subsequent dichloromethane washings were filtered into a round-bottom flask. This solution was concentrated by rotary evaporation to a thick viscous solution. The crude PA was isolated by precipitating with cold diethyl ether, filtrating, washing with copious cold ether, and drying under vacuum.

To purify the synthesized peptide amphiphile the resulting material was dissolved in water at a concentration of 10 mg/ml with the addition of NH_4OH to adjust the pH of the solution to 9. The solution was then filtered through a 0.2-μm nylon Acros filter and purified by

preparative-scale high-performance liquid chromatography (HPLC). Collected fractions were analyzed by analytical HPLC and electrospray ionization mass spectrometry (ESI-MS) (Figure 67) and the pure fractions were combined and lyophilized. After lyophilization, the white powder was combined and re-dissolved in PBS at a concentration of 10 mg/ml. The pH of this solution was gradually adjusted to 7.00 by adding 0.5 M NaOH and monitoring with pH meter. Excess salt was then removed by dialyzing this solution against pure water. This step ensured that peptide amphiphile molecules were uniformly ionized to minimize batch-to-batch variation. After dialysis, the solution was re-lyophilized and stored in –20°C freezer before use.

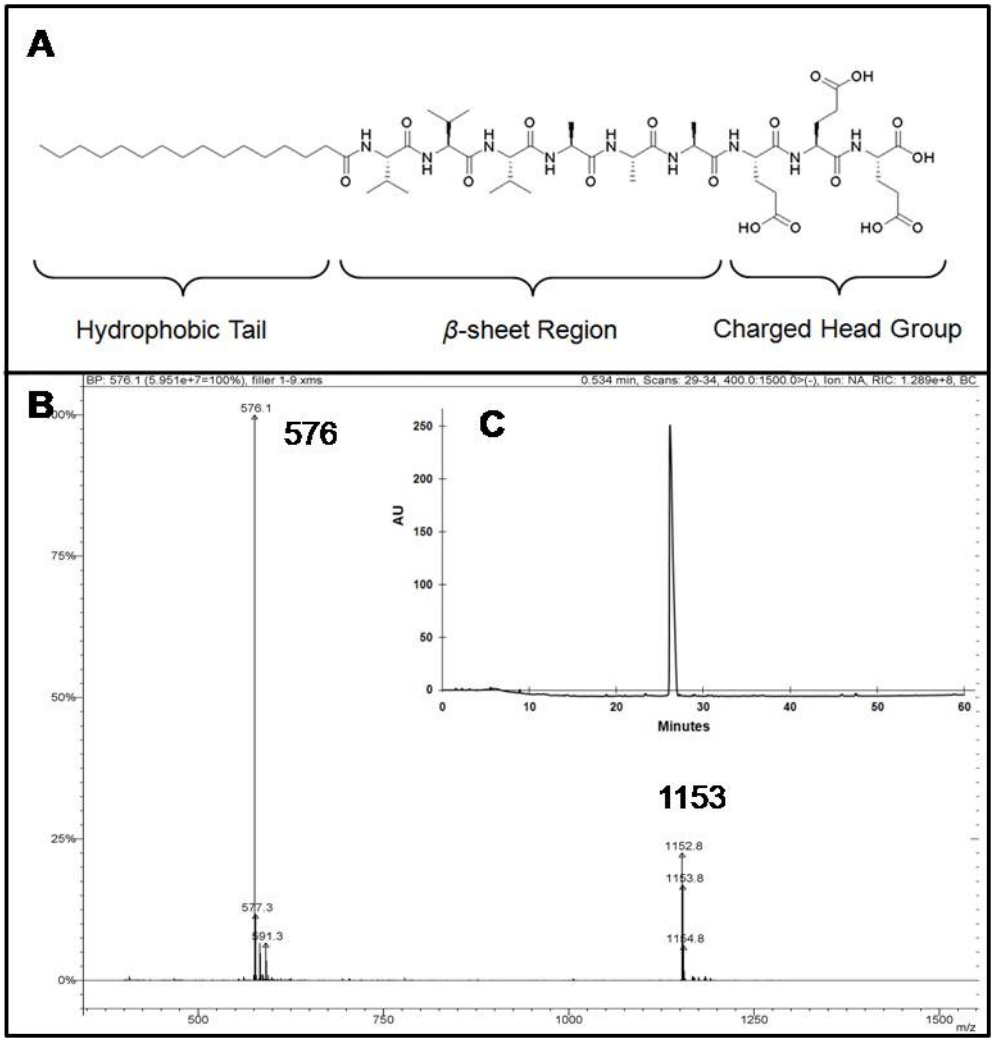

Figure 67 | One example of Peptide amphiphile molecule used in this study and purity test **a,** Chemical structure of the $C_{15}H_{31}CO$-VVVAAAEEE(COOH) PA. This molecule contains three sections: hydrophobic alkyl tail, beta-sheet forming peptide segment, and charged peptide head group. **b**, Single and double charged molecules were detected in ESI-MS. **c**, Analytical HPLC showed single peak. All other PAs used in this thesis work were tested as well.

Appendix 2: How to Design mRNA Primers for Plexor PCR system

Principles to follow:

1. primers have to span introns to avoid DNA contamination
2. there should be minimum interactions among different primers and amplicons
3. blast test should show that there is not any other gene that may show potential applification

Take Alkaline Phosphatase Bone/Liver as an example:

Step 1: Determine Official Symbol and Name for a Specific Gene

There are many naming systems for genes; sometimes the keywords search may give you search results of several genes with similar names. To pick out the right one for your research interest, go to NCBI home page http://www.ncbi.nlm.nih.gov. Choose category “gene”, search for key words, such as "alkaline phosphatase" and "homo". Find the correct Official Symbol: ALPL and Name: alkaline phosphatase, liver/bone/kidney [*Homo sapiens*]

Step 2: Get the Coding Sequence of Target mRNA

Go to ENSEMBL home page http://www.ensembl.org/ and search "*Homo sapiens"* with symbol found in step 1. The search result may return hits from different databases, such as Vaga and Ensembl, here we just choose hit from ENSEMBL. Click on the hyperlink from the search result. You will see a list of gene names such as:

ENST00000344573ENSP00000343937ALPL [Transcript info] [Exon info] [Peptide info]

ENST00000374829ENSP00000363962Q5T3S5_HUMAN [Transcript info] [Exon info] [Peptide info]

ENST00000374830ENSP00000363963Q5T3S5_HUMAN [Transcript info] [Exon info] [Peptide info]

ENST00000374832ENSP00000363965PPBT_HUMAN [Transcript info] [Exon info] [Peptide info]

ENST00000374840ENSP00000363973ALPL [Transcript info] [Exon info] [Peptide info]

Choose the one with key words ALPL and from database ENSEMBL. Click open [Transcript info]. In this page, choose “EXON and CODEON” for “Show the following features:” Refresh, then you will see the full mRNA sequence as below.

TCGGGCCCCGCGGCCGCCTTTATAAGGCGGCGGGGGTGGTGGCCCGGGCCGCGTTGCGCT
CCCGCCACTCCGCGCCCGCTATCCTGGCTCCGTGCTCCCACGCGCTTGTGCCTGGACGGA
CCCTCGCCAGTGCTCTGCGCAGGATTGGAACATCAGTTAACATCTGACCACTGCCAGCCC
ACCCCCTCCCACCCACGTCGATTGCATCTCTGGGCTCCAGGGATAAAGCAGGTCTTGGGG
TGCACCATGATTTCACCATTCTTAGTACTGGCCATTGGCACCTGCCTTACTAACTCCTTA
GTGCCAGAGAAAGAGAAAGACCCCAAGTACTGGCGAGACCAAGCGCAAGAGACACTGAAA
TATGCCCTGGAGCTTCAGAAGCTCAACACCAACGTGGCTAAGAATGTCATCATGTTCCTG
GGAGATGGGATGGGTGTCTCCACAGTGACGGCTGCCCGCATCCTCAAGGGTCAGCTCCAC
CACAACCCTGGGGAGGAGACCAGGCTGGAGATGGACAAGTTCCCCTTCGTGGCCCTCTCC
AAGACGTACAACACCAATGCCCAGGTCCCTGACAGTGCCGGCACCGCCACCGCCTACCTG
TGTGGGGTGAAGGCCAATGAGGGCACCGTGGGGGTAAGCGCAGCCACTGAGCGTTCCCGG
TGCAACACCACCCAGGGGAACGAGGTCACCTCCATCCTGCGCTGGGCCAAGGACGCTGGG
AAATCTGTGGGCATTGTGACCACCACGAGAGTGAACCATGCCACCCCCAGCGCCGCCTAC
GCCCACTCGGCTGACCGGGACTGGTACTCAGACAACGAGATGCCCCCTGAGGCCTTGAGC
CAGGGCTGTAAGGACATCGCCTACCAGCTCATGCATAACATCAGGGACATTGACGTGATC
ATGGGGGGTGGCCGGAAATACATGTACCCCAAGAATAAAACTGATGTGGAGTATGAGAGT
GACGAGAAAGCCAGGGGCACGAGGCTGGACGGCCTGGACCTCGTTGACACCTGGAAGAGC
TTCAAACCGAGATACAAGCACTCCCACTTCATCTGGAACCGCACGGAACTCCTGACCCTT
GACCCCCACAATGTGGACTACCTATTGGGTCTCTTCGAGCCAGGGGACATGCAGTACGAG
CTGAACAGGAACAACGTGACGGACCCGTCACTCTCCGAGATGGTGGTGGTGGCCATCCAG
ATCCTGCGGAAGAACCCCAAAGGCTTCTTCTTGCTGGTGGAAGGAGGCAGAATTGACCAC
GGGCACCATGAAGGAAAAGCCAAGCAGGCCCTGCATGAGGCGGTGGAGATGGACCGGGCC
ATCGGGCAGGCAGGCAGCTTGACCTCCTCGGAAGACACTCTGACCGTGGTCACTGCGGAC
CATTCCCACGTCTTCACATTTGGTGGATACACCCCCCGTGGCAACTCTATCTTTGGTCTG
GCCCCCATGCTGAGTGACACAGACAAGAAGCCCTTCACTGCCATCCTGTATGGCAATGGG
CCTGGCTACAAGGTGGTGGGCGGTGAACGAGAGAATGTCTCCATGGTGGACTATGCTCAC
AACAACTACCAGGCGCAGTCTGCTGTGCCCCTGCGCCACGAGACCCACGGCGGGGAGGAC
GTGGCCGTCTTCTCCAAGGGCCCCATGGCGCACCTGCTGCACGGCGTCCACGAGCAGAAC
TACGTCCCCCACGTGATGGCGTATGCAGCCTGCATCGGGGCCAACCTCGGCCACTGTGCT
CCTGCCAGCTCGGCAGGCAGCCTTGCTGCAGGCCCCCTGCTGCTCGCGCTGGCCCTCTAC
CCCCTGAGCGTCCTGTTCTGAGGGCCCAGGGCCCGGGCACCCACAAGCCCGTGACAGATG

CCAACTTCCCACACGGCAGCCCCCCCCTCAAGGGGCAGGGAGGTGGGGGCCTCCTCAGCC
TCTGCAACTGCAAGAAAGGGGACCCAAGAAACCAAAGTCTGCCGCCCACCTCGCTCCCCT
CTGGAATCTTCCCCAAGGGCCAAACCCACTTCTGGCCTCCAGCCTTTGCTCCCTCCCCGC
TGCCCTTTGGCCAACAGGGTAGATTTCTCTTGGGCAGGCAGAGAGTACAGACTGCAGACA
TTCTCAAAGCCTCTTATTTTTCTAGCGAACGTATTTCTCCAGACCCAGAGGCCCTGAAGC
CTCCGTGGAACATTCTGGATCTGACCCTCCCAGTCTCATCTCCTGACCCTCCCACTCCCA
TCTCCTTACCTCTGGAACCCCCCAGGCCCTACAATGCTCATGTCCCTGTCCCCAGGCCCA
GCCCTCCTTCAGGGGAGTTGAGGTCTTTCTCCTCAGGACAAGGCCTTGCTCACTCACTCA
CTCCAAGACCACCAGGGTCCCAGGAAGCCGGTGCCTGGGTGGCCATCCTACCCAGCGTGG
CCCAGGCCGGGAAGAGCCACCTGGCAGGGCTCACACTCCTGGGCTCTGAACACACACGCC
AGCTCCTCTCTGAAGCGACTCTCCTGTTTGGAACGGCAAAAAAAAATTTTTTTTTCTCTT
TTTGGTGGTGGTTAAAAGGGAACACAAAACATTTAAATAAAACTTTCCAAATATTTCCGA
GG

The yellow part is UTR region. All nucleic acids (DNA and RNA) have a direction in which it is read. The direction in which nucleic acids are read is from the 5' (five-prime) end to the 3' (three-prime) end. So when we discuss the structure of the mRNA, we will also naturally start with the 5’ end, following all the way to the 3’ end tail.

5' UTR MESSAGE UTR 3'

C~~~~~~~AUG~~~~~~~~~~~~~~~~~~(STOP)~~~~~~~~AAAAA//AAAAA

At 5’ side of the mRNA, there is a cap known as the 5' 7-methyl guanosine cap, and serves to identify the RNA as an mRNA (there are several other types of RNA, which do not concern us right now). Just below the cap (and head) is the 5' untranslated region (5' UTR). The UTR is a part of the mRNA which is not made into protein. After the 5' UTR comes the ACTUAL MESSAGE. The message starts off with a standard opening - AUG (adenine-uracil-guanine). It's like saying "Hello!" to start a conversation. From this point on, all this information will be used to make a protein. The message ends with another mRNA code equivalent to "Goodbye!"

(Actually there are 3 codes that can be used, like variations on a theme.) Then another UTR, the 3' untranslated region (3' UTR) follows directly after the message ends. And finally, the mRNA ends with a splendid poly-adenine (poly-A) tail. This is a long (100-250 bases) tail made up entirely of adenine-adenine-adenine-adenine... The longer this tail is, the more stable and longer-lasting is the mRNA.

Step 3: Choose Location for Primers Pairs

Open page [Exon info] and check for the intron and exon information.

Note: all the characters in upper case will be in the final mRNA sequence. The lower case however, will not be part of mRNA.

Choose the right intron or introns you would like to flank Figure 68. By saying right intron, it means the size should be large enough, so during amplification, the DNA would not get enough time to be amplified. Here if it over 1000 bps, it will be good.

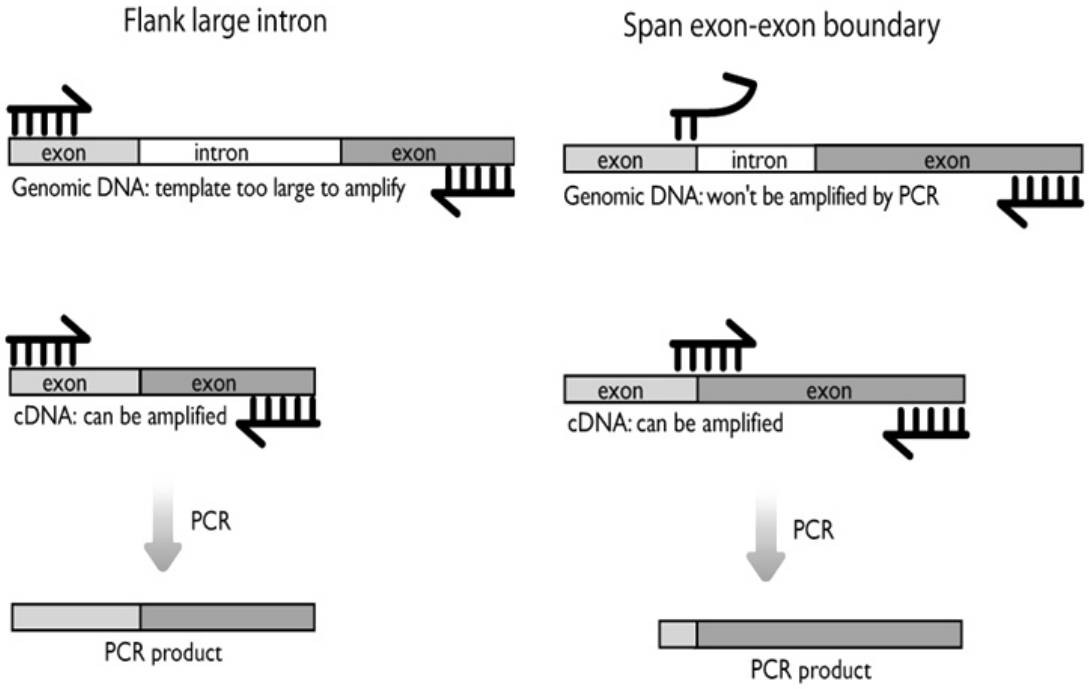

Figure 68 | Designing primers to avoid mistaken amplification of DNA fragment: flank large intron or span exon-exon boundary.

Another criterion is the distance from the 3' end of sequence. A location closer to 3' end, and with a large intron will be a good candidate. For example, in ALPL case, we made the primer flank intron 7-8 and intron 8-9, which are of size 2057 and 3290. DNA contamination would be minimum. The reason that the primer pairs should be closer to 3' is that, plexor system uses Oligo (dT)15 primer and ImProm-II™ Reverse Transcription System for first-strand synthesis reaction in the presence of 1u/µl rRNasin® Ribonuclease Inhibitor and 6mM MgCl2. Since the Oligo(dT)15 will bind to the 3' end and start to make copy from there, a primer pairs closer to that will have a better chance and efficiency in first-strand synthesis reaction Figure 69. For some short gene, this effect is minimum; however, in some cases when the gene is very long, this

should be taken into consideration. Figure 69 illustrates this issue. Oligo(dT) primer only bind to mRNA so this is more specific in first stand systhesis.

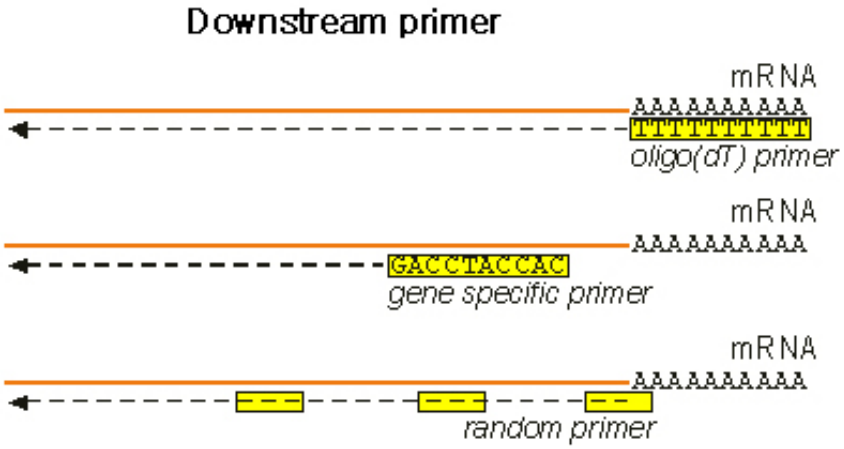

Figure 69 | How RT Primers different from each other

Step 4: Using primer 3 software to design primers at your desired location.

Paste the exons sequence, from which you want the primers to be picked, into the sequence box of primer 3 software interface.

The software location is at http://frodo.wi.mit.edu/cgi-bin/primer3/primer3_www.cgi

In targets box, fill in the base pair position need to be flanked. For example, we can put 142, 20 there. Then the primer designed will include the 20 base pairs after Base Pair position 142. This can help us to make sure that primers are designed to flank intron or introns. Choose product size range as 80-200. Even though for real time PCR, some people like the amplicon size to be around 100, 160 bps is indeed ok as well. Plus, in certain cases, 100 base pair will be too short to flank two introns. Set up other parameters such as primer size, Tm, GC%. Then click Pick primers.

Note: about Tm, the protocol in plexor system recommends 65 °C although not required. The GAPDH control probes have Tm 63 degree C and the manufacturer, Biosearch Technologies, assured that this primer pairs can work ok in a 10 degree window.

Figure 70 is a sample primer design results for ALPL:

```
OLIGO            start  len      tm      gc%   any   3'  seq
LEFT PRIMER         94   20   64.78   60.00  3.00  3.00 ACAACGAGATGCCCCCTGAG
RIGHT PRIMER       259   20   63.92   60.00  3.00  1.00 CCCCTGGCTTTCTCGTCACT
SEQUENCE SIZE: 320
INCLUDED REGION SIZE: 320

PRODUCT SIZE: 166, PAIR ANY COMPL: 6.00, PAIR 3' COMPL: 2.00
TARGETS (start, len)*: 176,2

    1 GGAAATCTGTGGGCATTGTGACCACCACGAGAGTGAACCATGCCACCCCCAGCGCCGCCT


   61 ACGCCCACTCGGCTGACCGGGACTGGTACTCAGACAACGAGATGCCCCCTGAGGCCTTGA
                                      >>>>>>>>>>>>>>>>>>>>

  121 GCCAGGGCTGTAAGGACATCGCCTACCAGCTCATGCATAACATCAGGGACATTGACGTGA
                                                            **

  181 TCATGGGGGGTGGCCGGAAATACATGTACCCCAAGAATAAAACTGATGTGGAGTATGAGA
                                                               <

  241 GTGACGAGAAAGCCAGGGGCACGAGGCTGGACGGCCTGGACCTCGTTGACACCTGGAAGA
      <<<<<<<<<<<<<<<<<<<

  301 GCTTCAAACCGAGATACAAG


KEYS (in order of precedence):
****** target
>>>>>> left primer
<<<<<< right primer
```

Figure 70 | Sample primer design results for ALP.

Step 5: Repeat the Same Procedure for Other Genes involved. Find 2 or 3 primer pairs for each gene.

Step 6: Check blast result. Instead of using the blast data base, we can achieve the same goal by using E-PCR, which also called In-Silico PCR. Program can be accessed with hyperlink

http://genome.ucsc.edu/cgi-bin/hgPcr. If the primer is designed well without any other potential contamination, we should only see one product. And you can calculate its size by the intron and exon information. In setting, we can choose human genome, latest assembly, pastes in the sense and anti sense primer sequence. Set the max product size as 50,000 and submit. Here is an example for Alkaline Phosphatase primer pairs. It gives single hit. So the primer pair is specific. Calculating the size of the amplicons, it exactly equal to the size the primer pairs flanks on the genome.

In-Silico PCR result

Alkaline Phosphatase:

>chr1:21763214+21767266 4053bp

ACAACGAGATGCCCCCTGAG & CCCCTGGCTTTCTCGTCACT

Step 7: Pick the right color for each individual primer pairs.

Dyes available for IQ5 plexor system are listed in Figure 71. To add a dye on the primers, just put an isoC at the 5' end of any of the sense or antisense. When ordering, just add Fam to the 5' end of either of these two sequence. For the principle of Plexor chemistry, please refer to Promega Corp website. The channel currently in use include: Fam, Cal Fluor Red 560 and Cal Fluor Red 610 as labeled in the above pictures. If more channels are needed, we can use Cy5 etc.

Fluorophore	Abs. max (nm)	Em. max (nm)
Cy® 5.5	675	694
Alexa 647	650	668
*Quasar® 670/Cy® 5	647	667
BODIPY® 650/665-X	646	660
Pulsar® 650	460	650
BODIPY® 630/650-X	625	640
CAL Fluor™ Red 635	618	637
BODIPY® TR-X/Alexa 594	590	617
CAL Fluor™ Red 610	590	610
Texas Red X/Alexa 568	578	603
ROX	575	602
Cy® 3.5	581	596
Redmond Red™	580	594
BODIPY® 581/591	581	591
CAL Fluor™ Red 590	569	591
*TAMRA/Rhodamine Red-X	555	580
Alexa 546	556	573
Cy® 3/BODIPY® TMR	544	570
BODIPY® 564/570	563	569
*Quasar® 570	548	566
Alexa 555	555	565
CAL Fluor™ Orange 560	538	559
*HEX	535	556
Alexa 532/VIC/BODIPY® 530/550	532	554
Rhodamine 6G	528	550
Yakima Yellow™	531	549
JOE	520	548
CAL Fluor™ Gold 540	522	544
Alexa 430	433	539
*TET	521	536
Rhodamine Green-X	503	528
Oregon Green® 514	506	526
*6-FAM	494	525
Alexa 488	495	519
*Fluorescein/DANSYL	335	518
BODIPY® FL	502	513
Cy® 2	489	506
BODIPY® 493/503	493	503
Coumarin	432	472
Edans	336	468
Acridine	362	462
Marina Blue	362	459
Pacific Blue	416	451
Alexa 350	346	442

Figure 71 | Available color combinations for Plexor primer system

Appendix 3: Primers List for Human Mesenchymal Stem Cells

Table 4 | Primers List for Human Mesenchymal Stem Cells

Osteogenic Lineage	Marker 1: Alkaline Phosphotase ALPL ACAACGAGATGCCCCCTGAG CCCCTGGCTTTCTCGTCACT Marker 2: Osteopontin OPN GTGATGTCCTCGTCTGTAGCATCA GTAGACACATATGATGGCCGAGG Marker 3: Osteocalcin OCN CTCACACTCCTCGCCCTATT GATCCGGGTAGGGGACTG Marker 4: RUNX2 TCATGGCGGGTAACGATGAA TGGGGAGGATTTGTGAAGACG Marker 3: Collagen I Alpha I COL1A1 GGCCAAGAGGAAGGCCAAGT ACAACACCTTGCCGTTGTCG
Chondrogenic Lineage	Marker 1: Aggrecan AGC1 TGTCCACAAAGTCTTCACCTGTGTAG GTGAGGACCGTCTACGTGCAT Marker 2: Collagen II alpha I COL2A1 TGGTGAAAGAGGACGGACTGG ACCAGCAGGACCGACAGGAC
Myogenic Lineage	Marker 1: Desmin Des AGATGGCCCTGGATGTGGAG CCCTTTGCTCAGGGCTGGT Marker 2: Alpha-Smooth-Muscle-Actin ACTA2 CTGTGCTTCGTCACCCACGTA GATGCTCCCAGGGCTGTTTTC
Non Differentiation	Marker 1: Endoglin CGGAGCTGCTCATGTCCTTG AGAAGGTCAGGCCCGTGATG Or CCCGAGAGGTGCTTCTGGTC GGAAGGTGACCAGGCTGGAA

Vita

Shuming Zhang was born on Oct 15th, 1978 in Fujian Province, People's Republic of China to Keping Zhang and Guihua Chen. He is the younger brother of his sister Dr. Qingrun Zhang. Shuming grew up in Yunan province, southwest China, attending Gao Feng elementary, middle and high School. In the fall of 1996, he enrolled at Tsinghua University in the department of Materials Science and Engineering. In this senior year of undergraduate study, he started to engage in biomaterials research with Prof. Fuzhai Cui. The research topic was on a porous composite bone implant material. July 2000, he graduated with Bachelor degree and started pursuing Master degree in the same school and laboratory. His work has leaded to one US patent, multiple Chinese patents and one referred publication. In the fall of 2002, Shuming enrolled at Northwestern University (Chicago, Illinois) to pursue a Ph. D. in Materials Science and Engineering. He joined Prof. Samuel I. Stupp's research group, applying the techniques of supramolecular chemistry to biomedical applications. His research topic was about creating architectural structures with peptide amphiphiles and find applications in living systems. He also investigated the methods for parallel analysis of cells hydrogel interaction with RT-PCR technique. His research is going to result in one US patent and at least three refereed publications. After graduation, Shuming wants to continue his research interest in biomaterial or bioenergy field.